Nanostructured Materials for Energy Conversion and Energy Storage Applications

John Hong

Kellogg College

A thesis submitted in fulfillment of requirement for the degree of

D.Phil in Engineering Science at the **University of Oxford**

Trinity Term 2018

Abstract

Currently, fossil fuels (i.e. coal, natural gas and oil) make up a significant proportion of our global energy demands and are classified as non-renewable energy sources. It is well known that we are confronting an energy crisis due to the depletion of these fossil fuels. Furthermore, as these fuels become more expensive and harder to source, there is a considerable need for low cost and facile processing of environmentally-friendly energy sources and storage systems.

Nanostructured 0-dimensional to 2-dimensional transition metal oxides and sulphides are promising materials for low-cost and high efficiency energy conversion and storage applications (especially for solar cell and supercapacitor technologies). Their unique physical and chemical properties as well the facile phase synthesis and device fabrication, demonstrate that nanostructured material-based energy sources could allow for the delivery of low cost power generation in the not too distant future. Nevertheless, further research needs to be carried out to increase the overall power conversion efficiencies of these corresponding solar cells and the specific energy storing capacitance of supercapacitors to meet the requirements for integration in commercially-available systems. This thesis is therefore focused on finding various ways to control the size and structures of transition metal oxides and sulphides to 1) understand the energy conversion and storing mechanisms in these materials and 2) to improve the overall energy conversion and storage performance.

For solar cell technologies, this thesis demonstrates a promising synthetic procedure for fabricating colloidal quantum dot (CQD) structures of different sizes based upon a hot injection method and a non-hot injection method. With these synthesis methods, CQDs with a high monodispersity and different band gap properties have been prepared for use in solar cells. Moreover, for quantum dot solar cells (QDSCs), surface functionalization of CQDs is demonstrated through the precise control of a halide ligand exchange method and a hybrid ligand exchange method. It is found that changing the surface molecules on CQDs can significantly alter the electronic and optoelectronic properties, and subsequently increase the power conversion efficiency (PCE) of QDSCs. Finally, two different plasmonic nanoparticles have been employed in QDSCs. The insertion of additional plasmonic nanostructures also improves the PCE performance of QDSCs due to dual plasmonic effects, which allows for more photons to be harnessed by scattering and near-field effects.

For the development of supercapacitors, different solution-based synthetic methods are proposed for the development of novel nanostructures and to understand the underlying electrochemical storage mechanisms. Different aspect ratios of one-dimensional transition metal oxides (nanostructures) can induce the different storing performance of supercapacitors, and hierarchically designed core-shell nanostructures can also result in the better charge storing properties of supercapacitors due to the enlarged surface area, high electrical conductivity and open-porous structures. Moreover, a room temperature (25 °C) and ultrafast synthesis (< 10 min) strategy is demonstrated for producing nanostructured transition metal sulphides through a simple solution-based direct synthetic method. A single crystalline 1-D nanorod electrode is synthesized directly using an ammonium sulphide solution and unique and practically designed energy storing electrodes for supercapacitors are proposed.

The collective works presented in this thesis investigate various growth strategies for synthesizing nanostructured transition metal oxides and sulphides, and also demonstrate novel energy conversion and storage application with these materials. These results provide a significant step forward in the development of energy conversion and storage devices based upon nanostructured materials.

Acknowledgements

First and foremost, I would like to express my gratitude to my supervisors, Prof. SeungNam Cha, Prof. Jung Inn Sohn, Prof. Stephen M. Morris, and Prof. Jong Min Kim (University of Cambridge) for their constant guidance, support, and encouragement in this D. Phil academic journey. It has been an honor and privilege to work with you all. Their insight and wisdom were valuable to my research, various projects, and thesis. I am very grateful to be able to take part in such research and academic work. I also thank them for the exceptional research atmosphere they have fostered in the NST group.

I would like to thank current group members in the NST group, Dr. Bo Hou, Dr. Sanghyo Lee, Dr. Yuljae Cho, Paul Giraud, Sangyeon Pak and Dr. Geon-Hyung An, as well as previous group members, Dr. Gooyeon Hwang, Dr. Jong Bae Park, Dr. Dae-Hwan Jung, Dr. Byung-Sung Kim, Dr. Young-Woo Lee, Dr. A-Rang Jang, Dr. Juwon Lee, Dr. Yong-Hae Kim, Prof. Hansu Kim and Prof. Tae-Lim Choi for providing excellent scientific reasoning, guidance, measurements, enjoyable discussions and invaluable advice about my research. Also, I would like to thank Dr. Jongchul Lim for the photoluminescence measurements, Dr. Jason Brown for SEM, Dr. Colin Johnston, Dr. Sungho Nam and Prof. Hyun-Suk Shin for the TEM and HRTEM measurements presented in this thesis.

I would like to thank my parents, Jin Pyo Hong, Wan Ok Kim, and my younger brother, Jeffrey Hong for their support and unconditional love. Finally, I would like to thank my love, Yae Hyun Kang, for always keeping me grounded. Your support and strength inspire me to always reach higher.

Table of Contents

List of Figures

List of Tables

List of Abbreviation

AFM	Atomic force microscope
Ag	Silver
Au	Gold
BTMO	Binary transition metal oxide
CV	Cyclic voltammetry
C_B	Conduction band
C_T	Charge transfer
CQD	Colloidal quantum dot
DOS	Density of state
EES	Electrochemical energy storage
EDLC	Electrostatic double-layer capacitor
EDT	1,2-Ethaneidthiol
Eg	Band gap
EQE	External quantum efficiency
FF	Fill factor
FT-IR	Fourier-transform infrared
GA	Glycolic acid
GCD	Galvanic charge-discharge
J - V	Current - voltage
ITO	Indium-doped tin oxide
J_{sc}	Short circuit current density
LIB	Lithium ion battery

MPA	3-Mercaptopropinoic acid
NIR	Near infrared region
NREL	National renewable energy laboratory
OA	Oleic acid
ODE	1-Octadecene
PbS	Lead sulphide
PbSe	Lead selenide
PCE	Power conversion efficiency
PL	Photoluminescence
PV	Photovoltaic
QD	Quantum dot
SAED	Selected area diffraction
SC	Supercapacitor
SEM	Scanning electron microscope
TBAI	Tetrabutyl ammonium iodide
TEG	Thiolethylene glycol
TMS	Hexamethyldisilathiane
(HR)TEM	(High resolution) Transmission electron microscope
V_B	Valence band
Voc	Open circuit voltage
XRD	X-ray powder diffraction
XPS	X-ray photoelectron spectroscopy
ZnO	Zinc oxid

Chapter 1. Introduction

1.1 Motivation for the Thesis

The development of new methods for efficient energy generation and storage is of paramount importance in order to meet the ever-increasing global energy demands. At present, fossil fuels generate more than 70.0 % of primary energy supply in the earth, but it is well-documented that these fuels are rapidly running out.[1-2] Moreover, the global population has also seen a steep increase to 7.6 billion people as of 2018, which is expected to grow further by 2100.[3] At the same time, the consumption of the remaining forms of fossil fuel will dramatically increase year on year, shortening the time remaining until the total depletion of these fossil fuels (**Figure 1.1**).[4-6]

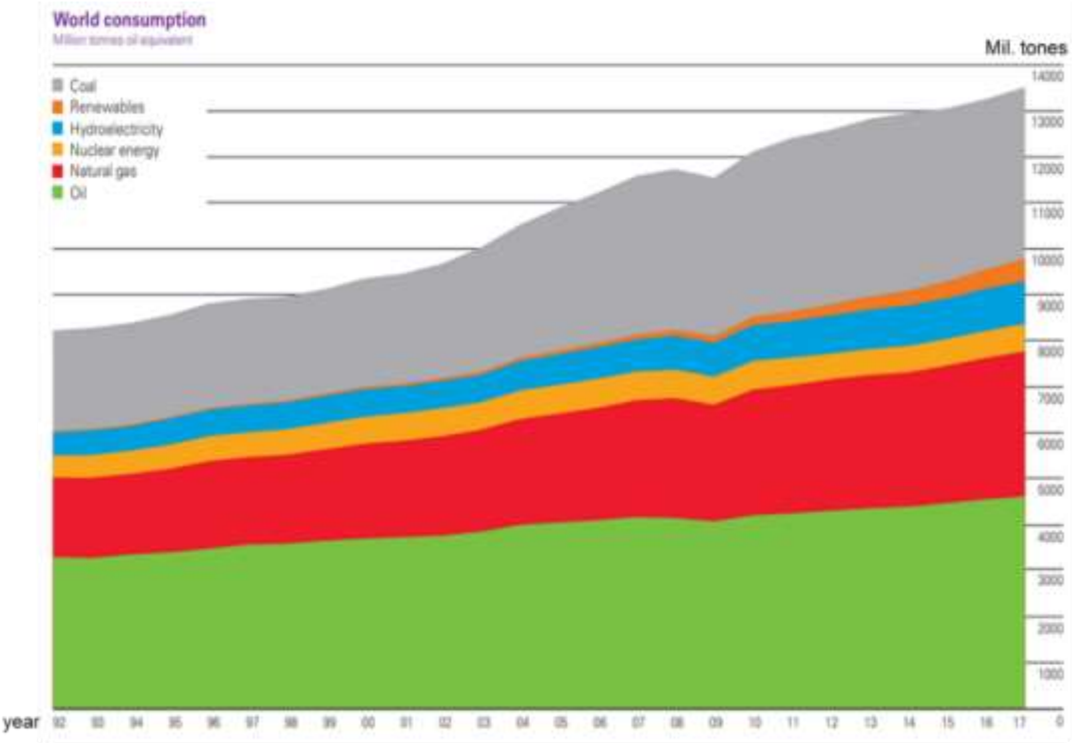

Figure 1.1: Summary of world-wide energy consumption (reproduced from Ref. 1).

Moreover, carbon dioxide (CO_2) and greenhouse gas emissions from the combustion of those fossil fuels constitute the major sources of global warming as they induce changes in the climate, resulting in severe damage to environment, and negative effects on social systems.[7-9] In addition, environmentally-hazardous pollutants from fossil fuels, such as sulphur oxides (SO_x) and nitric oxide (NO_x) have increased significantly due to the consumption of those fossil fuels.[10-11] For these reasons, a large number of research teams are currently attempting to discover new ways to replace those fossil fuels. One approach is the introduction of new forms of energy generation using renewable sources such as wind, ocean and solar energy.[12-14] Of all the energy sources, the sun can provide substantially larger amounts of energy than other renewable energy resources on a daily basis. In addition to the efficient extraction of energy from renewable sources, another issue concerns the non-constant and variable generation of electricity from renewable sources.[15] Therefore, another avenue that has to be explored is to find the new types of systems that can store energy to ensure that the delivery of energy to the consumer remains constant. In this respect, nanostructured materials have emerged as a leading candidate to achieve these two goals both in terms of energy conversion and storage. This is because of their unique energy harvesting and storing mechanisms.

Nanostructured materials constructed from 0-dimensional to 2-dimensional materials have already demonstrated their exceptional optical and photovoltaic properties because the small dimensions of the materials, close to atomic sizes.[16] Moreover, the large surface area of these nanostructured materials has significant implications with respect to electrochemical energy storage devices as they provide the large storing active sites and favorable ion diffusion kinetics for supercapacitors.[17] Therefore, to optimize the energy harvesting and storing performance of those nanostructured materials, various strategies such as decreasing the particle size, controlling the morphology, combining different nanomaterial structures, and functionalizing the surface of nanomaterials have been proposed so as to tailor their energy-related properties.

1.2 Quantum Dot Solar Cell

Solar energy is one of the most abundant and sustainable candidates for future energy harvesting. A direct way to convert solar energy to electrical energy is through the use of photovoltaic cells (PVs).[18] Currently, commercially-available solar cells (SCs) and solar panels have been developed using a variety of bulk semiconductor materials. At present, the dominant photovoltaic material on market is crystalline Silicon (Si), followed by thin film semiconductor materials such as cadmium telluride (CdTe) and copper indium gallium selenide (CIGS).[19-21] However, there are a lot of challenges involved in the use of these materials in PVs such as the high manufacturing cost of thin film semiconductor materials. In addition, CdTe and CIGS contain Tellurium (Te) and Indium (In), which are both in short supply in the earth. Therefore, these materials are very expensive and require complex high-temperature extraction processes. In this regard, reducing the costs of harnessing solar energy is being solicited through cheap and low temperature solution-processed semiconductors such as 0-dimensinal colloidal quantum dots (CQDs).[22]

The major benefits of CQDs are tunable band gap, the relatively inexpensive material and the production costs afforded by the colloidal synthesis process.[23-25] As a result of the tunable band gap, CQD solar cells are able to harvest light from across the entire solar spectrum, including the near infrared (NIR) region which is typically beyond the absorption bands of bulk materials.[26] Moreover, solution synthesis techniques also allow CQD-based PVs to be manufactured using a simple solution phase deposition such as spin coating, casting or inkjet printing as well as practical roll-to-roll production. Amongst the many CQD candidates, lead-based chalcogenide quantum dots such as lead sulphide (PbS) and lead selenide (PbSe) have shown to be, potentially, the most attractive CQDs for PVs, possessing an ε_{gap} of ~1.3 eV thus resulting in absorption at NIR wavelengths.[27] Recently, the highest power conversion efficiencies (PCEs) of quantum dot-based solar cells (QDSCs) that have been reported have exceeded 10%, and research on these technologies has continued to demonstrate considerable efficiency improvements in recent years (**Figure 1.2**).[28-29] However, compared to bulk semiconductor materials, the PCE of QDSCs are slightly lower than that of commercialized thin film solar cells. To develop high-efficiency CQD photovoltaics, we need to find new colloidal synthesis methods and to consider in more depth the process of surface functionalization and the role of device architecture in order to maximize the charge extraction properties of CQD films.

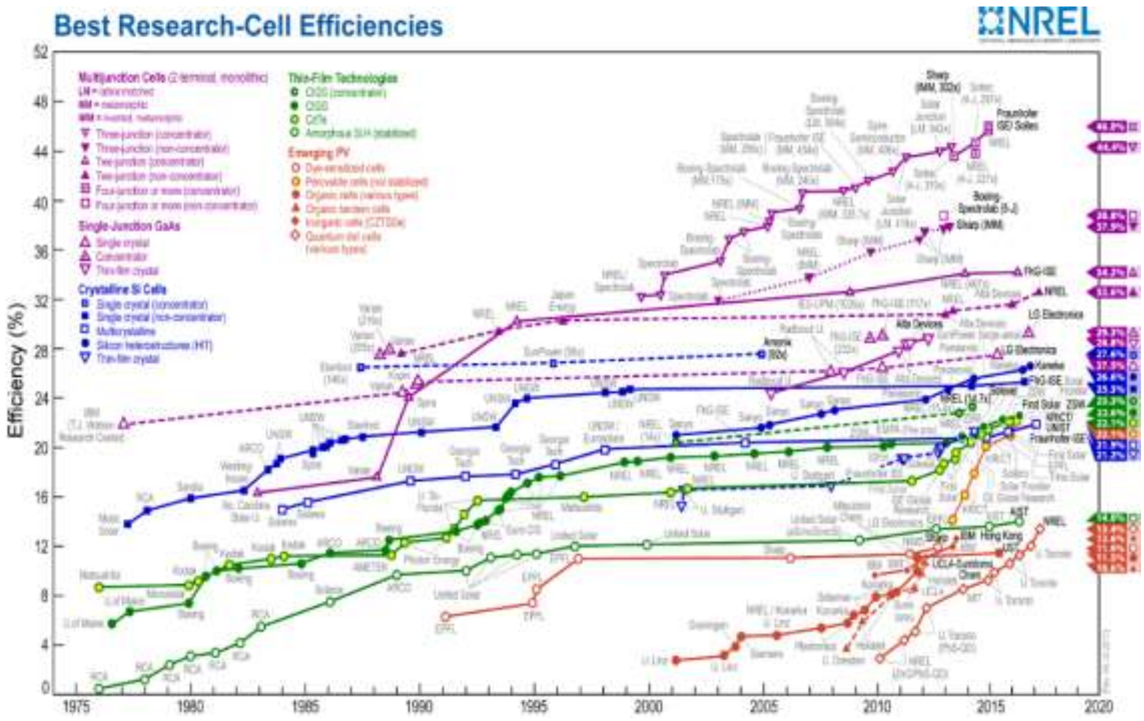

Figure 1.2: Best Research-Cell efficiencies that were presented by NREL (reproduced from Ref. 28).

1.3 Nanostructured Energy Storage Applications

Electrical energy generated from renewable resources such as solar radiation is a great alternative to fossil fuels and have the potential to meet future energy demands in a sustainable manner. However, the energy extracted from renewable sources often results in the intermittent generation of electricity and therefore additional energy storing components are required. Recently there has been a growing interest in high power and high energy density storage systems through electrochemical energy storage (EES) systems such as Li ion batteries, capacitors and supercapacitors.[30-31] Specifically, electrochemical supercapacitors are currently being considered as a promising candidate for next-generation energy storage applications since they have the potential to bridge the gap between batteries and conventional capacitors to produce higher power densities. Furthermore, they have been shown to exhibit a good rate capability, long cycling life time, and environmentally friendly characteristics (**Figure 1.3**).[32] However, they cannot be used as standalone units in these applications since their energy storing performance is lower to that of Li-batteries. At present, the scientific community is striving to dramatically enhance the energy density of supercapacitors by developing new electrode materials and electrolytes, and to explore unique device designs.[33-35]

To date, it has been widely proposed and generally accepted that the structural engineering of electrode materials (transition metal oxides and sulphides) on the nanoscale, through the miniaturization of size as well as the construction of porous-structures, is an effective and viable strategy towards steadily improving the performance of supercapacitors.[36-38] In particular, nanostructures in electrode materials enlarge the electrochemically active surface sites for large energy-storing sites as well as providing favorable electrode surface conditions for fast ionic and electronic transport over small diffusion length scales. Therefore, engineering the electrode designs using nanostructures offers a promising avenue to obtain high-performance supercapacitors.

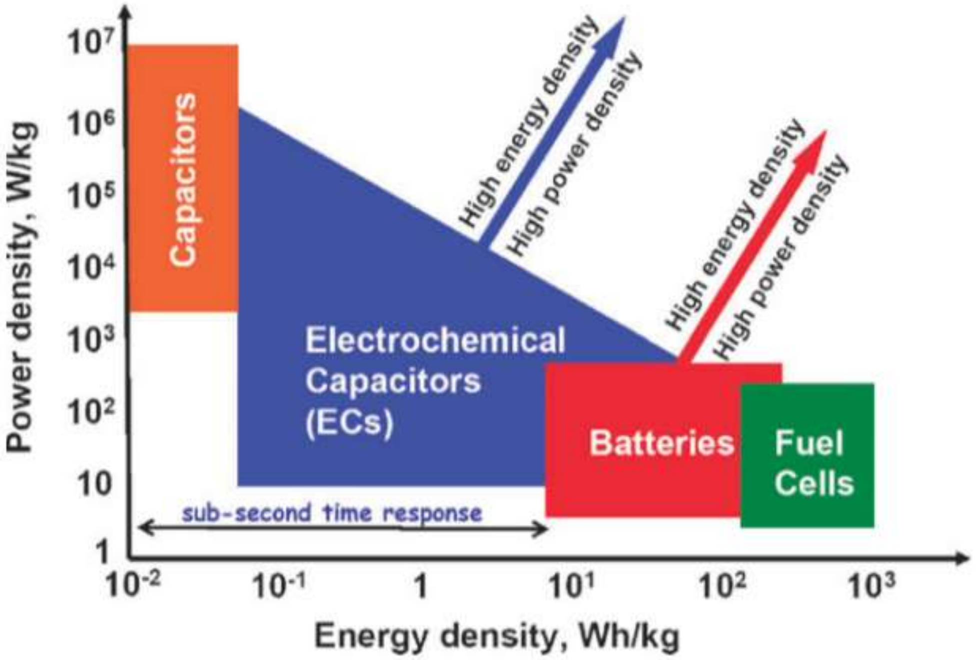

Figure 1.3: Comparison of the operational characteristics of EESs (reproduced from Ref. 39).

1.4 Structure of the Thesis

Chapter One provides a motivation for the thesis, and a broad overview of energy conversion and storage devices using nanostructured materials. The chapter begins with an introduction to the concept of low dimensional materials in solar cells and electrochemical supercapacitors.

Chapter Two introduces the main concepts of solar energy harvesting using 0-dimensinoal colloidal quantum dots and electrochemical supercapacitors (a literature survey is carried out on CQDS, QD photovoltaics, nanostructure synthesis and ESS energy storage systems). The chapter begins with a general description of 0-dimensional nanostructured materials (quantum dots) and their corresponding photovoltaic properties.

The electrical characteristics of solar cells and the standard figures of merit of solar cells that are used to describe device performance are then discussed. Moreover, a basic description of an electrochemical energy storage system, underlying storage mechanism, and electrochemical characteristics for such a storage system is then described. Towards the end of the chapter, the general ideas for nanostructured material electrodes for supercapacitors are discussed.

Chapter Three describes the experimental and synthetic techniques of PbS CQD and their subsequent characterization. Controlling the synthetic parameters to provide well-organized PbS CQDs and to tune the band gap of PbS CQDs is important to increase solar cell performance. It is demonstrated that the mole ratio between the precursors and a new anion sulphur source can lead to the creation of PbS CQDs with better crystallinity and band gap tunablity. The work presented in this chapter has been published in **ACS Energy Lett.** 1, 834 (2016) and **J. Mater. Chem. C** 5, 3692 (2017).

Chapter Four reports the surface functionalization of CQDs as a means for improving the charge extraction properties using short-chain chemical structures. It is systematically shown that the energy conversion performance is affected by the short ligand layers (halide and pyridine) that cap the CQDs. The work presented in this chapter has been published in **Appl. Phys. Lett.** 109, 063901 (2016) and **J. Mater. Chem. A** 4, 18769 (2016).

Chapter Five explores the structural control of QDSCs through the insertion of various supporting nanostructures to extract more charge carriers from the CQD films. Here, metal (gold and silver) nanoparticles are employed to absorb more incident photon energy. This work has been submitted for publication in **ACS Appl. Mater. Interfaces**

(2018).

Chapter Six discusses new nanostructured electrode materials (transition metal oxides and sulphides) that have been designed to improve the overall energy storing performance. A variety of facile synthetic methods are presented for the nanostructured electrodes, and their unique energy storing performance are discussed. It is demonstrated that the nanostructured electrodes offer a promising avenue to fulfil high-performance energy storage system. The work presented in this chapter has been published in **ACS. Appl. Mater. Interfaces** 8, 35227 (2016) and **Nano Energy** 39, 337 (2017), and submitted for publication in **Adv. Sci.** (2018).

Finally, **Chapter Seven** concludes the scientific findings of the thesis and proposes further work that could be carried out.

1.5 References

[1] British Petroleum (BP), “BP statistical review of world energy 2018,” (https://www.bp.com/content/dam/bp/en/corporate/pdf/energy-economics/statistical-review/bp-stats-review-2018-full-report.pdf), 2018.

[2] J. Jewell, D. McCollum, J. Emmerling, C. Bertram, D. Gernaat, V. Krey, L. Paroussos, L. Berger, K. Fragkiadakis, I. Keppo, N. Saadi, M. Tavoni, D. van Vuuren, V. Vinichenko, and K. Riahi, “Limited emission reductions from fuel subsidy removal except in energy-exporting regions,” Nature, vol. 554, no. 7691, p. 229, 2018.

[3] United Nations (UN), “World population prospects 2017,” (https://esa.un.org/unpd/wpp/DataQuery), 2017.

[4] S. Chu and A. Majumdar, “Opportunities and challenges for a sustainable energy future,” Nature, vol. 488, no. 7411, p. 294, 2012.

[5] J. Chow, R. J. Kopp, and P. R. Portney, “Energy resources and global development,” Science, vol. 302, no. 5650, p. 1528, 2003.

[6] International Energy Agency. “World energy outlook 2017,” (http://www.iea.org/weo2017), 2017.

[7] S. Chu, Y. Cui, and N. Liu, “The path towards sustainable energy,” Nat. Mater., vol. 16, no. 1, p. 16, 2016.

[8] S. A. Montzka, E. J. Dlugokencky, and J. H. Butler, “Non-CO_2 greenhouse gases and climate change,” Nature, vol. 476, no. 7358, p. 43, 2011.

[9] T. Root, J. Price, K. Hall, S. Schneider, C. Rosenzweig, and A. Pounds, "Fingerprints of global warming on wild animals and plants," Nature, vol. 421, no. 6918, p. 57, 2003.

[10] A. Desai, "A review on assessment of air pollution due to vehicular emission in traffic area," Int. J. Curr. Eng. Technology, vol. 8, no. 2, 2018.

[11] J. Lelieveld, J. S. Evans, M. Fnais, D. Giannadaki, and A. Pozzer, "The contribution of outdoor air pollution sources to premature mortality on a global scale," Nature, vol. 525, no. 7569, p. 367, 2015.

[12] R. H. Crawford, "Life cycle energy and greenhouse emissions analysis of wind turbines and the effect of size on energy yield," Renew. Sustain. Energy Rev., vol. 13, no. 9, p. 2653, 2009.

[13] A. Westwood, "Ocean power: wave and tidal energy review," Refocus, vol. 5, no. 5, p. 50, 2004.

[14] Editorial, "Solar energy's path towards competitiveness," Nat. Mater., vol. 11, no. 3, p. 173, 2012.

[15] J. P. Barton, and D. G. Infield, "Energy storage and its use with intermittent renewable energy," IEEE T. Energy Conver., vol. 19, no. 2, p. 441, 2004.

[16] R. Yu, Q. Lin, S.-F. Leung, and Z. Fan, "Nanomaterials and nanostructures for efficient light absorption and photovoltaics," Nano Energy, vol. 1, no. 1, p. 57, 2012.

[17] A. Aricò, P. Bruce, B. Scrosati, J.-M. Tarascon, and W. van Schalkwijk, "Nanostructured materials for advanced energy conversion and storage devices," Nat. Mater., vol. 4, no. 5, p. 366, 2005.

[18] M. Gul, Y. Kotak, and T. Muneer, “Review on recent trend of solar photovoltaic technology,” Energ. Explor. Exploit., vol. 34, no. 4, p. 485, 2016.

[19] C. Battaglia, A. Cuevas, and S. Wolf, “High-efficiency crystalline silicon solar cells: status and perspectives,” Energy Environ. Sci., vol. 9, no. 5, p. 1552, 2016.

[20] B. Basol, and B. McCandless, “Brief review of cadmium telluride-based photovoltaic technologies,” J. Photonics Energy, vol. 4, no. 1, p. 040996, 2014.

[21] J. Ramanujam and U. Singh, “Copper indium gallium selenide based solar cells – a review,” Energy Environ. Sci., vol. 10, no. 6, p. 1306, 2017.

[22] O. Semonin, J. Luther, and M. Beard, “Quantum dots for next-generation photovoltaics,” Mater. Today, vol. 15, no. 11, p. 508, 2012.

[23]. P. de Arquer, T. Lasanta, M. Bernechea, and G. Konstantatos, “Tailoring the electronic properties of colloidal quantum dots in metal–semiconductor nanocomposites for high performance photodetectors,” Small, vol. 11, no. 22, p. 2636, 2015.

[24] J. Tang, L. Brzozowski, A. Barkhouse, X. Wang, R. Debnath, R. Wolowiec, E. Palmiano, L. Levina, A. Pattantyus-Abraham, D. Jamakosmanovic, and E. Sargent, “Quantum dot photovoltaics in the extreme quantum confinement regime: the surface-chemical origins of exceptional air- and light-stability,” ACS Nano, vol. 4, no. 2, p. 869, 2010.

[25] X. Lan, O. Voznyy, A. Kiani, P. de Arquer, A. Abbas, G. Kim, M. Liu, Z. Yang, G. Walters, J. Xu, M. Yuan, Z. Ning, F. Fan, P. Kanjanaboos, I. Kramer, D. Zhitomirsky, P. Lee, A. Perelgut, S. Hoogland, and E. Sargent, “Passivation using molecular

halides increases quantum dot solar cell performance," Adv. Mater., vol. 28, no. 2, p. 299, 2016.

[26] J. Tang, K. Kemp, S. Hoogland, K. Jeong, H. Liu, L. Levina, M. Furukawa, X. Wang, R. Debnath, D. Cha, K. Chou, A. Fischer, A. Amassian, J. Asbury, and E. Sargent, "Colloidal-quantum-dot photovoltaics using atomic-ligand passivation," Nat. Mater., vol. 10, no. 10, p. 765, 2011.

[27] Y. Cho, P. Giraud, B. Hou, Y. Lee, J. Hong, S. Lee, S. Pak, J. Lee, J. Jang, S. Morris, J. Sohn, S. Cha, and J. Kim, "Charge transport modulation of a flexible quantum dot solar cell using a piezoelectric effect," Adv. Energy Mater., vol. 8, no. 3, p. 1700809, 2017.

[28] NREL, "https://www.nrel.gov/pv/assets/images/efficiency-chart-20180716.jpg," 2018.

[29] Z. Yang, J. Fan, A. Proppe, P. de Arquer, D. Rossouw, O. Voznyy, X. Lan, M. Liu, G. Walters, R. Quintero-Bermudez, B. Sun, S. Hoogland, G. Botton, S. Kelley, and E. Sargent, "Mixed-quantum-dot solar cells," Nat. Comm., vol. 8, no. 1, p. 1325, 2017.

[30] C. Liu, F. Li, L. Ma, and H. Cheng, "Advanced materials for energy storage," Adv. Mater., vol. 22, no. 8, p. E28, 2010.

[31] Y. Gogotsi, "Materials science: energy storage wrapped up," Nature, vol. 509, no. 7502, p. 568, 2014.

[32] P. Simon, Y. Gogotsi, and B. Dunn, "Where do batteries end, and supercapacitors begin?" Science, vol. 343, no. 6176, p. 1210, 2014.

[33] J. Yan, Q. Wang, T. Wei, and Z. Fan, "Recent advances in design and fabrication of electrochemical supercapacitors with high energy densities," Adv. Energy Mater., vol. 4, no. 4, p. 1300816, 2014.

[34] S. Guo and S. Dong, "Graphene nanosheet : synthesis, molecular engineering, thin film, hybrids, and energy and analytical applications," Chem. Soc. Rev., vol. 40, no. 5, p. 2644, 2011.

[35] G. Lee, D. Kim, D. Kim, S. Oh, J. Yun, J. Kim, S.-S. Lee, and J. Ha, "Fabrication of a stretchable and patchable array of high performance micro-supercapacitors using a non-aqueous solvent based gel electrolyte," Energy Environ. Sci., vol. 8, no. 6, p. 1764, 2015.

[36] X. Rui, H. Tan, and Q. Yan, "Nanostructured metal sulfides for energy storage," Nanoscale, vol. 6, no. 17, p. 9889, 2014.

[37] S. Peng, L. Li, H. Wu, S. Madhavi, and X. Lou, "Controlled growth of $NiMoO_4$ nanosheet and nanorod arrays on various conductive substrates as advanced electrodes for asymmetric supercapacitors," Adv. Energy Mater., vol. 5, no. 2, p. 1401172, 2015.

[38] A. Pendashteh, S. Moosavifard, M. Rahmanifar, Y. Wang, M. El-Kady, R. Kaner, and M. Mousavi, "Highly ordered mesoporous $CuCo_2O_4$ nanowires, a promising solution for high-performance supercapacitors," Chem. Mater., vol. 27, no. 11, p. 3919, 2015.

[39] D. Rolison, J. Long, J. Lytle, A. Fischer, C. Rhodes, T. McEvoy, M. Bourg, and A. Lubers, "Multifunctional 3D nanoarchitectures for energy storage and conversion," Chem. Soc. Rev., vol. 38, no. 1, p. 226, 2008.

Chapter 2. Background and Literature Review

This chapter introduces the background information and literature review important to the studies presented in this thesis. From a top level, my thesis explores two areas: energy conversion and energy storage applications with nanostructured materials. For energy conversion, we provide the relevant background on 0-dimensional colloidal nanostructures (quantum dots) including how they are prepared, characterized and employed in energy conversion technologies. Following this, we then introduce and discuss work that has been done on 1 or 2-dimensional nanostructured metal oxides and sulphides for electrochemical energy storage applications. In general, the chapter provides a broad description of solar cell technologies and energy storage applications.

2.1 Quantum Dots and Photovoltaic Solar Cells

2.1.1. 0-Dimensonal semiconductors and quantum dots

In bulk semiconductors, materials are of a sufficient size such that they are not constrained by their exciton Bohr Radius (a mean radius of the orbit of an electron) and thus do not exhibit any quantum confinement effects. In this case, electrons and holes are free to move and, as a result, they are highly delocalized. Therefore, the energy bands cover a continuous range of values and, upon excitation, the confinement of excitons of the materials is negligible, leading to a so-called continuous density of states (DOS).[1] However, when the dimensions of the materials become sufficiently small, the DOS of the materials become discrete, and they lose their continuous band features. Moreover, the confinement of excitons to discrete DOS leads to unique electronic and photovoltaic properties because the size is comparable or smaller than their Bohr radius.[2-3]

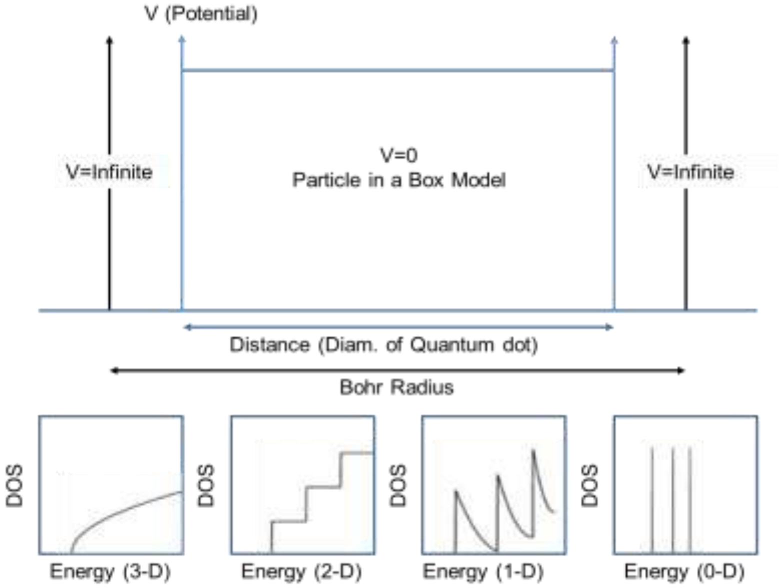

Figure 2.1: Schematic of the particle-in-a-box model and the corresponding DOS for various dimensionalities (reproduced from Ref. 1).

As illustrated in **Figure 2.1**, the DOS of bulk semiconductors covers a continuous range of values, but when the charge carriers and the excitons are confined in all dimensions (0-D), the energy bands converge to atomic-like discrete energy states. An example of such a system are colloidal quantum dots (zero-dimensional materials), which can induce strong confinement effects. The energy gap of colloidal quantum dots (CQDs) can be estimated using a model for the particle-in-a-box based upon the following equation:[4-5]

$$E_g(L) \approx E_g(Bulk) + \frac{h^2}{2L^2}\left(\frac{1}{m_e} + \frac{1}{m_h}\right) - \frac{1.8e^2}{2\pi\varepsilon_0\varepsilon L} \qquad [2.1]$$

where L is the size (radius) of the box or material, E_g is the band-gap energy, h is Planck's constant, m is the effective mass, e is the elementary charge, and $\varepsilon_0\varepsilon$ is the dielectric constant. In the equation, size dependent energy terms are included: first, the confinement energies for hole and electrons, which have size dependency of $1/L^2$. Second, the Coulomb interaction between the electrons and the holes depend on size in the form $1/L$. Therefore, for very small CQDs, the confinement energy forms the predominant part of Equation 2.1, hence to induce strong quantum confinement (i.e. a large band-gap), the overall size of the CQDs should be decreased, which can be seen from the $1/L^2$ dependence. Therefore, reducing the radius of the CQD results in an increased energy gap. This effect is known as the "Quantum size effect" and can be used to control the energy gap of CQDs, tailoring the optical properties of CQDs over a wide spectral range (**Figure 2.2**).[6]

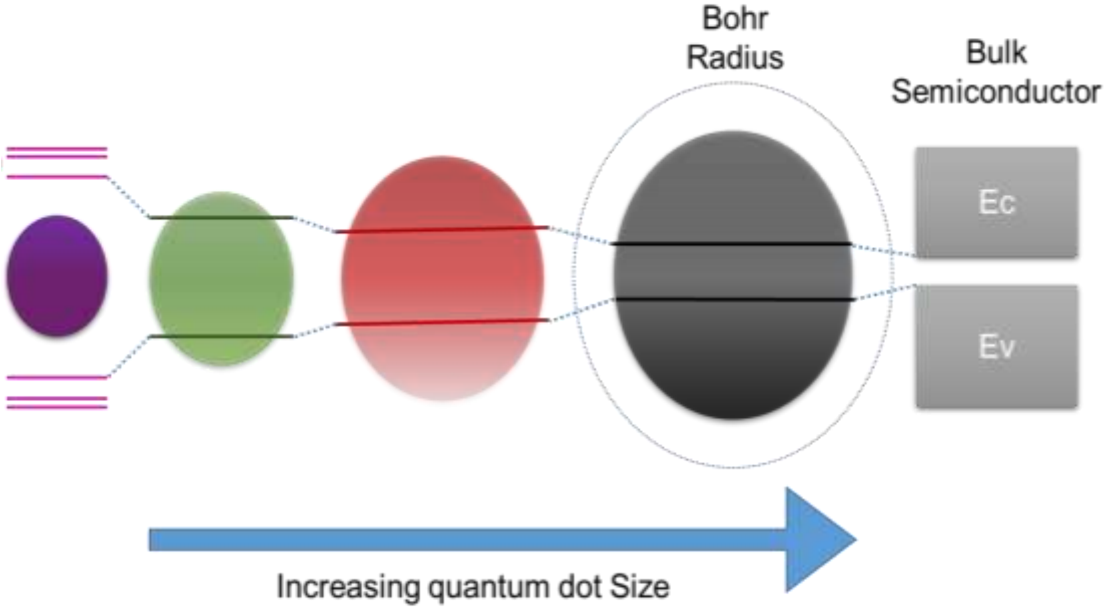

Figure 2.2: A schematic illustrating the correlation between the quantum dot size and the corresponding band gap (E_c = conduction band and E_v = valence band).

2.1.2. Quantum dot synthesis and structure

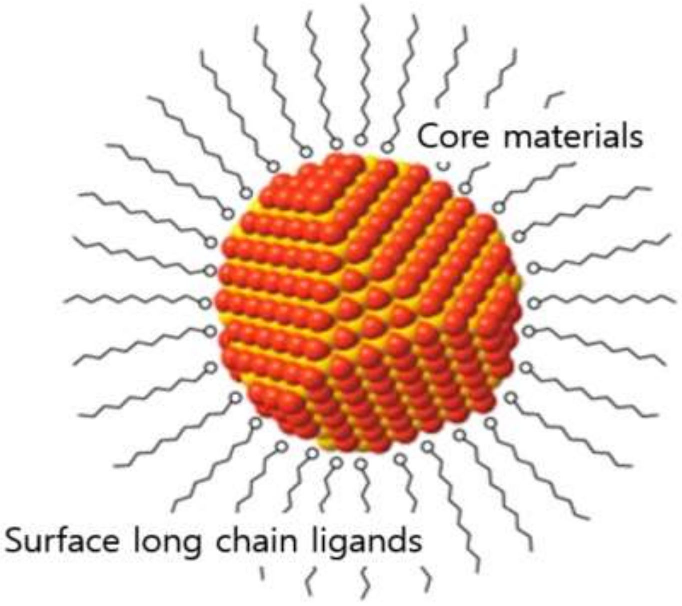

Figure 2.3: A Schematic of a colloidal quantum dot (reproduced from Ref. 7).

Colloidal quantum dots are single-crystal clusters of ~100 to ~10,000 atoms that are 2 to 10 nm in size (**Figure 2.3**).[8-9] There are many methods used in the fabrication or synthesis of CQDs, which can be classified as being either top-down (i.e. cleaving a piece of the material) or bottom-up (assembling atoms).[10-11] Of all the techniques, colloidal (Wet Chemistry) synthesis is one of the most widespread and efficient bottom-up methods employed to synthesize CQDs (**Figure 2.4**). The method is inexpensive and can be used to rapidly synthesize large quantities of CQDs as well as providing wide band gap tunability. Specifically, molecular metal precursors are first heated in a reactor followed by the fast injection of other anion precursors, which result in rapid nucleation. The growth conditions of CQDs strongly depend on the reaction temperature and time. Moreover, another important composition in the nucleation and growth of CQDs is the presence of organic surfactant molecules or long-chain bulky ligands, which adhere dynamically to the crystals that grow during the synthesis process. The role of ligands is to allow the addition of reactants to the crystals when the reaction temperature is high, and to block the accumulation of crystals when the reaction temperature is low. Therefore, the ligands attached on the surface of CQD crystals as well as the reaction temperature and time are all important parameters that determine the size of the resulting CQDs.[12]

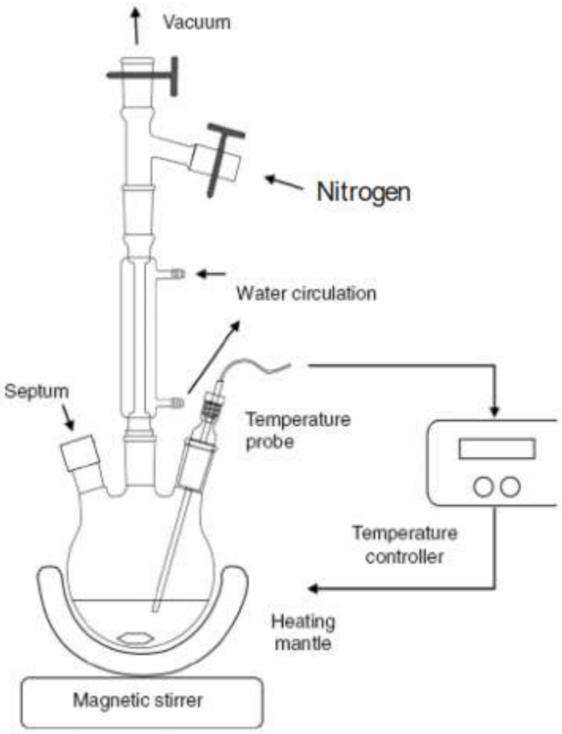

Figure 2.4: A Schematic of a typical experimental setup for colloidal synthesis of CQDs (reproduced from Ref. 13).

To use CQDs as an active photovoltaic layer, researchers have adopted various growth strategies to fabricate QDs with a range of band-gap energies so as to harvest photons from across the entire solar spectrum. However, long and bulky chain ligands typically impede charge transport and the surface coverage of the CQDs is not entirely complete, resulting in non-passivated dangling bonds. These dangling bonds act as midgap surface states, degrading the CQDs electrical properties. Recently, research groups have focused on controlling the ligands for the purposes of practical photovoltaic applications. For example, the solid-state and solution phase treatments of CQDs using alternative ligands and linkers have been reported.[14-16] Chapters 3 and 4 will deal with newly designed synthetic approaches to control the physical properties of CQDs and the efforts of controlling solid-state ligand exchange methods to improve the solar cell performance.

2.1.3. Photovoltaic solar cell

When photons are absorbed by semiconductor materials, they can create electron-hole (exciton) pairs or free charged carriers. These pairs or carriers usually recombine rapidly with each other and relax to their ground state. Before the relaxation, the built-in electric field in a photovoltaic device transports and diffuse the carriers to an external electrical circuit so as to generate electricity.[17-19] By forming a p-n junction using n-type and p-type semiconducting materials, a space charge region is formed where an internal built-in potential is induced. When p-type and n-type materials are brought together they create a p-n junction and the diffusion of holes from the p-type layer into the n-type layer and electrons from the n-type layer into the p-type layer results in the creation of a region that is depleted of charge (**Figure 2.5**).

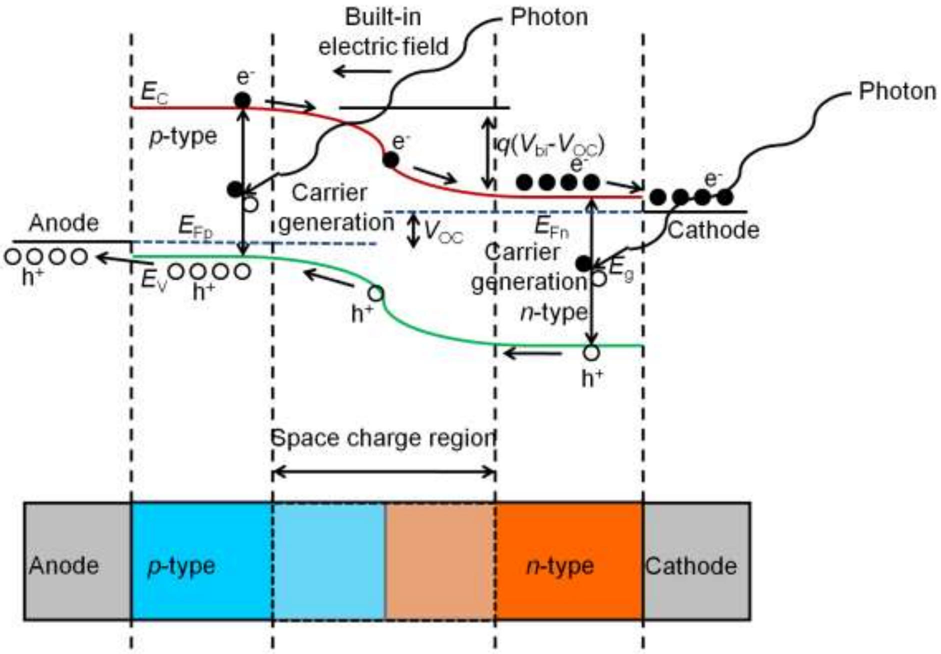

Figure 2.5: A p-n junction band diagram and an illustration of the photovoltaic effect (reproduced from Ref. 20).

An ideal solar cell can be modelled as current generator in parallel with a p-n junction diode as seen in **Figure 2.6**. The resistance of the load determines how much current flows through the system after illumination or in dark conditions.

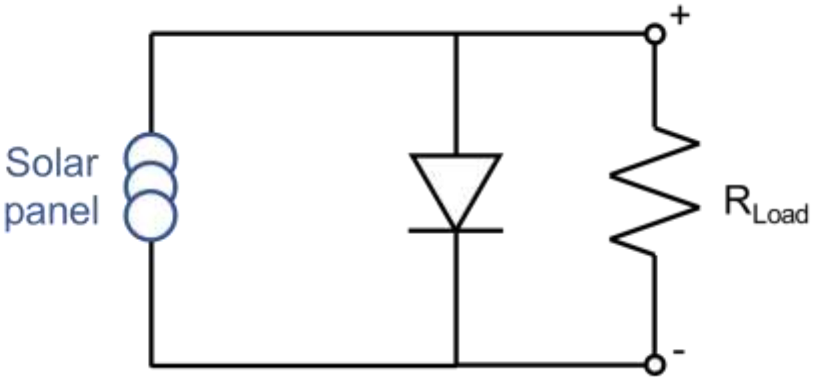

Figure 2.6: Equivalent circuit for an ideal solar cell.

The p-n junction within a solar cell exhibits diode characteristics that enables charge separation. The current of an ideal cell modelled in dark conditions is given by the following equation:[18]

$$I_{diode} = I_0(e^{\frac{qV}{k_BT}} - 1) \qquad [2.2]$$

where I_0 is the dark saturation current density, V is the applied bias voltage, k_B is the Boltzmann constant, and T is the temperature. Under illumination, the light-generated photocurrent (I_{ph}) contributes to the current given by equation (2.2) resulting in

$$I = I_{ph} - I_0\left(e^{\frac{qV}{k_BT}} - 1\right) \qquad [2.3]$$

An example of a current as a function of the applied voltage (I-V) plot is shown in **Figure 2.7**. The maximum output power and efficiency can be evaluated using the following equations,

$$P_{max} = V_{oc}J_{sc}FF \qquad [2.4]$$

$$PCE = \frac{P_{max}}{P_{in}} = \frac{V_{oc}J_{sc}FF}{P_{in}} \qquad [2.5]$$

where V_{oc} is the open-circuit voltage, J_{sc} the short-circuit current density (I/A , where A is the area), *FF* the fill factor and *PCE* the power conversion efficiency. The short-circuit current density is the current through a solar cell when the voltage across the solar cell is zero (when the device is short-circuited). The J_{sc} depends on the area of the solar cell, the incident light (power and spectrum), the optical properties of the solar active materials and the efficiency of the electron/hole extraction process. The open-circuit voltage is the maximum voltage obtained from a solar cell at zero current density. The fill factor (FF) is the parameter that determines the maximum power efficiency from a solar cell. The FF is the ratio between the maximum generated power and the theoretical power.[17] Usually, p_{in} is correlated to the standard spectrum at the Earth's surface and called AM1.5G, (AM for air mass coefficient and G for global, 1000 W/m^2).

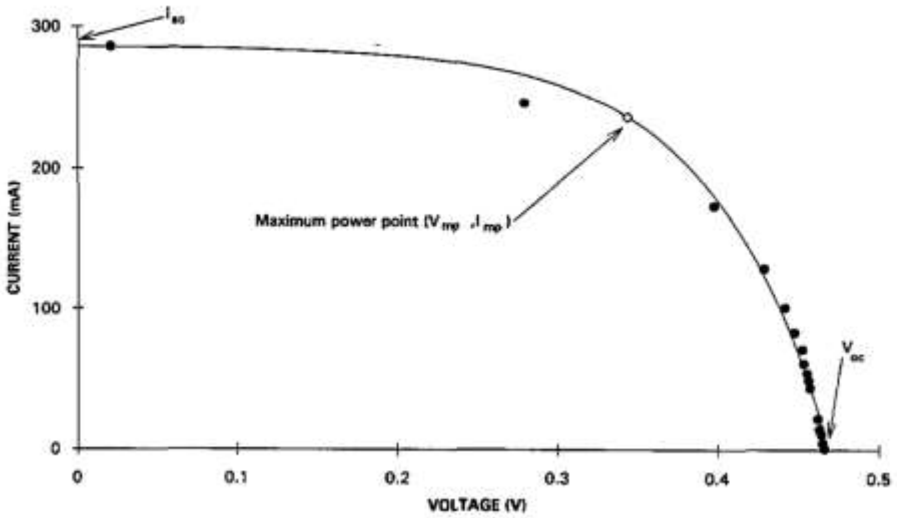

Figure 2.7: light I-V curves of a photovoltaic cell (reproduced from Ref. 21).

Two other important parameters that arise in real diode solar cells are the series (R_s) and shunt (R_{sh}) resistances. R_s is due to contact and bulk resistance within the overall solar cell circuit. The main impact of R_s is to reduce the *FF* and it may also reduce the short-circuit current. R_{sh}, on the other hand, is due to carrier recombination and needs to be maximized for optimal performance. In an ideal solar cell, R_s should be close to zero whereas R_{sh} should be as large as possible. **Figure 2.8** shows how R_s and R_{sh} are included in the equivalent solar cell circuit and the resulting effects on the current.

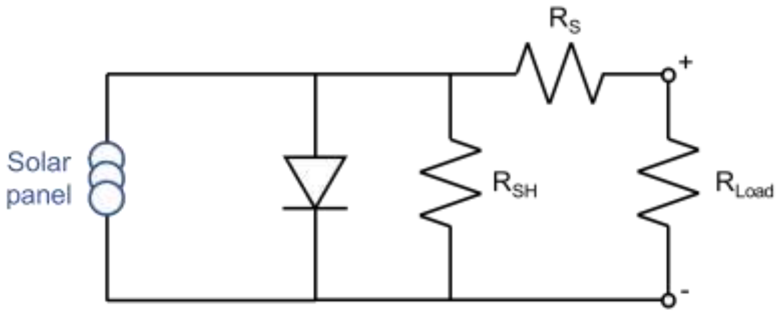

Figure 2.8: A schematic of a solar cell equivalent circuit with series and shunt resistances.

Considering these additional contributions, the non-ideal diode equation can then be written as follows:

$$I = I_{ph} - I_0\left(e^{\frac{q(V+IR_S)}{nk_BT}} - 1\right) - \frac{V+IR_S}{R_{sh}} \qquad [2.6]$$

Equation 2.2 is also modified with the addition of an ideality factor, *n*, given by

$$I = I_0(e^{\frac{qV}{nk_BT}} - 1) \qquad [2.7]$$

In an inorganic solar cell, the ideality factor (*n*) generally takes a value between 1 and 2. The low shunt resistance causes power losses by providing an alternative current path after the light-generated current. Moreover, the large series resistance can also cause power losses by consuming the generated power after the photons have been converted to excitons. Series and shunt resistances can be extracted by the slope of I-V curves:

$$R_s = -\left(\frac{dV}{dI}\right)_{where\ V=V_{oc}} \text{ and } R_{sh} = -\left(\frac{dV}{dI}\right)_{where\ I=I_{sc}} \qquad [2.8]$$

The external quantum efficiency (EQE) of a solar cell is a wavelength related parameter describing the ratio of the number of charge carriers collected by the solar cell to the overall number of incident photons. The EQE can be divided into several independent factors as follows:

$$EQE(\lambda) = R(\lambda) \cdot \frac{hc}{q\lambda} = \frac{J_{sc}}{I_n} \cdot \frac{hc}{q\lambda} \qquad [2.9]$$

Where R is the responsivity of solar cell, J_{sc} is the short circuit current density, I_n the illumination intensity, h is the Planck constant, c is the speed of light, and λ is the illumination wavelength. Besides demonstrating how the EQE can be determined, Equation 2.9 also shows that J_{sc} can be obtained by integrating over all EQE values across the spectrum, which should result in similar J_{sc} values to that obtained from solar cell measurements.

2.1.4. Current QD solar cell technology

Quantum dot solar cells (QDSC) have been intensively researched for the past decade and have shown rapid progress in terms of device improvements with power conversion efficiencies (PCE) now reaching more than 10%, which is comparable to that achievable with their organic counterparts. However, the PCE of QDSCs is still below the theoretical value, known as the Shockley-Queisser limit. The key challenges facing the performance of QDSCs are the synthesis of high-quality and mono-dispersed CQD solutions with ideal optical properties. It is also particularly important that high-quality

CQD films are formed (ideal QD lattice packing, surface passivation with short chain ligands, and conductive thin film properties) so as to lead to favorable behavior in terms of the photovoltaic effect. [22-25]

2.2 Electrochemical Energy Storage

2.2.1 Electrochemical energy storage system

The amount of energy generated by energy conversion systems such as the photovoltaic devices discussed in the previous section and the power consumed by end-users varies with time, location, function, and purpose. Hence, the efficient storage of electrical energy is strongly required. Clean electrochemical energy storage (EES) systems and devices (lithium-ion batteries (LIBs) and supercapacitors (SCs)) are expected to play essential roles in new power sources that can store electrical energy that would otherwise be wasted.[26-27] A typical LIB or SC system consists of a positive electrode (cathode), a negative electrode (anode), an electrolyte and a separator between the two electrodes (**Figure 2.9**).

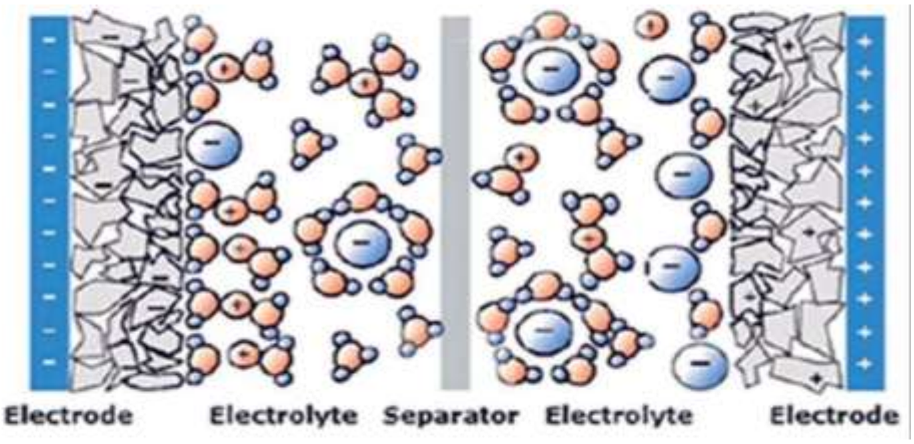

Figure 2.9: Schematic illustration of an EES system (reproduced from Ref. 28).

The energy storing principle relevant to both devices involves the migration of electrolyte ions (Li^+, Na^+, K^+, and H^+) or anions (OH^-) towards the electrodes for reversible electrochemical reactions.[29] For LIBs, the electrochemical reaction of Li^+ on the electrodes is realized by the intercalation, conversion and alloying reactions of Li^+ through to the inside of the electrodes. These conversion and alloying reactions usually require a long reaction time to store charges. However, for SCs, unlike ordinary capacitors, supercapacitors do not use a conventional solid dielectric, but rather, they use electrostatic double-layer capacitance (EDLC) and electrochemical pseudocapacitance. Both EDLCs and pseudocapacitors store charges through fast-physical adsorption of electrolyte ions on the surface of the electrodes. The electrochemical reaction of ions on the electrodes is realized through fast surface or near-surface reactions. Therefore, supercapacitive energy storage has the advantage of delivering large amounts of power over shorter timescales than that of LIBs. This characteristic demonstrates that SCs have a power density that far exceeds that of LIBs (**Figure 2.10**).[30-31]

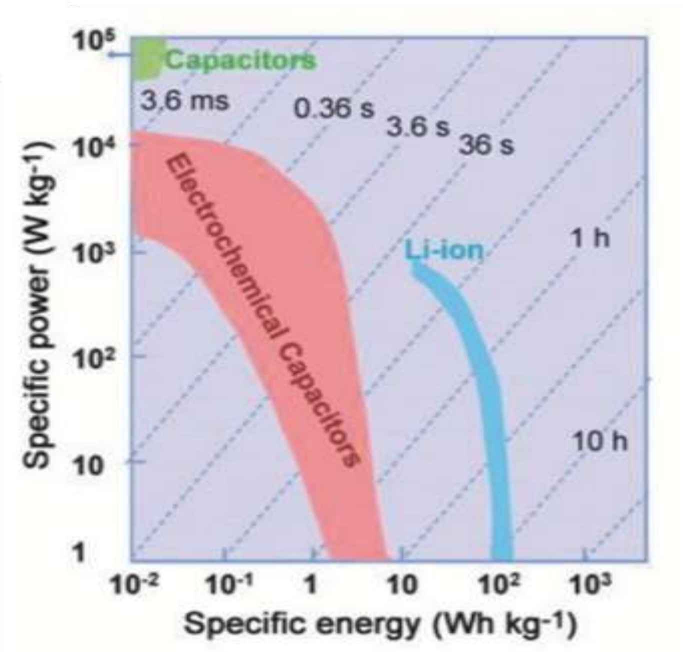

Figure 2.10: Ragone plot of energy-storing devices (reproduced from Ref. 32).

Generally, supercapacitors can store electricity in two different ways, which can be classified as either a non-Faradaic reaction process or a Faradaic redox reaction process on the electrodes. Non-faradaic technologies store electricity directly in an electrostatic way between the electrodes and the electrolyte and these are known as electric double-layer capacitors (EDLCs). EDLCs involve only the physical adsorption of electrolyte ions without any surface chemical reactions. Because there is no physical and chemical change on the electrodes, EDLCs are stable, and efficient (≈100%), but are only capable of storing a low energy density.[33-34] The other type of SCs are based on surface Faradaic redox reactions, termed pseudocapacitors. Pseudocapacitance involves storing energy based on Fast-redox reactions on the surface or near-surface region of the electrodes, where electrosorption/electrodesorption occurs for charge transfer (**Figure 2.11**). More recently, research on understanding pseudocapacitance behaviour has grown substantially because it can provide a higher energy density than EDLCs while maintaining a fast power delivery.[35-36] However, the electrodes undergo physical changes during the charge/discharge process resulting in relatively poor durability compared with EDLCs.

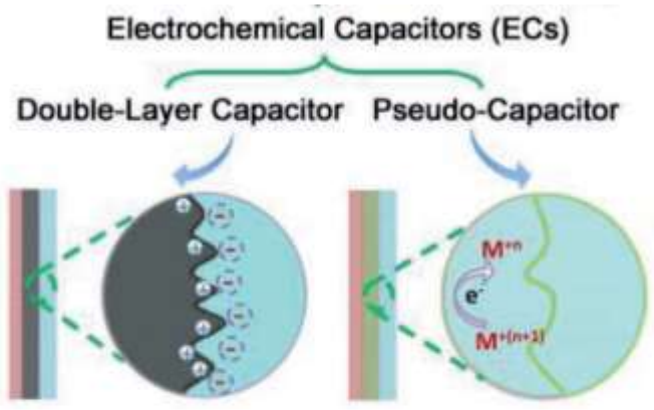

Figure 2.11: Schematic of electrochemical capacitance. Left image shows the electrostatic accumulation of charges on the electrodes, and right image shows the electrostatic and redox reactions of a transition metal (M) on the electrodes (reproduced from Ref. 37).

2.2.2 Charge storage mechanism in pseudocapacitors.

For the EES system, the capacitance can be calculated by the following equation[38]

$$C\ (capacitance) = \frac{Q}{V} = \frac{\varepsilon_0 k A}{d} \qquad [2.10]$$

where Q is the total charge on the plates, V is the voltage, A is the specific area of the electrode/electrolyte interface, d is the thickness of the electric double layer, ε_0 is the permittivity of free space and k is the dielectric constant of the electrolyte. However, pseudocapacitors store energy through fast-redox reaction processes on the surface of the electrodes upon charging/discharging, resulting in a potential-dependent accumulation of electrostatic charge by the following equation[39]

$$C_p\ (pseudocapacitance) = \frac{\Delta Q}{\Delta V} \qquad [2.11]$$

The energy density E and power density P of an electrochemical supercapacitor is also calculated by the following equations

$$E = \frac{1}{2} C_p V^2 \qquad [2.12]$$

$$P = \frac{E}{t} \qquad [2.13]$$

where C_p is the specific capacitance and V is the voltage applied on the cell. Upon charging/discharging, the redox system is a typical form of pseudocapacitance, where the mechanism involves the adsorption of electroactive ions onto the surface or near-surface region of the electrode materials and Faradaic reactions (Faradaic redox charge transfer) occur with the process of charge transfer. In particular, transition metal oxides and sulphides exhibit fast Faradaic redox reactions on their surface through the intercalation of protons (H^+), alkali metal cations ($C^+ = Na^+, K^+$, etc.), or hydroxyl ions (OH^-) as described by[40]

$$MX_2 + H^+ + e^- \leftrightarrow MXXH \qquad [2.14]$$

or

$$MX_2 + C^+ + e^- \leftrightarrow MXXC \qquad [2.15]$$

or

$$MX_2 + OH^- \leftrightarrow MXXOH + e^- \qquad [2.16]$$

where X represents either oxides or sulphides. Upon charging/discharging, no chemical transition occurs, but instead a molecular layer consisting of electrolyte ions is formed on the electrode surface and Faradaic reactions then occur to generate electrons.

2.2.3 Cyclic voltammetry (CV) curves

In a cyclic voltammetry (CV) experiment, a working electrode potential is ramped up linearly as a function of time in cyclical phases. The current measured at the working electrode is then plotted as a function of the applied voltage (that is, the working electrode's potential) to give the CV curve. CV measurements can be used to evaluate the average capacitance. The specific capacitance of electrode materials is calculated via a current-voltage (CV) analysis[41]

$$C = \frac{\int I dv}{2mv\triangle V} \qquad [2.17]$$

where m is mass of the electrode material (g), I is the voltammetric current, ΔV is the potential window (V), and v is the scan rate (mV s^{-1}). The area bounded by the CV curve for the electrodes reveals the absolute value for the electrochemical capacitance. Moreover, for CV measurements, the difference between the anodic and cathodic peak positions, $\Delta E_{a,c}$, as well as the voltage shift in the anodic and cathodic peaks with a change in v typically define the level of reversibility of the electrochemical reactions. For example, when $\Delta E_{a,c}$ is small or remains constant, then the electrode is considered to have a high level of reversibility.[42]

2.2.4 Galvanostatic charge-discharge curves

The profile of Galvanostatic Charge-Discharge (GCD) curves for EDLCs is a well-defined linear shape. In contrast, for pseudocapacitor electrodes the curves always exhibit slight potential plateaus. The GCD curves indicate the specific capacitance and rate retention of the electrodes as a function of charge/discharge current densities. The specific capacitance that can be obtained from GCD curves can be calculated according to the following equation[41]

$$C_m = \frac{I_d * t}{\triangle V * m} \qquad [2.18]$$

where C_m is the specific gravimetric capacitance, I_d is the discharge current, t is the discharge time, $\triangle V$ is the operating potential during the discharge process, and m is the mass of the active material. From a low current density to a high current density, the rate retention of the electrodes is determined from the capacitance ratio between the low current and high current densities.

2.2.5 Nanostructured electrodes

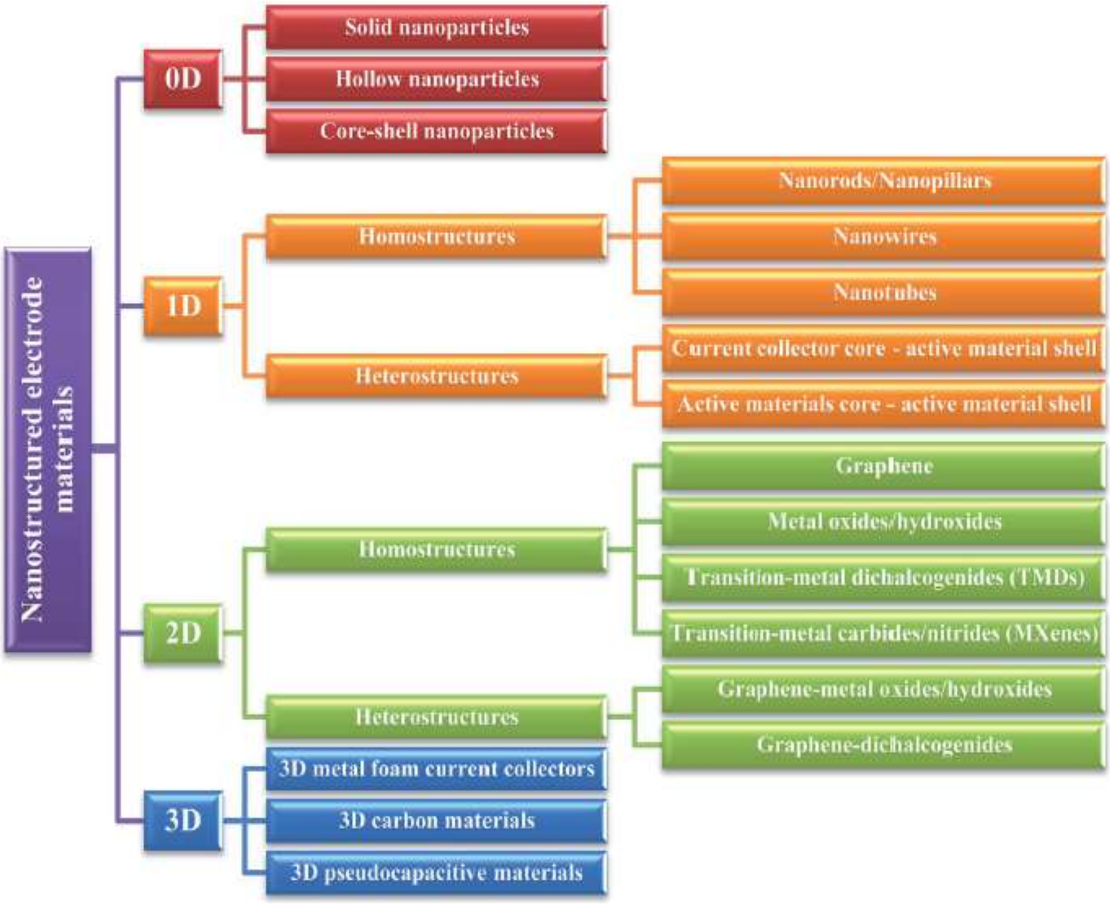

Figure 2.12: A schematic summarizing the range of electrode materials from 0 to 3-dimensions (reproduced from Ref. 43).

To realize high performance supercapacitor electrodes, there are many factors that determine the overall performance: specific capacitance, rate capability, and cycle stability. Usually, charges are stored on the surface of the electrodes. Electrodes with a higher surface area can provide more opportunity for surface interactions between the electrodes and the electrolyte ions. The high electronic conductivity of electrodes also considerably affects the specific capacitance and rate capability, and subsequently results in fast charge transfer after the adsorption/desorption of the electrolyte ions on the electrodes. The mechanical and chemical stability of the electrodes can be an important parameter to evaluate the performance of supercapacitors. How to protect the phase change, side reaction and volume expansion of electrode materials are key parameters to boost the stability during charge/discharge cycling. The performance of supercapacitors can be effectively manipulated using a nanostructured design due to their unique storage mechanism when materials are reduced to a small size.

Nanomaterials can be classified into zero dimensional (0D), one dimensional (1D) and two dimensional (2D) (**Figure 2.12**).[44-48]. Those nanostructures can generally provide large surface areas because of their high surface-to-volume ratio, and the large surface area of electrodes, which is usually expected to result in a higher specific capacitance. The confinement over small-scale structures can provide efficient transport pathways for both electrons and ions. Moreover, their unique structural properties can effectively decrease the unstable surface energy which reduces the aggregation possibility of active materials, resulting in better reversibility and cyclic stability of the electrodes.

2.3 Experimental Procedures

Atomic force microscopy (AFM) measurement was carried out by Veeco Dimension 3100. Scanning electron microscopy (SEM) measurement was carried out FEI Quanta 600 FEG. Transmission electron microscopy (TEM) and selected area (electron) diffraction (SAED) measurement were carried out by TEM spectroscopy (JEM-2100 and

JEM-2200MCO FEGTEM, JEOL). X-ray powder diffraction (XRD) measurement was carried out by Rigaku Medel Smartlab in a two-theta range. X-ray photoelectron spectroscopy (XPS) was carried out using a Thermo Scientific K-Alpha XPS instrument equipped with a micro-focused mono-chromated Al X-ray source. Ultraviolet–visible (UV-Vis) spectroscopy measurement was carried out by cary5000 UV-VIS. Steady-state photoluminescence (PL) measurements were carried out by an automated spectrofluorometer (Fluorolog, Horiba Jobin Yvon). Time-resolved photoluminescence (TR-PL) measurement was carried out using a time-correlated single photon counting apparatus (FluoTime 300, PicoQuant GmbH) with a NIR-PMT detector assembly (H10330A-45, Hamamatsu). Solar cell measurements were performed using a source meter (Keithley 4200-SCS) and a solar simulator (LOT-Quatum Design) with an AM 1.5 G filter (100 mW cm^{-2}). The electrochemical properties of samples were performed using a potentiostat (PGSTAT302N, Metrohm, Autolab).

2.4 Concluding Remarks

This chapter offers an overview and literature review of basic principles in the synthesis, design, experiments and characterization of nanostructured materials and energy conversion and storage applications. This chapter reviews the major concept of nanostructures, and then introduce some of the most important parameters to characterize their energy conversion and storing performance. Finally, experimental procedures are discussed for further information.

2.5 References

[1] P. Alivisatos, "Semiconductor clusters, nanocrystals, and quantum dots," Science, vol. 271, no. 5251, p. 933, 1996.

[2] A. D. Yoffe, "Low-dimensional systems: quantum size effects and electronic properties of semiconductor microcrystallites (zero-dimensional systems) and some quasi-two-dimensional systems," Adv. Phy., vol. 42, no. 2, p. 173, 1993.

[3] P. Kamat, "Quantum dot solar cells. semiconductor nanocrystals as light harvesters," J. Phys. Chem. C, vol. 112, no. 48, p. 18737, 2008.

[4] M. A. Hines, and G. D. Scholes, "Colloidal PbS nanocrystals with size-tunable near-infrared emission: observation of post-synthesis self-narrowing of the particle size distribution," Adv. Mater., vol. 15, no. 21, p. 1844, 2003.

[5] W. Parka, L. Manna, F. Simmel, D. Gerion, and P. Alivisatos, "Nanoparticles: from theory to application," WILEY-VCH Verlag GmbH & Co.: Weinheim, 2004.

[6] C. Kagan, and C. B. Murray, "Charge transport in strongly coupled quantum dot solids," Nat. Nanotech., vol. 10, no. 12, p. 1013, 2015.

[7] C. Kagan, E. Lifshitz, E. Sargent, and D. Talapin, "Building devices from colloidal quantum dots," Science, vol. 353, no. 6302, p. aac5523, 2016.

[8] C. B. Murray, D. J. Norris, and M. G. Bawendi, "Synthesis and characterization of nearly monodisperse CdE (E = sulfur, selenium, tellurium) semiconductor nanocrystallites," J. Am. Chem. Soc., vol. 115, no. 19, p. 8706, 1993.

[9] I. Moreels, K. Lambert, D. Smeets, D. Muynck, T. Nollet, J. Martins, F. Vanhaecke, A. Vantomme, C. Delerue, G. Allan, and Z. Hens, “Size-dependent optical properties of colloidal PbS quantum dots,” Acs Nano, vol. 3, no. 10, p. 3023, 2009.

[10] D. Talapin, J.-S. Lee, M. Kovalenko, and E. Shevchenko, “Prospects of colloidal nanocrystals for electronic and optoelectronic applications,” Chem. Rev., vol. 110, no. 1, p. 389, 2010.

[11] Y. Wang, and Y. Xia, “Bottom-up and top-down approaches to the synthesis of monodispersed spherical colloids of low melting-point metals,” Nano Lett., vol. 4, no. 10, p. 2047, 2004.

[12] G. Carey, A. Abdelhady, Z. Ning, S. Thon, O. Bakr, and E. Sargent, “Colloidal quantum dot solar cells,” Chem. Rev., vol. 115, no. 23, p. 12732, 2015.

[13] K. E. Jasim, “Quantum dots solar cells (Ch. 11),” Solar Cells Leonid A. Kosyachenko, IntechOpen, DOI: 10.5772/59159, 2015.

[14] C.-H. Chuang, P. Brown, V. Bulović, and M. Bawendi, “Improved performance and stability in quantum dot solar cells through band alignment engineering,” Nat. Mater., vol. 13, no. 8, p. 796, 2014.

[15] A. Ip, S. Thon, S. Hoogland, O. Voznyy, D. Zhitomirsky, R. Debnath, L. Levina, L. Rollny, G. Carey, A. Fischer, K. Kemp, I. Kramer, Z. Ning, A. Labelle, K. Chou, A. Amassian, and E. Sargent, “Hybrid passivated colloidal quantum dot solids,” Nat. Nanotech., vol. 7, no. 9, p. 577, 2012.

[16] P. Brown, D. Kim, R. Lunt, N. Zhao, M. Bawendi, J. Grossman, and V. Bulović, "Energy level modification in lead sulfide quantum dot thin films through ligand exchange," Acs Nano, vol. 8, no. 6, p. 5863, 2014.

[17] A. Luque, and S. Hegedus, "Handbook of photovoltaic science and engineering," John Wiley & Sons, 2011.

[18] J. Nelson, "The physics of solar cells," Imperial College Press: London, 2003.

[19] M. Shanawani, D. Masotti, and A. Costanzo, "THz rectennas and their design rules," Electronics, vol. 6, no. 99. P. 1, 2017.

[20] P. Wurfel, "Physics of solar cells: from basic principles to advanced concepts," Wiley-VCH, 2009.

[21] M. Morgan, G. Jakovidis, and I. Mcleod, "An experiment to measure the I-V characteristics of a silicon solar cell," Phys. Educ., vol 29, no. 252, p. 252, 1994.

[22] M. Liu, O. Voznyy, R. Sabatini, P. de Arquer, R. Munir, A. Balawi, X. Lan, F. Fan, G. Walters, A. Kirmani, S. Hoogland, F. Laquai, A. Amassian, and E. Sargent, "Hybrid organic–inorganic inks flatten the energy landscape in colloidal quantum dot solids," Nat. Mater., vol. 16, no. 2, p. 258, 2016.

[23] S. Pradhan, A. Stavrinadis, S. Gupta, S. Christodoulou, and G. Konstantatos, "Breaking the open-circuit voltage deficit floor in PbS quantum dot solar cells through synergistic ligand and architecture engineering," ACS Energy. Lett., vol. 2, no. 6, p.1444, 2017.

[24] M. R. Kim, and D. Ma, "Quantum-dot-based solar cells: recent advances, strategies, and challenges," J. Phys. Chem. Lett., vol. 6, no. 1, p. 85, 2015.

[25] G. Shi, Y. Wang, Z. Liu, L. Han, J. Liu, Y. Wang, K. Lu, S. Chen, X. Ling, Y. Li, S. Cheng, and W. Ma, "Stable and highly efficient PbS quantum dot tandem solar cells employing a rationally designed recombination layer," Adv. Energy Mater., vol. 7, no. 15, p. 1602667, 2017.

[26] B. Dunn, H. Kamath, and J.-M. Tarascon, "Electrical energy storage for the grid: A battery of choices," Science, vol. 334, no. 6058, p. 928, 2011.

[27] Z. Yang, J. Zhang, M. Kintner-Meyer, X. Lu, D. Choi, J. Lemmon, and J. Liu, "Electrochemical energy storage for green grid," Chem. Rev., vol. 111, no. 5, p. 3577, 2011.

[28] X. Rui, H. Tan, and Q. Yan, "Nanostructured metal sulfides for energy storage," Nanoscale, vol. 6, no. 17, p. 9889, 2014.

[29] B. E. Conway, "Electrochemical supercapacitors: scientific fundamentals and technological applications," Springer Science + Business Media, 1999.

[30] A. Gonzlez, E. Goikolea, J. A. Barrena, and R. Mysyk, "Review on supercapacitors: technologies and materials," J. Renew. Sustain. Energy, vol. 58, no. 1, p. 1189, 2016.

[31] C. Liu, F. Li, L. Ma, and H. Cheng, "Advanced materials for energy storage," Adv. Energy Mater., vol. 22, no. 8, p. E28, 2010.

[32] P. Simon, and Y. Gogotsi, "Materials for electrochemical capacitors," Nat. Mater., vol. 7, no. 11, p. 845, 2008.

[33] X. Chen, R. Paul, and L. Dai, "Carbon-based supercapacitors for efficient energy storage," Natl. Sci. Rev., vol. 4, no. 3, p. 453, 2017.

[34] H. Ji, X. Zhao, Z. Qiao, J. Jung, Y. Zhu, Y. Lu, L. Zhang, A. MacDonald, and R. Ruoff, "Capacitance of carbon-based electrical double-layer capacitors," Nat Commun, vol. 5, no. 1, p. 3317, 2014.

[35] V. Augustyn, P. Simon, and B. Dunn, "Pseudocapacitive oxide materials for high-rate electrochemical energy storage," Energy Environ. Sci., vol. 7, no. 5, p. 1597, 2014.

[36] Z. Wu, Y. Zhu, and X. Ji, "$NiCo_2O_4$-based materials for electrochemical supercapacitors," J. Mater. Chem. A, vol. 2, no. 36, p. 14759, 2014.

[37] J. Liu, J. Wang, C. Xu, H. Jiang, C. Li, L. Zhang, J. Lin, and Z. Shen, "Advanced energy storage devices: basic principles, analytical methods, and rational materials design," Adv. Sci. vol. 5, no. 1, p. 1700322, 2018.

[38] L. L. Zhang, and X. S. Zhao, "Carbon-based materials as supercapacitor electrodes," Chem. Soc. Rev., vol. 38, no. 9, p. 2520, 2009.

[39] B. E. Conway, "Transition from 'supercapacitor' to 'battery' behavior in electrochemical energy storage," J. Electrochem. Soc., vol. 138, no. 6, p. 1539, 1991.

[40] Y. Wang, Y. Song, and Y. Xia, "Electrochemical capacitors: mechanism, materials, systems, characterization and applications," Chem. Soc. Rev., vol. 45, no. 21, p. 5925, 2016.

[41] J. Theerthagiri, Karuppasamy, G. Durai, A. Rana, P. Arunachalam, K. Sangeetha, P. Kuppusami, and H.-S. Kim, "Recent advances in metal chalcogenides (MX; X = S, Se) nanostructures for electrochemical supercapacitor applications: a brief review," Nanomater., vol. 8, no. 4, p. 256, 2018.

[42] L. Mai, H. Li, Y. Zhao, L. Xu, X. Xu, Y. Luo, Z. Zhang, W. Ke, C. Niu, and Q. Zhang, "Fast ionic diffusion-enabled nanoflake electrode by spontaneous electrochemical pre-intercalation for high-performance supercapacitor," Sci. Rep., vol. 3, no. 1, p. 1718, 2013.

[43] Z. Yu, L. Tetard, L. Zhai, and J. Thomas, "Supercapacitor electrode materials: nanostructures from 0 to 3 dimensions," Energy Environ. Sci., vol. 8, no. 3, p. 702, 2014.

[44] H. Jia, Y. Cai, J. Lin, H. Liang, J. Qi, J. Cao, J. Feng, and W. Fei, "Heterostructural graphene quantum dot/MnO_2 nanosheets toward high-potential window electrodes for high-performance supercapacitors," Adv. Sci., vol. 5, no. 5, p. 1700887, 2018.

[45] G. Zhang, X. Xiao, B. Li, P. Gu, H. Xue, and H. Pang, "Transition metal oxides with one-dimensional/one-dimensional-analogue nanostructures for advanced supercapacitors," J. Mater. Chem. A, vol. 5, no. 18, p. 8155, 2017.

[46] W. Wei, X. Cui, W. Chen, and D. Ivey, "Manganese oxide-based materials as electrochemical supercapacitor electrodes," Chem. Soc. Rev., vol. 40, no. 3, p. 1697, 2010.

[47] C. Yuan, J. Li, L. Hou, X. Zhang, L. Shen, and X. Lou, "Ultrathin mesoporous $NiCo_2O_4$ nanosheets supported on Ni foam as advanced electrodes for supercapacitors," Adv. Funct. Mater., vol. 22, no. 21, p. 4592, 2012.

[48] E. Pomerantseva, and Y. Gogotsi, "Two-dimensional heterostructures for energy storage," Nat. Energy, vol. 2, no. 7, p. 17089, 2017.

Chapter 3. Quantum Dot Synthesis and Characterization

3.1 Introduction

In 1993, a highly efficient synthetic method for producing colloidal quantum dots (CQDs) was introduced by C. B. Murray, D. J. Norris and M. G. Bawendi and involves a high-temperature colloidal synthesis process with a fast precursor injection method.[1] Due to the unique band gap tunability and solution processability of this method, colloidal synthesis provides an excellent opportunity for the practical implementation of CQDs in solar energy conversion devices.[2-3] In particular, lead-based CQDs such as lead sulphide (PbS) and lead selenide (PbSe) have shown to be, potentially, the most attractive forms of CQDs, possessing large Bohr radius (~ 10 nm) for enhanced quantum confinement effects.[4-5] Moreover, PbS CQDs exhibit strong light absorption across the ultraviolet-visible-near infrared spectrum depending upon their size and band gap.[6-7] In addition, due to their solution processability, PbS CQD films can be synthesized at low-cost, low-temperature and can be used for large area fabrication. The broad absorption spectrum of PbS CQDs allows for the incorporation of thin CQD films into solar cells with high power conversion efficiencies (PCE). As shown in **Figure 3.1**, PbS CQDs of different diameters can harvest different portions of the solar spectrum and, therefore, the development of efficient and facile colloidal synthetic routes for PbS CQDs need to be developed to precisely tune the band gap and size of the CQDs for solar cell applications.

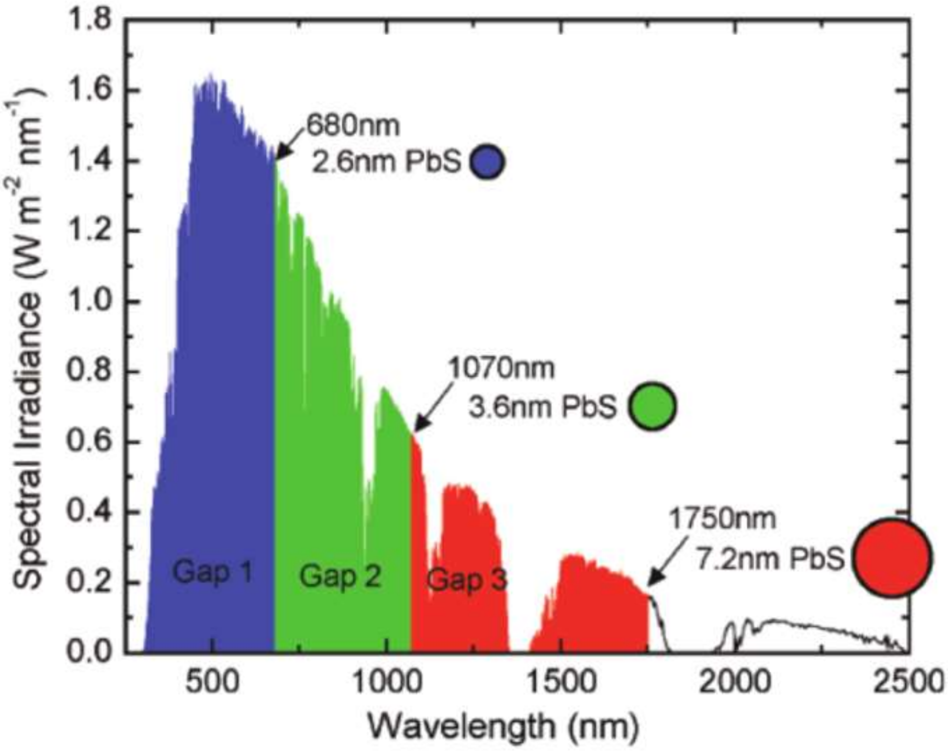

Figure 3.1: The spectral irradiance of PbS QDs at different sizes and band gaps (reproduced from Ref. 8).

Most CQDs are prepared using a hot-injection colloidal synthesis process, and control of the size of the resultant QDs can be achieved by varying the reaction temperature, time and ligand-to-precursor ratio. Principally, the colloidal hot-injection method includes (1) the rapid injection of precursor(s), (2) nucleation and (3) crystal growth stages (**Figure 3.2**).[9] The injection temperature and the magnitude of the precursor ratios are important, as they regulate the decomposition of the reaction precursor(s). After the injection process, small nuclei are formed due to the induced supersaturation status of the precursors and solvents, and the injection is then accompanied by burst-like nucleation sites at the high reaction temperature. The reaction temperature is maintained throughout the nanocrystalline growth process. The growth time is also an important parameter in the control of the size of CQDs. Finally, after the crystal growth process, a rapid decrease in the reaction temperature leads to the termination of the nucleation and growth steps. CQDs with different diameters result in electronic band gap levels of different magnitudes and can be used selectively in the diverse wavelength range required for solar cells. Controlling the synthesis parameters is of paramount importance when preparing high quality and size-dependent PbS CQDs for solar cell applications. In this Chapter, both conventional and novel synthetic methods are considered in order to precisely tailor the sizes of PbS CQDs ranging from small (0.8-1.4 eV) to large electronic band gaps (1.8-3.0 eV). In addition, the various characterization techniques used to analyze PbS CQDs are also explained in detail in this chapter.

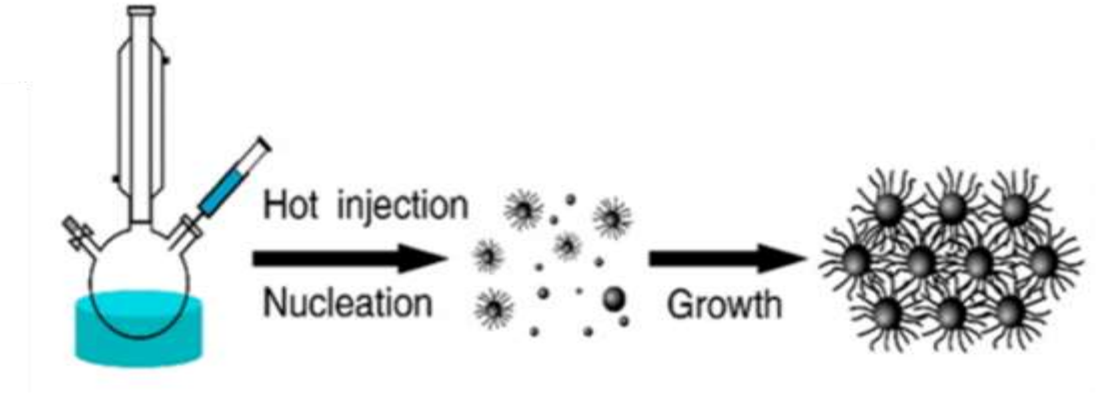

Figure 3.2: Schematic illustration of CQD synthesis (reproduced from Ref. 9).

3.2 1.3 eV PbS CQDs

PbS CQDs with an absorption peak at 980nm (1.3 eV) were synthesized by a colloidal synthesis (**Figure 3.3**).[10] First, a lead precursor solution was produced by mixing lead oxide (PbO, 0.47 g), oleic acid (OA, 18 g) and 1-octadecene (ODE, 10 g) in a 50 ml two-neck flask and then heated to 100 °C under vacuum (a transparent Pb precursor solution). For further treatment, the lead precursor solution was then heated to 130 °C for 1hr under argon to increase the precursor reaction kinetics. Separately, a sulphur precursor solution was also produced by mixing hexamethyldisilathiane (TMS, 210 μL) and ODE (6.4 mL) in a 50 ml two-neck flask and treated at room temperature under argon (the transparent S precursor solution). After a certain amount of time, the PbS CQD synthesis was completed by the rapid injection of the sulphur precursor solution into the lead precursor solution. After fast and hot injection, the two-neck flask with the PbS CQD solution (black solution) was cooled down to room temperature. Finally, the PbS CQDs were purified using a centrifuge. A further wash was applied to the extracted quantum dots and the PbS CQDs were finally dispersed in toluene to produce a 50 mg ml^{-1} solution.

The band-gap of the as-prepared ~1.3 eV PbS CQDs were evaluated using ultraviolet–visible (UV-Vis) spectroscopy. UV-Vis spectroscopy at 400-1500 nm region is an excellent tool for identifying the band gap characteristics of nanocrystals. As shown in **Figure 3.4**, the as-synthesized PbS CQDs exhibited an absorption peak close to a wavelength of 980 nm, corresponding to a band gap energy of ~1.3 eV as determined from the Planck–Einstein relation.

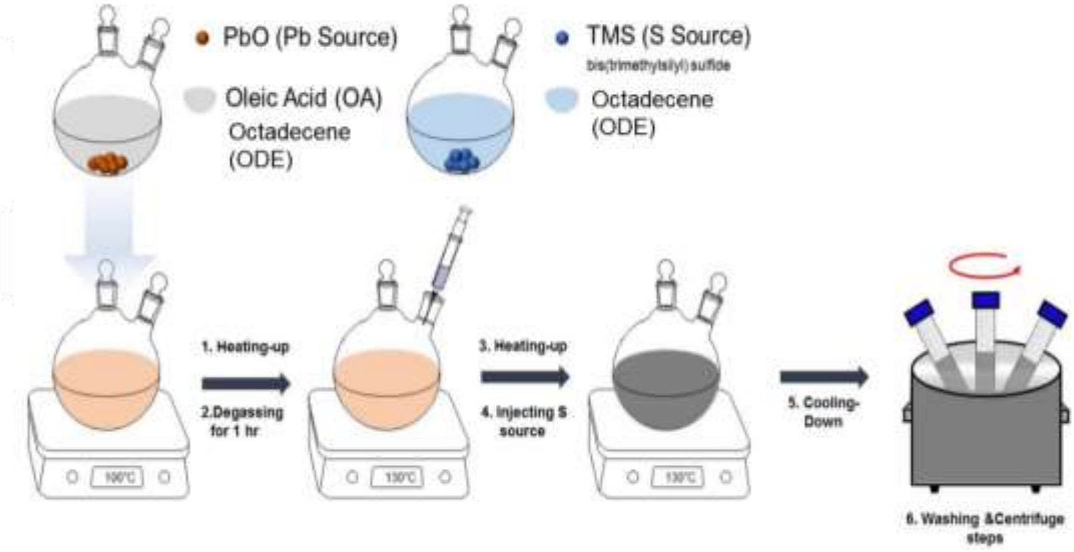

Figure 3.3: Schematic illustration of the synthesis of PbS CQDs using a colloidal fabrication process. preparation and synthesis steps.

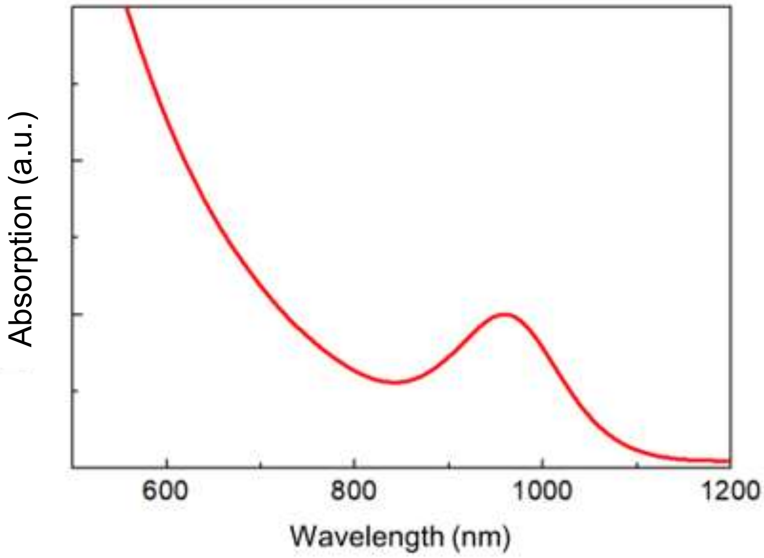

Figure 3.4: Absorption spectrum of PbS CQD with an electronic band gap of 1.3 eV (the size of the QDs was ~ 3 nm, the 10 mg ml^{-1} solution in toluene).

3.3 Band Gap-Controlled PbS CQDs (Low Band Gap Region)

The size of CQDs generally depends on the reaction time of the growth stage of the colloidal synthesis process. The reaction time is defined as the time that after the fast and hot injection, the flask is maintained at a temperature before the cool down process. A long growth reaction time typically results in CQDs with a large diameter (a small electronic band gap). Alternatively, a short growth reaction time leads to CQDs with a small diameter and consequently a large electronic band gap. However, the control of reaction time can cause inconsistent results (inconsistent band gaps) as the reaction time for the growth stage occurs within an extremely short time frame (~ 20 s) and the cool down process also requires the time which can increase the overall reaction time.

In this work, to obtain the CQDs with the excellent monodispersity and the precise control of electronic band gaps, the reaction time with the cool down was fixed and instead the ratio between PbO and long ligand chains (oleic acids) was adjusted. The mole ratio between the PbO and OAs was set equal to 1:2, 1:3, 1:8, 1:16, or 1:27 (**Table 3.1**). During the synthesis, other parameters that also influence the size of the PbS CQDs (i.e. the reaction time and temperature) were fixed at 130 °C injection temperature and 20 s reaction time. With a small number of OAs, many of the PbO precursors are converted to a large number of monomers for further growth, and the high initial monomer concentration can subsequently result in the formation of small-sized CQDs (large band gap). In this regard, a large amount of OA (low initial monomer) will result in the formation of large PbS CQDs (small band gap).

Sample	Peak(Band gap)	PbO	OA	PbO:OA	TMS(S)	Injected Temp.	Reaction Time
Sample 1	1.37 eV	0.47 g(2mmol)	1.49 mL (4mmol)	1 : 2	210 µL	130 °C	20 s
Sample 2	1.30 eV	0.47 g(2mmol)	2.25 mL (6mmol)	1 : 3	210 µL	130 °C	20 s
Sample 3	1.15 eV	0.47 g(2mmol)	5.96 mL (16mmol)	1 : 8	210 µL	130 °C	20 s
Sample 4	0.95 eV	0.47 g(2mmol)	12.67 mL (34mmol)	1 : 16	210 µL	130 °C	20 s
Sample 5	0.84 eV	0.47 g(2mmol)	20.12 mL (54mmol)	1 : 27	210 µL	130 °C	20 s

Table 3.1: The synthesis parameters for quantum dots of different diameters and electronic band gaps.

To characterize the as-prepared PbS CQDs, the material properties were determined by a combination of UV-Vis spectroscopy, Fourier-transform infrared (FT-IR) spectroscopy, X-ray diffraction (XRD), and transmission electron microscopy (TEM). **Figure 3.5**a presents examples of the absorption spectra used to evaluate the size distribution and the variation in the band gap of the as-prepared PbS CQDs. The observed peak absorption wavelength of the as-prepared PbS CQDs corresponds to band gaps ranging from 0.84 to 1.37 eV. Therefore, it can be clearly confirmed that different mole ratios between the PbO and OA precursors can precisely control the band gap of the PbS CQDs when the same reaction temperature and time are used. Moreover, the degree of monodispersity of the CQDs can be determined from the full width at half maximum (FWHM) of the absorption spectrum at 1000 nm region. All FWHM values of the UV-Vis peaks are less than 150 nm, indicating that relatively monodisperse PbS CQDs were prepared.

For the sample preparation, the CQD solution was spin-coated on a Si substrate. As shown in **Figure 3.5**b, the FT-IR spectra (from 2000-3500 nm) of the as-prepared PbS CQDs reveals the existence of long alkane chains at the surfaces of the CQDs. There are two dominant peaks, which correspond to symmetric stretching (2854 cm^{-1}) and asymmetric stretching (2924 cm^{-1}) of the $-CH_2$ bonds.[11] These two peaks are the primary signatures that indicate that the oleic acid is strongly attached to the surface of the PbS CQDs. XRD analysis of the as-prepared PbS CQDs was also carried out to determine the crystallography during the growth of the nanocrystals. A rock-salt cubic crystal structure is revealed for the different sizes of PbS CQDs (referring to PDF card 78-1057). The XRD peaks correspond to the (111), (200), (220) and (311) planes of the PbS crystalline structure (**Figure 3.5**c).[12] The high crystallinity and the rock-salt cubic crystal structure of the as-prepared PbS CQDs are also demonstrated in high-resolution TEM (HRTEM) images (**Figure 3.5**d-h). The TEM images of the as-prepared 1.37, 1.3, 1.15, 0.95 and 0.84 eV PbS CQDs show the size of the nanocrystals to be ~2.3, ~2.6, ~3.5, ~5.2 and ~5.8 nm, respectively, corresponding to synthetic molar ratios of PbO:OA of 1:2, 1:3, 1:8, 1:16 and 1:27, respectively.

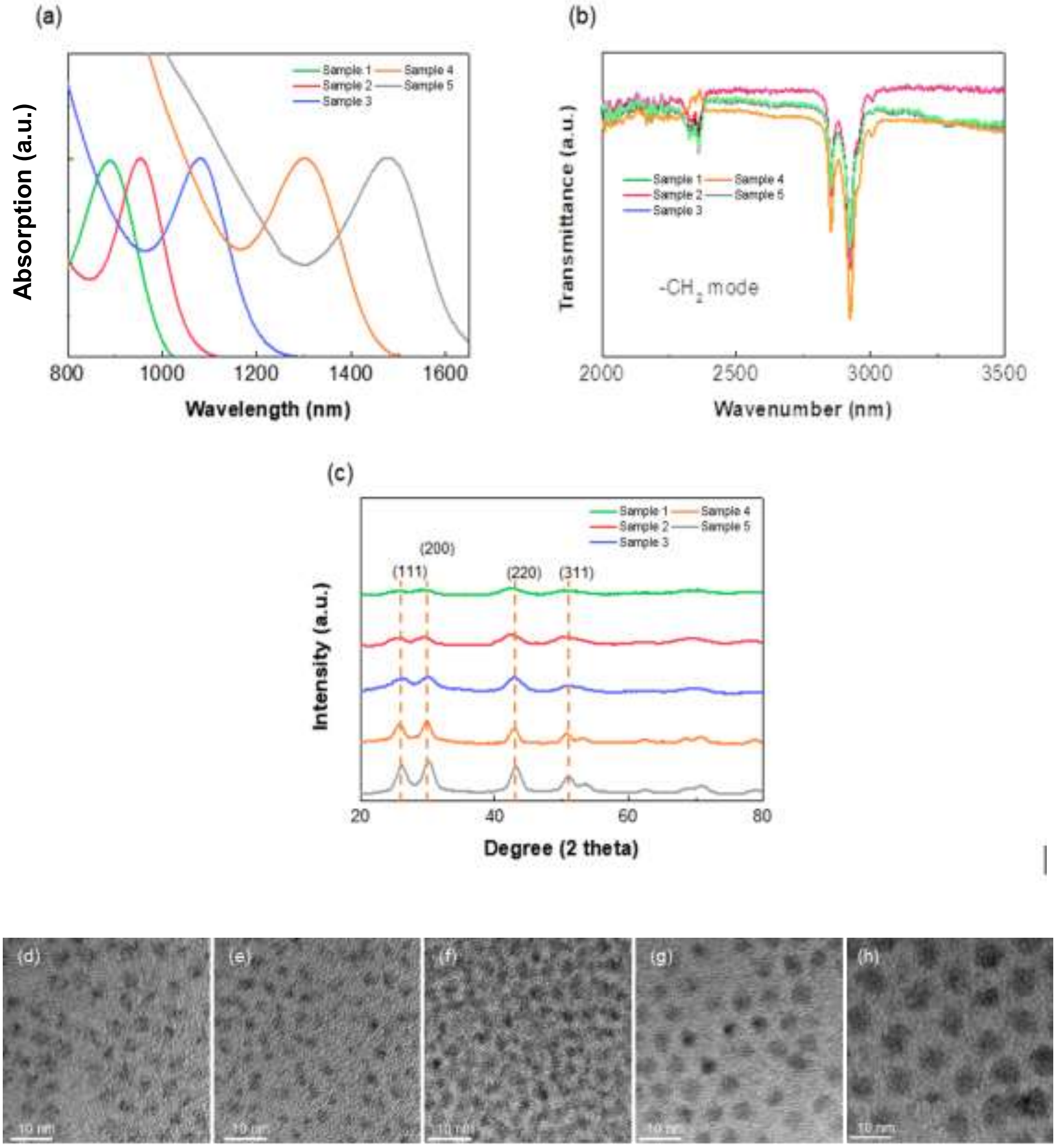

Figure 3.5: CQD characterization. (a) UV-Vis spectroscopy (the 10 mg ml^{-1} solution in toluene), (b) FT-IR spectroscopy, (c) XRD, (d-h) TEM images of (d) 0.84, (e) 0.95, (f) 1.15, (g) 1.30, and (h) 1.37 eV quantum dots, respectively. (TEM images were taken by Dr. Bo Hou).

3.4 Band Gap-Controlled PbS CQDs (Large Band Gap Region)

The need for large band gap PbS CQDs has increased dramatically, mainly due to their performance in QDSCs. The reason for this is that, even though the best performing QDSCs show considerably large short-circuit currents (J_{sc}) and fill factors (FF), their open circuit voltage, V_{oc}, of around 0.6 V remains lower than the estimated band gap of the PbS CQDs. Using the larger band gap of PbS CQDs might be an alternative way in which to increase the overall V_{oc} values. Therefore, there has been a high demand for producing larger band gap PbS QDs so as to compensate for the open circuit voltage (V_{oc}) deficiency.[13] However, due to limitations in the synthetic techniques, PbS CQDs with large band gaps have not been precisely realized.

The general hot-injection method is undoubtedly the best method for producing high-quality CQDs that has been reported to date. Unfortunately, the hot-injection methods are prohibitive in terms of producing extremely small diameter PbS CQDs and thus band gaps above 1.6 eV cannot be easily obtained by the method. Instead of using a hot-injection method, this work demonstrates that large band gap of PbS CQDs can be obtained by slowing down the reactivity of the sulphur precursors through the use of different sulphur sources and reaction temperatures. This is shown in **Figure 3.6**.

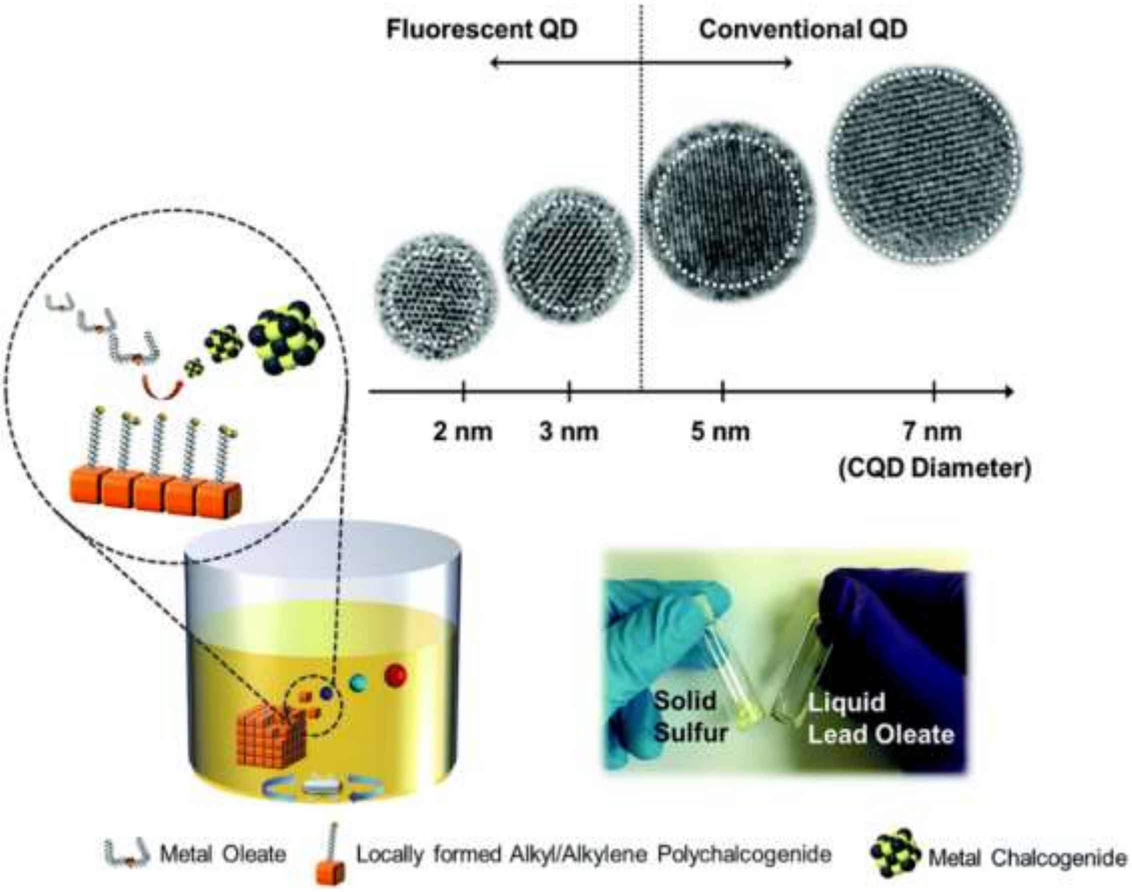

Figure 3.6: An illustration of the proposed synthesis method for large band gap PbS CQDs. (reproduced from Ref. 14).

The primary idea underpinning the synthesis of wide band gap PbS CQDs is to control the reaction activity of the precursors from the beginning of low reaction temperature. More specifically, the injected sulphur solution source at the general hot temperature can induce the unintentional reaction temperature and nucleation variance. In this project, we used the solid sulphur source and the reaction temperature was increased from the room temperature. The concentration of the OA was fixed to achieve equal particle stabilization. A solid-state sulphur was employed as the S source and lead oleate-dispersed ODE was employed as the Pb source. More specifically, the solid-state sulphur was injected into the Pb solution, after the Pb precursor solution was cooled down to room temperature. Then, the reaction temperature of the flask was elevated at a ramp rate of 0.2 °C s^{-1}, and the small sizes of PbS CQDs were formed at the different reaction temperatures. With the elevation of the reaction temperature, the alkyl or alkylene polysulphide was formed in the solution (**Figure 3.7**). Moreover, due to the high enthalpy of the solid sulphur bonds, no detectable reaction appeared below 150 °C, and large band gap PbS CQDs (the small sizes) can only be formed when the reaction occurs above 170 °C. The optical properties extracted from the fabricated PbS CQDs with the solid sulphur source are summarized in **Table 3.2**.

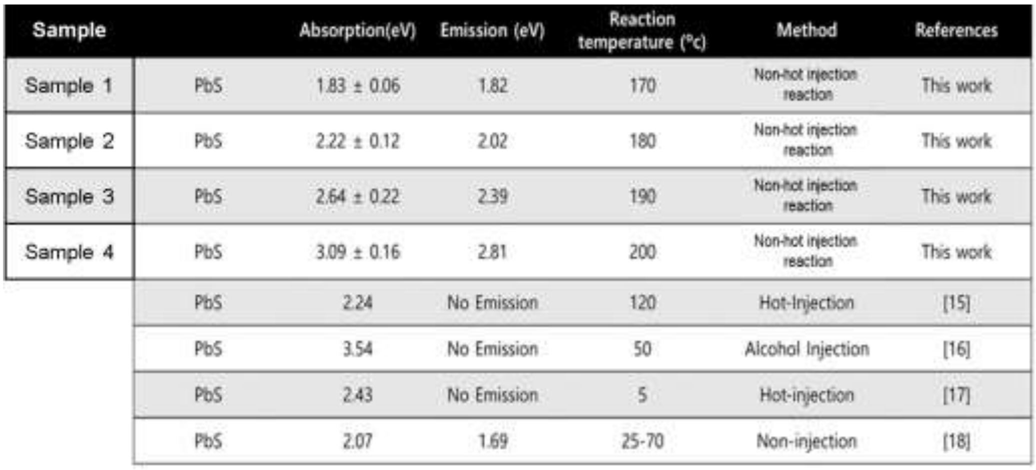

Sample		Absorption(eV)	Emission (eV)	Reaction temperature (°c)	Method	References
Sample 1	PbS	1.83 ± 0.06	1.82	170	Non-hot injection reaction	This work
Sample 2	PbS	2.22 ± 0.12	2.02	180	Non-hot injection reaction	This work
Sample 3	PbS	2.64 ± 0.22	2.39	190	Non-hot injection reaction	This work
Sample 4	PbS	3.09 ± 0.16	2.81	200	Non-hot injection reaction	This work
	PbS	2.24	No Emission	120	Hot-Injection	[15]
	PbS	3.54	No Emission	50	Alcohol Injection	[16]
	PbS	2.43	No Emission	5	Hot-injection	[17]
	PbS	2.07	1.69	25-70	Non-injection	[18]

Table 3.2: Summary of the synthesis conditions and corresponding optical properties.

After synthesis, 10 mL of hexane is added to the solution, and centrifugation was carried out at 8000 rpm for further purification of the CQD. After the first centrifugation step, acetone was added to the solution followed by 10 min of 8000 rpm centrifugation. After drying in a vacuum, the CQDs were finally dispersed in toluene. The as-prepared CQDs by the solid sulphur method are systematically characterized.

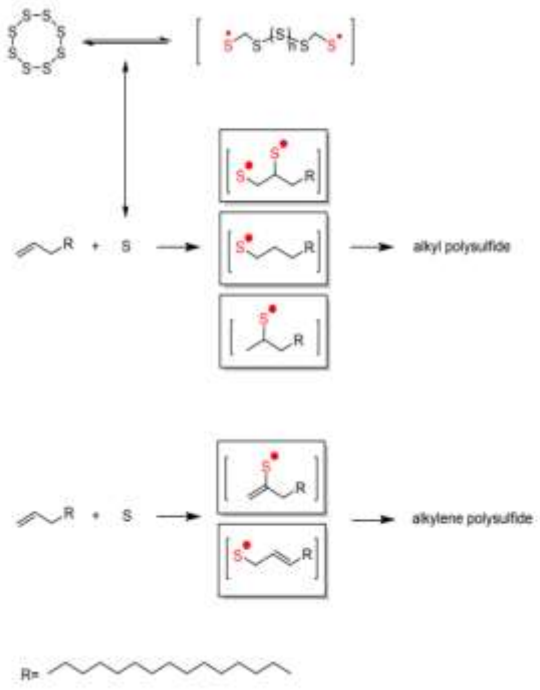

Figure 3.7: Potential schemes for the formation of alkyl or alkylene polysulfide from sulphur powders (reproduced from Ref. 14).

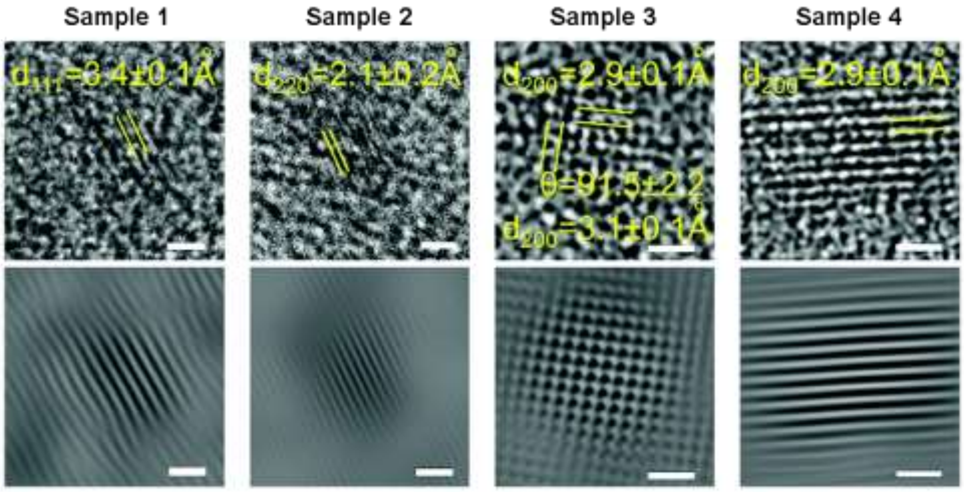

Figure 3.8: TEM images of large band gap CQDs. Scale bars are 1 nm for the HRTEM image (top) and the inverse fast Fourier transform enhanced images (bottom). (TEM images were taken by Dr. Bo Hou).

Figure 3.8 shows the high resolution TEM (HRTEM) images of the as-prepared PbS CQDs. From the HRTEM analysis, clearly resolved lattice fringes corresponding to the {111}, {220}, {200} planes can be seen, which are close to the PbS bulk crystal values (PDF = 78-1057, d_{111} = 3.4 Å, d_{220} = 2.1 Å, d_{200} = 3.0 Å).

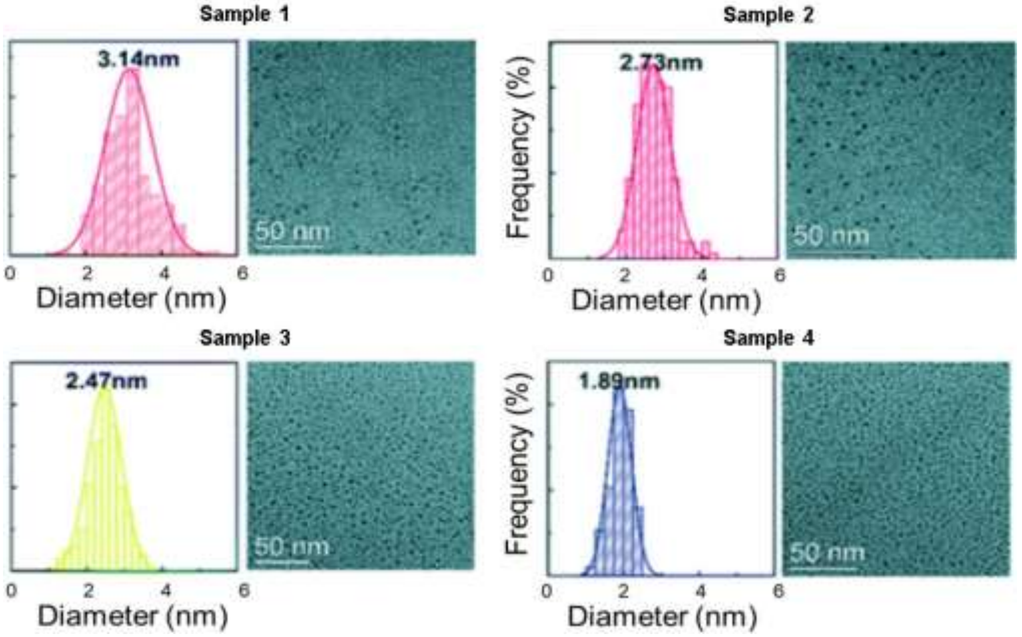

Figure 3.9: TEM images and the size distribution histogram analysis results for each CQDs (TEM images were taken by Dr. Bo Hou).

Figure 3.9 presents the TEM images of the as-prepared QDs, which exhibit a quasi-spherical appearance. The diameters of these QDs are 1.9 ± 0.3 nm (blue), 2.5 ± 0.5 nm (yellow), 2.7 ± 0.4 nm (red) and 3.1 ± 0.1 nm (dark red). The size distributions of the fluorescent PbS QDs are determined from the TEM size statistical analysis.

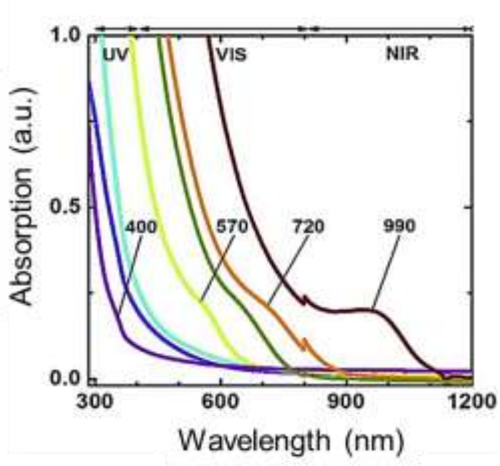

Figure 3.10: Absorption spectra for the different band gap PbS CQDs (the 10 mg ml^{-1} solution in toluene). (UV-Vis image was taken by me with Dr. Bo Hou).

The optical band gaps of the fabricated PbS CQDs were determined from absorption spectroscopy as presented in **Figure 3.10**. These plots show that the absorption edge of the QDs can extend from the ultraviolet (UV) to the near infrared (NIR) of the electromagnetic spectrum.

3.5 Concluding Remarks.

In this work, PbS CQDs with a range of band gaps have been synthesized and characterized. The as-synthesized CQDs have been found to be monodisperse and UV-Vis spectroscopy, TEM, FT-IR spectroscopy, and PL measurements enable the band gaps to be determined precisely. For the first time, large band gap PbS CQDs have been synthesized using a solid sulphur with a non-hot injection method that controls the precursor reactivity and kinetics.

3.6 References

[1] C. B. Murray, D. J. Norris, and M. G. Bawendi, “Synthesis and characterization of nearly monodisperse CdE (E = sulfur, selenium, tellurium) semiconductor nanocrystallites,” J. Am. Chem. Soc., vol. 115, no. 19, p. 8706, 1993.

[2] J. Kim, O. Voznyy, D. Zhitomirsky, and E. Sargent, “25th anniversary article: colloidal quantum dot materials and devices: a quarter-century of advances,” Adv. Mater., vol. 25, no. 36, p. 4986, 2013.

[3] X. Lan, O. Voznyy, P. de Arquer, M. Liu, J. Xu, A. Proppe, G. Walters, F. Fan, H. Tan, M. Liu, Z. Yang, S. Hoogland, and E. Sargent, “10.6% certified colloidal quantum dot solar cells via solvent-polarity-engineered halide passivation,” Nano Lett., vol. 16, no. 7, p. 4630, 2016.

[4] Y. Cao, A. Stavrinadis, T. Lasanta, D. So, and G. Konstantatos, “The role of surface passivation for efficient and photostable PbS quantum dot solar cells,” Nat. Energy, vol. 1, no. 4, p. 16035, 2016.

[5] J. Zhang, J. Gao, C. Church, E. Miller, J. Luther, V. Klimov, and M. Beard, “PbSe quantum dot solar cells with more than 6% efficiency fabricated in ambient atmosphere,” Nano Lett., vol. 14, no. 10, p. 6010, 2014.

[6] Y. Bi, S. Pradhan, S. Gupta, M. Akgul, A. Stavrinadis, and G. Konstantatos, “Infrared solution-processed quantum dot solar cells reaching external quantum efficiency of 80% at 1.35 μm and J_{sc} in excess of 34 mA cm^{-2},” Adv. Mater., vol. 30, no. 7, p. 1704928, 2018.

[7] Y. Cho, P. Giraud, B. Hou, Y. Lee, J. Hong, S. Lee, S. Pak, J. Lee, J. Jang, S. Morris, J. Sohn, S. Cha, and J. Kim, “Charge transport modulation of a flexible quantum dot solar cell using a piezoelectric effect,” Adv. Energy Mater., vol. 8, no. 3, p. 1700809, 2018.

[8] J. Tang and E. Sargent, “Infrared colloidal quantum dots for photovoltaics: fundamentals and recent progress,” Adv. Mater., vol. 23, no. 1, p. 12, 2011.

[9] G. Carey, A. Abdelhady, Z. Ning, S. Thon, O. Bakr, and E. Sargent, “Colloidal quantum dot solar cells,” Chem. Rev., vol. 115, no. 23, p. 12732, 2015.

[10] B. Hou, Y. Cho, B. Kim, J. Hong, J. Park, S. Ahn, J. Sohn, S. Cha, and J. Kim, “Highly monodispersed PbS quantum dots for outstanding cascaded-junction solar cells.,” ACS Energy Lett., vol. 1, no. 4, p. 834, 2016.

[11] W. Feng, C. Qin, Y. Shen, Y. Li, W. Luo, H. An, and Y. Feng, “A layer-nanostructured assembly of PbS quantum dot/multiwalled carbon nanotube for a high-performance photoswitch,” Sci. Rep., vol. 4, no. 1, p. 3777, 2014.

[12] J. Patel, F. Mighri, A. Ajji, and S. Elkoun, “Room temperature synthesis of aminocaproic acid-capped lead sulphide nanoparticles,” Mater. Sci. Appl., vol. 3, no. 2, p. 17264, 2012.

[13] W. Yoon, J. Boercker, M. Lumb, D. Placencia, E. Foos, and J. Tischler, “Enhanced open-circuit voltage of PbS nanocrystal quantum dot solar cells,” Sci. Rep., vol. 3, no. 1, p. 2225, 2013.

[14] B. Hou, Y. Cho, B.-S. Kim, D. Ahn, S. Lee, J. Park, Y.-W. Lee, J. Hong, H. Im, S. Morris, J. Sohn, S. Cha, and J. Kim, “Red green blue emissive lead sulfide quantum

dots: heterogeneous synthesis and applications," J. Mater. Chem. C, vol. 5, no. 15, p. 3692, 2017.

[15] E. Miller, D. Kroupa, J. Zhang, P. Schulz, A. Marshall, A. Kahn, S. Lany, J. Luther, M. Beard, C. Perkins, and J. van de Lagemaat, "Revisiting the valence and conduction band size dependence of PbS quantum dot thin films," ACS Nano, vol. 10, no. 3, p. 3302, 2016.

[16] A. Antanovich, A. Prudnikau, and M. Artemyev, "Formation of ultrasmall PbS nanocrystals in octadecene at mild temperature promoted by alcohol or acetone injection," J. Phys. Chem. C, vol. 118, no. 36, p. 21104, 2014.

[17] A. Shrestha, N. Spooner, S. Qiao, and S. Dai, "Mechanistic insight into the nucleation and growth of oleic acid capped lead sulphide quantum dots," Phys. Chem. Chem. Phys., vol. 18, no. 20, p. 14055, 2016.

[18] T.-Y. Liu, M. Li, J. Ouyang, M. Zaman, R. Wang, X. Wu, C.-S. Yeh, Q. Lin, B. Yang, and K. Yu, "Non-injection and low-temperature approach to colloidal photoluminescent PbS nanocrystals with narrow bandwidth," J. Phys. Chem. C, vol. 113, no. 6, p. 2301, 2009.

Chapter 4. Quantum Dot Surface Functionalization

4.1 Introduction

As shown in Chapter 3, during the hot-injection colloidal synthesis process, long and bulky surface ligands become attached to the surface of metal precursors on CQDs. The long and bulky ligands can either assist or block the nucleation of colloidal quantum dots (CQDs) depending on the reaction temperature and time. However, these long and bulky surface ligands impair the transport of charge when the CQD films are applied in any practical electronics devices. This is because the long interdot-space between neighboring CQDs, which results from the bulky ligands, decreases the probability of electron wave overlapping and inhibits quantum dot charge coupling and transfer (**Figure 4.1**).[1-5] More specifically, the long distance between quantum dots due to the long chain ligands can act as large energy barriers between the band gap of quantum dots (decrease the charge transport). However, with short ligands, the narrow barriers can provide better charge transfer and transport properties. Therefore, in order to realise improvements in quantum dot solar cells (QDSCs), the judicious control of surface passivation is required, and to this end researchers have explored replacing the long-chain aliphatic ligands on the CQDs or CQD films with smaller molecules through a solid-state ligand exchange process.[7-9]

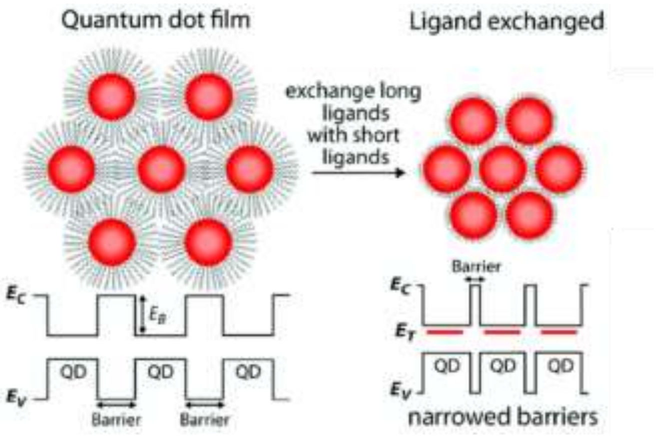

Figure 4.1: The effects of surface treatment on CQD films. (E_c = conduction band, E_v = valence band, and E_T = transport band) (reproduced from Ref. 6).

Figure 4.2: Schematic illustration of a ligand exchange process replacing the long-chain oleic acid (OA) with smaller molecules such as TBAI, EDT, GA, TEG, and Cysteine.

The ligand exchange process is considered to be an important and necessary step in the fabrication of QDSCs and has a significant impact on the resulting QD film properties (**Figure 4.2**). For instance, CQDs that have not undergone a ligand exchange process will still consist of the initial bulky ligands that were introduced during the fabrication process, thereby resulting in low charge mobility and conductivity.[10] Furthermore, failure to accomplish surface passivation of CQD films will lead to a drastic decrease in the photoluminescence quantum yield as well as unwanted fast-carrier recombination, which is believed to result from the generation of surface trap states.[11] Therefore, for QDSC applications, enhancing the carrier transport properties and minimizing the degree of surface trap sites through a successful ligand exchange method are two key issues that have to be resolved.

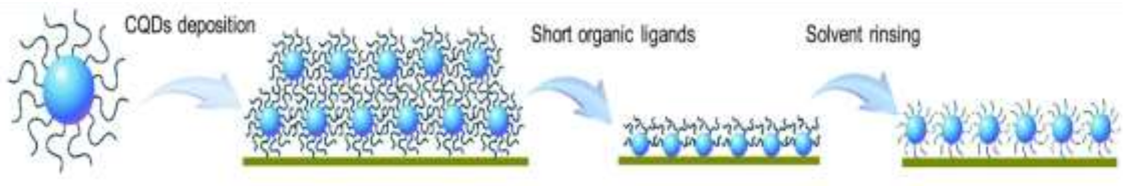

Figure 4.3: Schematic of a solid-state ligand exchange process (reproduced from Ref. 12).

Figure 4.3 shows schematic diagrams of the solid-state ligand exchange process and the fabrication of a CQD film. A neat CQD solution is deposited onto a substrate by spin-coating or spin casting methods. A solution containing short organic and inorganic ligands such as 3-mercaptopropinoic acid (MPA), 1,2-ethaneidthiol (EDT), or tetrabutyl ammonium iodide (TBAI) is then deposited onto the CQD films.[13-16] After sufficient time for the exchange process, a pure ligand solvent is subsequently cast onto the CQD films to wash away the initial longer chain ligands as well as any excess of the new short ligands. In this chapter, we consider how the solid-state ligand exchange method might be optimized as well as the use of new candidate ligands. The aim of this work is to improve the overall performance of QDSCs. Among the many ligand candidates, a ligand exchange method using TBAI appears to show n-type characteristics with the best charge transport properties whereas a ligand exchange method with EDT exhibit p-type characteristics with good hole transport properties.

4.2 CQD Solid-State Ligand Exchange Process

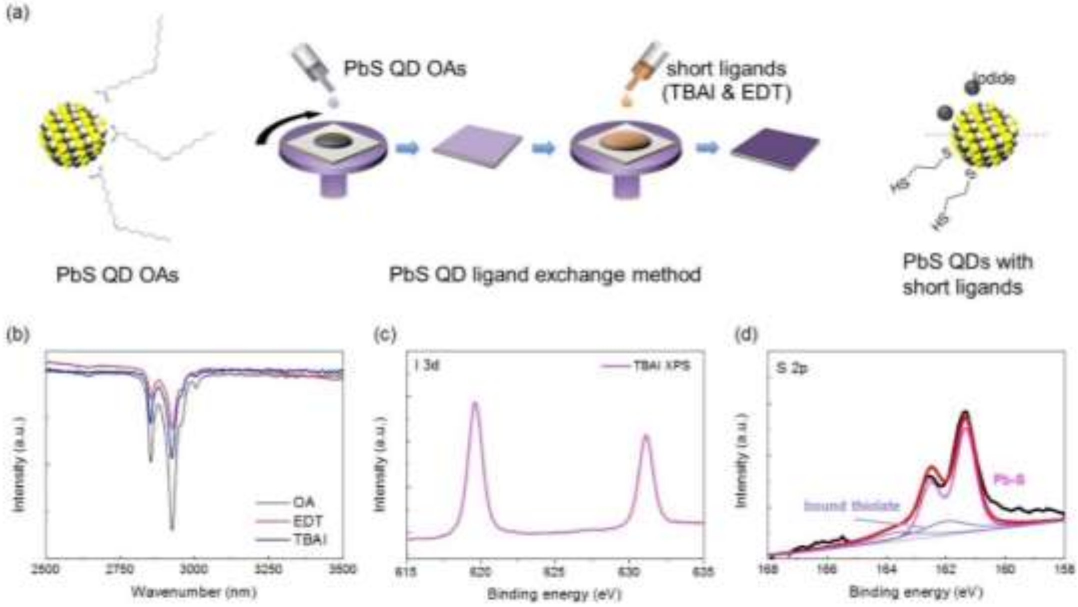

Figure 4.4: (a) Schematic illustrating the PbS quantum dot ligand exchange process. The approach starts with long oleic acid ligands which are then replaced with shorter chain ligands. (b) FT-IR spectroscopy for QDs with OA, EDT, and TBAI ligands, (c) I 3d XPS for TBAI ligand exchange and (d) S 2p XPS for EDT ligand exchange.

As shown in **Figure 4.4**a, a conventional solid-state ligand exchange process which involved replacing oleic acid with either TBAI or EDT ligands was carried out. For the CQD films with TBAI passivation, a drop of the PbS CQD solution was deposited onto spinning substrates at a spin rate of 2500 rpm. 5 drops of the TBAI solution (10 mg ml^{-1} in methanol) was then dropped onto the CQD films and left for 30 seconds before 4 drops of methanol were applied to remove the excess TBAI solution. For the EDT-treated CQD films, the same fabrication method was applied, but in this case a 2 vol% EDT-solution in acetonitrile was used. After the ligand exchange process, it can be clearly observed that the vibrations in the -CH_2 bond disappear after either the TBAI or EDT treatment (**Figure 4.4**b). Moreover, X-ray photoelectron spectroscopy (XPS) was performed to probe the existence of the TBAI and EDT-treated CQD films. **Figure 4.4**c shows the high resolution XPS spectra of I 3d (TBAI treated films). The I 3d doublet is clearly observed at 620.1 eV and at 631.6 eV with a d spin-orbit splitting of 11.5 eV, indicating the existence of iodine molecules on the CQD films. Moreover, as shown in **Figure 4.4**d, the S 2P spectrum can be deconvoluted into two different S oxidation states, one represents the Pb-S state and the other is the thiolate binding state. These XPS results indicate that the long oleic acid ligands have been successfully replaced with shorter (TBAI or EDT) ligands.

4.3 Standard TBAI/EDT QDSC Structure

Figure 4.5 shows a schematic of the energy-band alignment of a QDSC that is based upon an inverted structure: in this case, electrons are collected at the ITO electrode whereas the holes are collected at the Au electrode. The light absorbing layer consists of either TBAI-treated QD layers (12 layers) or a combination of TBAI-treated QD layers (10 layers) & thin EDT-treated QD layers (2 layers), which acts as an electron blocking layer. Throughout Chapter 4, the ligand exchange process has been studied using this standard device configuration.[17]

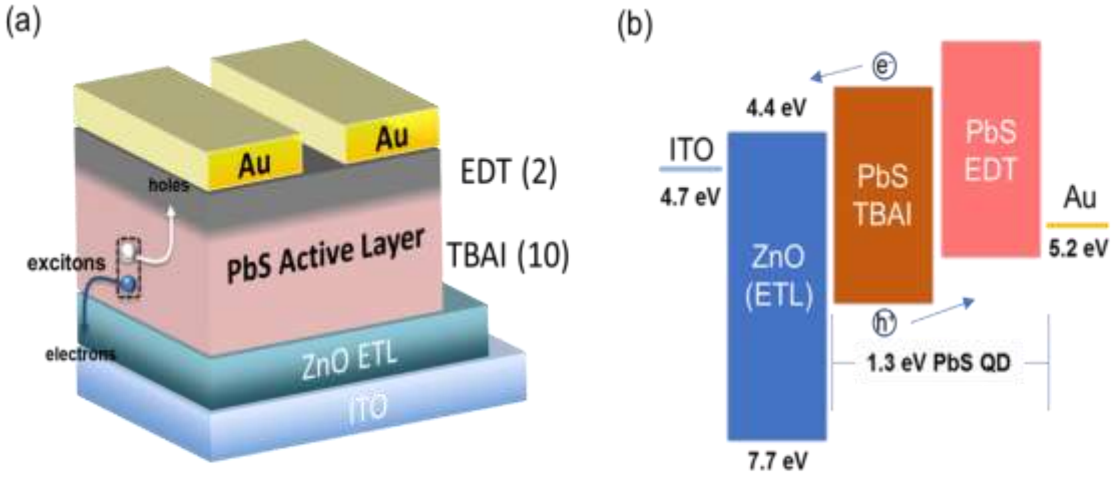

Figure 4.5: (a) A 3D schematic of a QDSC that consists of an ITO electrode, a ZnO ETL, a TBAI-treated QD layer, an EDT-treated QD layer, and an Au electrode. and (b) a schematic of the energy-band alignments.

4.4 Time-Dependent Atomic Ligand Surface Functionalization

For an optimized halide ligand exchange process, the importance of ligand exchange time was investigated for the TBAI-treated PbS CQD films. For the same concentration of TBAI solution, the reaction time of the TBAI solution after casting was controlled, and the performance of the QDSCs with different TBAI ligand exchange times (T_L) was then evaluated (**Figure 4.6**). As shown in **Figure 4.6**, with the short T_L, the surface of CQDs have the OA-rich status, but with the long T_L, the surface of CQDs will show the halide atom rich status.

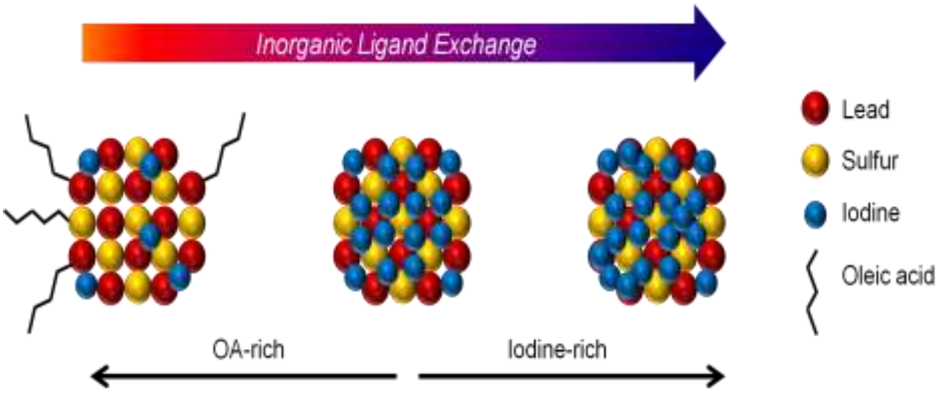

Figure 4.6: Schematics illustrating the TBAI ligand exchange process on a PbS CQD film.

Optimizing the reaction time for the ligand exchange process in CQD films is important for minimizing the amount of oleic acid ligands that remain, which is needed to improve the charge transfer kinetics in the resultant films. To systematically investigate the influence of the ligand exchange time on the resulting performance, the TBAI solution was cast onto the CQD films with the following times (T_L): 15, 30, 60, and 90 sec. After the ligand exchange process, the surface composition of the PbS CQD films was evaluated using FT-IR and XPS. In FT-IR spectroscopy, the presence of the OA on the CQD films can be determined by the identification of four characteristic peaks including vibration peaks at 2920 cm^{-1} (asymmetric C-H), 2850 cm^{-1} (symmetric C-H), 1545 cm^{-1} (asymmetric COO-), and 1403 cm^{-1} (symmetric COO-) (**Figure 4.7**a). The different peaks corresponding to OA were observed to decrease according to the TBAI treatment time (T_L) on the CQD films. Note that a short ligand exchange time (T_L < 30 sec) cannot provide enough replacement of oleic acid with iodine atoms on the surface of the QDs, and considerably large amounts of OAs is found to remain after the treatment. Conversely, a long ligand exchange time is sufficient for the removal of large amounts of the OA. The atomic ratios between Pb atoms and iodine atoms also confirm that, for long T_L, the OA was largely removed, and the surface iodine concentration was found to increase (**Figure 4.7**b-c)

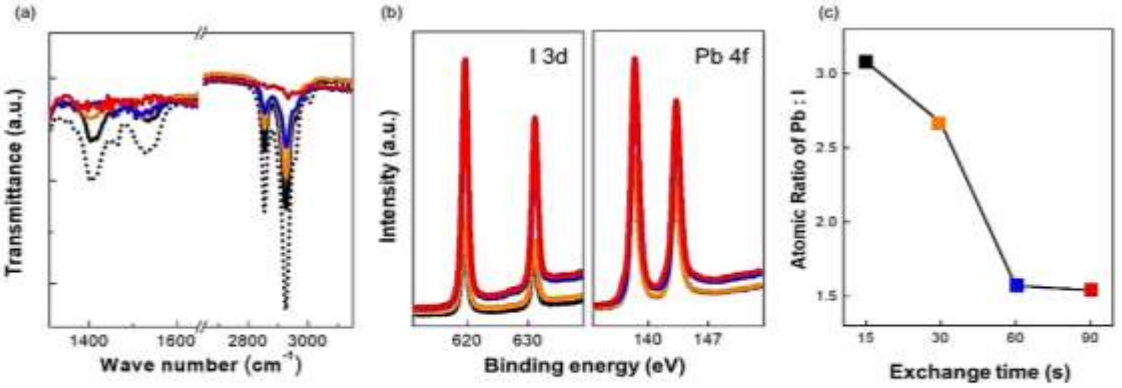

Figure 4.7: (a) FT-IR spectra. The dotted line is for the CQD films with OAs. (b) XPS spectra of the PbS CQD films. (c) Atomic ratios of Pb:I in the PbS CQD films as a function of the reaction time. The color of each curve presents the CQD films with the different TBAI ligand exchange times (T_L): 15 seconds (black), 30 seconds (orange), 60 seconds (blue), and 90 (red) seconds.

Generally, the atomic packing density in a PbS CQD film is a critical factor in determining the resultant photovoltaic performance of a QDSC. This is because the charge carrier transport properties of CQD films are improved when the inter-dot distance between neighboring quantum dots is reduced. **Figure 4.8** shows the packing densities of the bare OA-capped PbS CQD films as well as the TBAI ligand-exchanged PbS CQD films. Compared to the bare OA-capped PbS CQD films, the packing densities increase with the TBAI ligand-exchange time before becoming saturated.

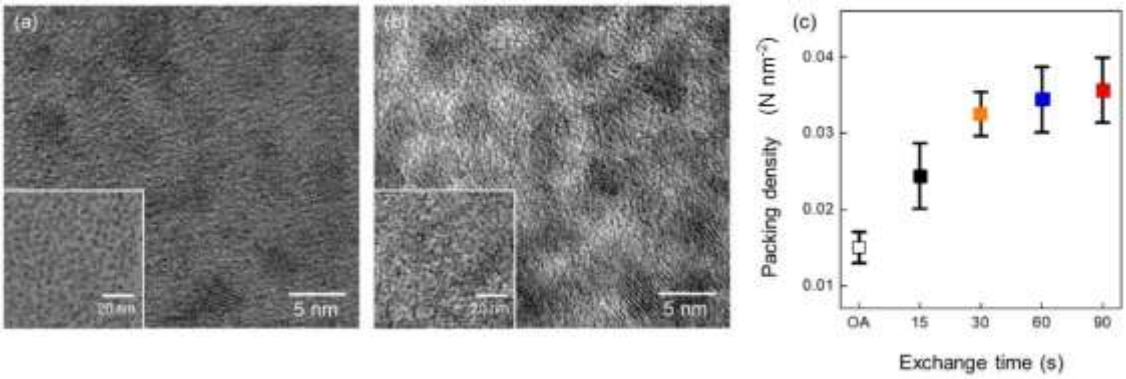

Figure 4.8: TEM images of the CQD films (a) OA surface treatment only and (b) after a fixed ligand exchange time (60 sec). (c) Packing density of the CQD films as a function of the ligand-exchange time (TEM images were taken by Dr. Bo Hou).

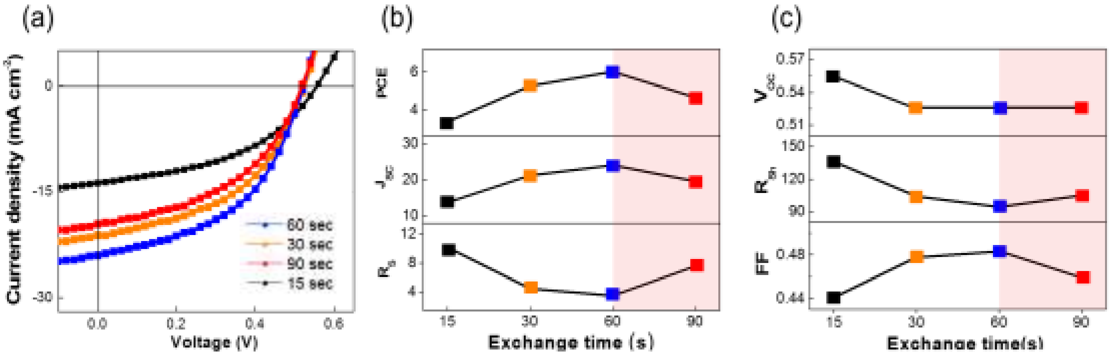

Figure 4.9: (a) J-V curves of the PbS CQD films. (b,c) Solar cell performance parameters of the PbS CQD films. [PCE: power conversion efficiency, J_{sc}: short-circuit current, R_s: series resistance, V_{oc}: open-circuit voltage, R_{sh}: shunt resistance, and FF: fill factor]. The color of each curve presents the CQD films with the different TBAI ligand exchange times (T_L): 15 seconds (black), 30 seconds (orange), 60 seconds (blue), and 90 (red) seconds.

The photocurrent density as a function of voltage (J-V) of the PbS QDSCs for different ligand-exchange times was evaluated. The QDSCs were prepared by applying

10 cycles of spin coating of the TBAI-PbS CQD films onto ZnO/ITO substrates. As shown in **Figure 4.9**a, the PbS CQD films fabricated with a 60 sec-TBAI-treatment time appear to have the greatest solar cell performance with the largest J_{sc}. As shown in **Figure 4.9**b-c, an incomplete removal of the OA after a short ligand exchange time results in a relatively low short-circuit current (J_{sc}) and PCE with a high series resistance (R_s) and shunt resistance. Therefore, QDSCs with a T_L of 60 sec appear to have the highest PCE of 6.62% with an J_{sc} of 24.06 mA cm^{-2}.

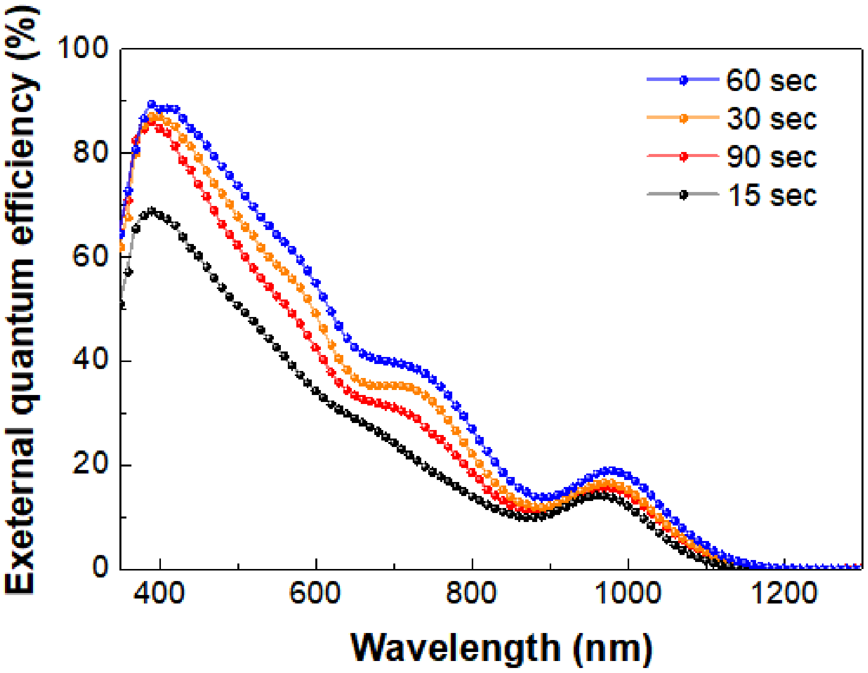

Figure 4.10: External quantum efficiency (EQE) of the PbS QDSCs.

The J_{sc} values obtained from the external quantum efficiency (EQE) measurements also show the same performance trend, which is in good accord with the enhancement in the J_{sc} noted from the J-V curve of the PbS QDSCs (**Figure 4.10**). Increasing the ligand exchange time can alter the packing density of the PbS CQD films as well as the surface coverage. Therefore, at the optimized TBAI-treatment time of 60 sec, the QDSCs show a substantial improvement of 77.58% and 74.98% in the PCE, and J_{sc}, respectively, compared to QDSCs that have been treated with TBAI passivation for 15 seconds. Interestingly, the photovoltaic performance appears to decrease for a longer T_L of 90 seconds despite the high surface coverage of the iodide molecules on the CQD films. It is assumed that the excess iodide molecules (from TBAI molecules) on the CQD films acts as insulators and charge blocking barrier layers in the CQD films.

4.5 Hybrid Ligand Surface Functionalization

With TBAI ligands, the enhanced surface passivation and superior charge transport properties in CQD films have been reported. Nevertheless, not all of the OA ligands (1.3 eV PbS QDs) can be fully removed using the TBAI/methanol ligand solution. Recently, Balazs et. al. reported that the TBAI/methanol solid-state ligand exchange process cannot lead to a complete removal of the surface ligands.[18] Moreover, the work carried out in Bawendi's group reported that a large open-circuit voltage deficit is mainly attributed to the existence of sub-band-gap states, which originate from the bare charged Pb metal atoms, where the iodine molecules cannot attach to the surface of the CQDs after the removal of the OA.[19]

In this work, instead of using single halide molecules, additional pyridine molecules in solution were used in combination to form a hybrid passivation process with the TBAI solution. Pyridine is a small molecule with an amine anchor group. Furthermore, it has already been successfully applied in various CQD optoelectronic devices for the purposes of surface passivation.[20] Its short molecular length can increase the carrier mobility following CQD passivation whereas its alkalinity facilitates a near-complete removal of the initial surfactant (e.g. the oleic acid). In addition, pyridine can create favorable binding with bare charged Pb metal atoms, and eventually decrease any surface defects.[21] By synergistically combining two short ligands (TBAI and pyridine in this case), it is expected that this should lead to a near-complete removal of OA, reducing the formation of sub-ε_{gap} states and the trap states as well as maintaining a high exciton diffusion channel as a result of the halide ion functionalization. For the hybrid (HB, TBAI + pyridine) CQD films, the same fabrication method with the TBAI treatment was used, but during the methanol cleaning steps, a few drops of the pyridine solution (0.5 vol% in acetonitrile) were also applied to the CQD films.

In order to investigate the influence of the hybrid (HB: TBAI + pyridine) ligand passivation process on the structural properties, AFM and TEM analysis of the PbS CQD films were carried out (**Figure 4.11**). **Figure 4.11**a-b show AFM topography images of TBAI-treated and HB-treated CQD films, respectively. The TBAI-treated PbS CQD films show a non-uniform surface consisting of significant cracks and roughness, which is in contrast to the relatively flat and uniform surface of the HB-treated PbS CQD films. The distinct features of the CQD surface can be further evaluated after zooming in on the detailed crystal texture using TEM images. As demonstrated in **Figure 4.11**c-d, the TBAI-treated PbS films show highly fused and aggregated features (see the HRTEM image), which is consistent with the selected area electron diffraction (SAED) patterns shown in the inset where the concentric ring patterns are discontinuous. On the other hand, individual PbS CQDs can be resolved in the HB-treated solid films, which exhibit a high packing density and distinguishable crystal boundaries. Moreover, the continuous concentric ring patterns in the SAED images also indicate that the HB-treated CQD films consist of even and small-sized film grains.

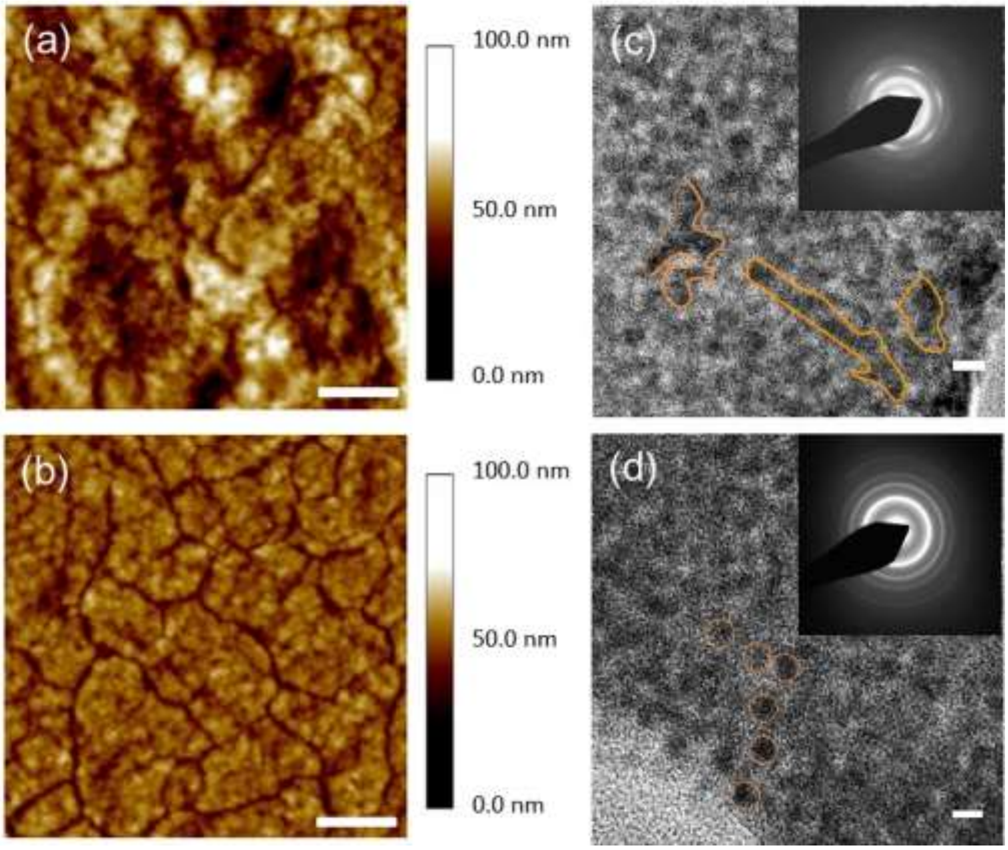

Figure 4.11: AFM images of the PbS quantum dot films with (a) TBAI and (b) Hybrid (HB, TBAI+Pyr) surface passivation. The scale bars are 2μm. HRTEM images of the PbS quantum dot films with (c) TBAI and (d) Hybrid passivation. The scale bars are equal to 5 nm. Insets: SAED patterns of the PbS quantum dot films. (AFM images were taken by Dr. Yuljae Cho and TEM images were taken by Dr. Bo Hou).

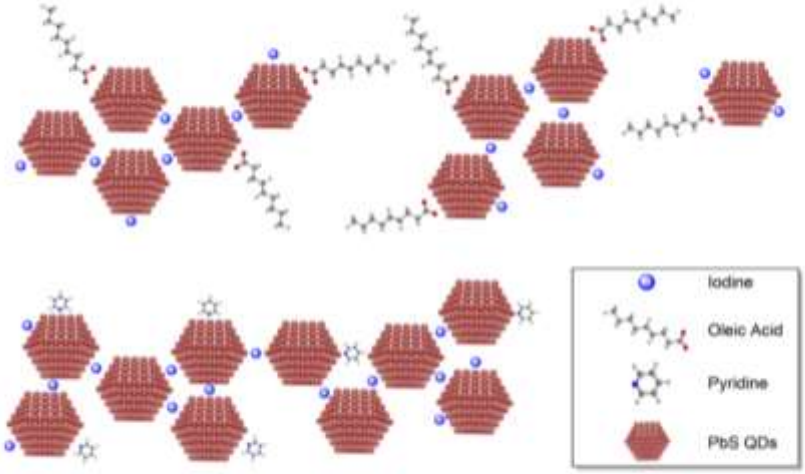

Figure 4.12: Schematics of the CQD films after the hybrid ligand exchange process.

As illustrated in **Figure 4.12**, the HB-treated surface passivation process efficiently controls the CQD films allowing for a decrease in the particle separation, which substantially preserves the quantum confinement effects. It is expected that this noticeable difference in the formation of the CQD films may have a big influence on the electrical and photovoltaic properties.

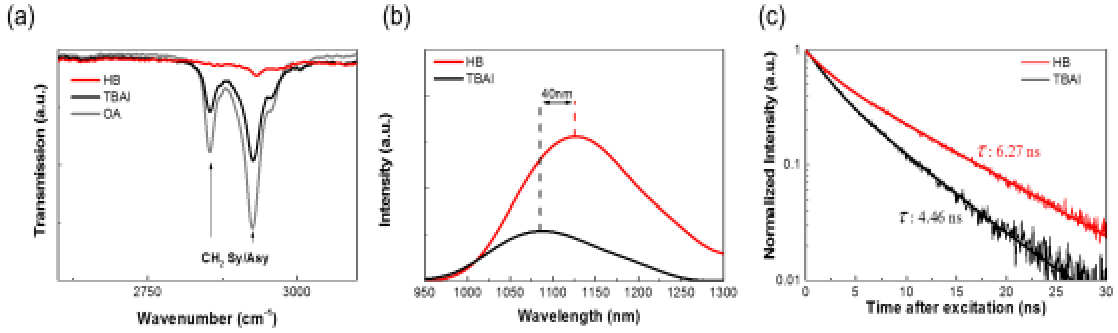

Figure 4.13: (a) FT-IR spectra of the pristine CQD film (with oleic acid, shown in grey), TBAI-treated (black line) and HB-treated (red line) ligand-exchanged films. (b) Stationary photoluminescence of the HB (red line) and TBAI-passivated (black line) PbS CQD films with identical thickness. (c) Time-resolved photoluminescence of HB (red line) and TBAI-passivated (black line) PbS CQD films. (PL spectra were taken by Dr. Jong Chul Lim).

The HB and TBAI-passivated PbS CQD films were investigated by studying the FT-IR spectra (**Figure 4.13**). The as-prepared PbS CQDs with oleic acid show two dominant peaks in the FT-IR spectra, which correspond to the symmetric vibration (2854 cm^{-1}) and asymmetric stretching (2924 cm^{-1}) of the $-CH_2$ bonds of the oleic acids (**Figure 4.13**a). The absence of these two distinct peaks implies the complete removal of the oleic acid from the CQD surface. It can be clearly observed that the $-CH_2$ stretching vibrations almost completely disappear after the HB passivation process, although they still can be seen in the TBAI-treated films.

To further probe the fundamental optical properties, both the steady-state and time-resolved photoluminescence (TR-PL) properties were studied. In **Figure 4.13**b, for the same thickness conditions, the PL intensity of the HB-treated films was found to be higher than that of the TBAI-only treated films, which indicates an increase in the radiative recombination and a reduction in the surface trap sites. Moreover, there is a redshift in the exciton peak of the PL spectra between the HB and TBAI-treated films, which suggests an enhancement in the quantum coupling due to a reduction in the inter-particle(dot) spacing. Moreover, the HB-treated CQD films display a much longer PL decay as seen in the TR-PL measurement shown in **Figure 4.13**c. A prolonged exciton lifetime is an indicator that the faster, non-radiative recombination channels have been suppressed and there is little influence from deep trap sites. The increased PL intensity and PL lifetime strongly indicate that the HB-passivation treatment results in a significant reduction in the number of surface trap sites and the corresponding non-radiative recombination within the CQD films. These results support the claim that the pyridine and TBAI hybrid ligand treatment provides a better passivation compared to that of the films treated with only the TBAI ligand exchange process.

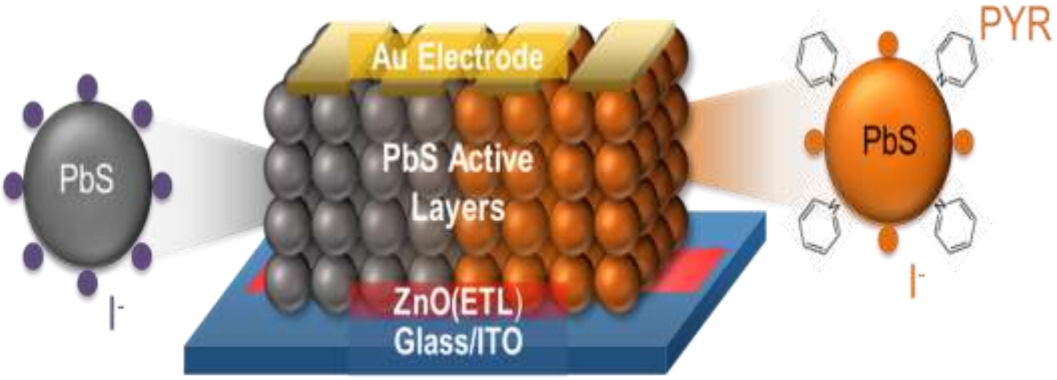

Figure 4.14: Illustration of the assembly of PbS QDSCs using a layer-by-layer deposition process.

Figure 4.14 shows an illustration of the fabricated QDSCs with the TBAI and HB surface passivation process. Typically, ZnO nanoparticle films are used to act as the electron-accepting layer, which was spin-coated on to the indium tin oxide/glass (ITO/glass) substrate. Subsequently, CQD films and the corresponding ligand exchange treatment with the TBAI and HB ligands were then deposited onto the ZnO films. In this case, the CQD films act as the layers responsible for generating the charge.

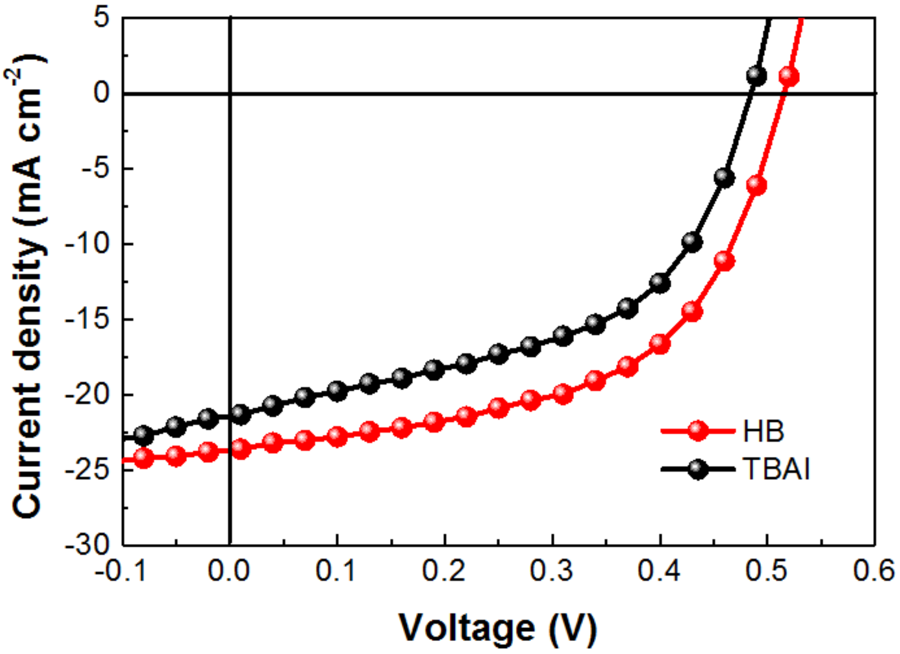

Figure 4.15: Current density-voltage (J-V) characteristics for the HB-treated PbS film (red line) and the TBAI-treated PbS film (black line) devices.

Figure 4.15 shows the J-V characteristics under AM1.5G illumination conditions. The overall PCE performance is much improved with the HB-treatment than that of the TBAI-treated films. The device consisting of 10 TBAI-PBS CQD layers shows an open circuit voltage (V_{oc}) of 0.485V, a short circuit current J_{sc} of 21.36 mA cm^{-2}, a fill factor (FF) of 0.51 and a power conversion efficiency (PCE) of 5.3 %. However, by adding the extra pyridine treatment step, it appears to noticeably increase V_{oc}, J_{sc} and FF resulting in an overall increase in the power conversion efficiency to 6.8 %. After applying pyridine onto the CQD surface, the remaining oleic acid ligands are effectively removed, resulting in a well-ordered CQD film with better surface alignment properties. Furthermore, due to the decrease in the inter-dot spacing, there is then an increase in the probability that the wavefunctions of the charge carriers will overlap.

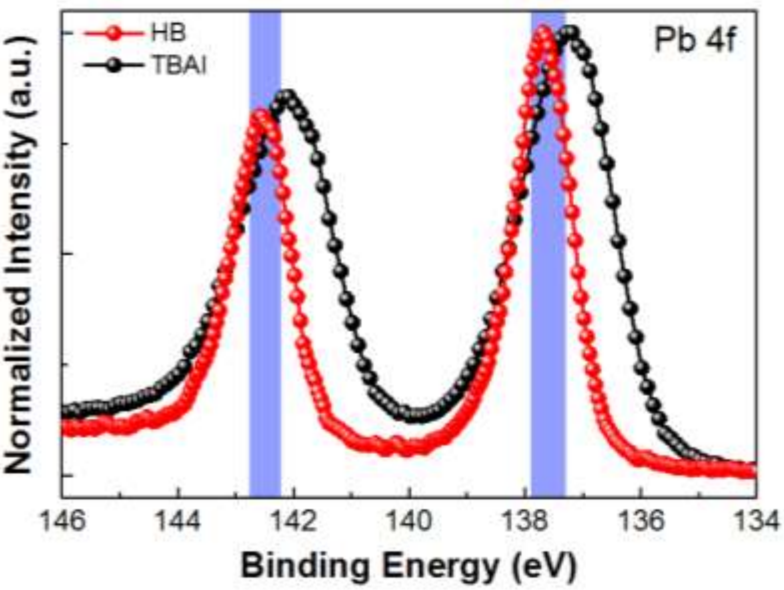

Figure 4.16: XPS spectra of Pb 4f in CQD films of TBAI and HB passivation.

XPS was performed to probe the bare charged Pb metal states on the surface of the CQDs for both the HB and TBAI-treated films (**Figure 4.16**). The Pb 4f peaks probed following the HB-passivation process have a higher binding energy and smaller FWHM values than that observed for the TBAI surface passivation films. Moreover, the XPS peak positions for the HB-passivation film are much closer to the expected Pb-S bond feature whereas films with only the TBAI passivation appear to be much closer to that of metallic Pb. This suggests that the HB treatment process plays a key role in maintaining the Pb-S bond state, which prevents the generation of surface traps and exposed charged Pb atoms.

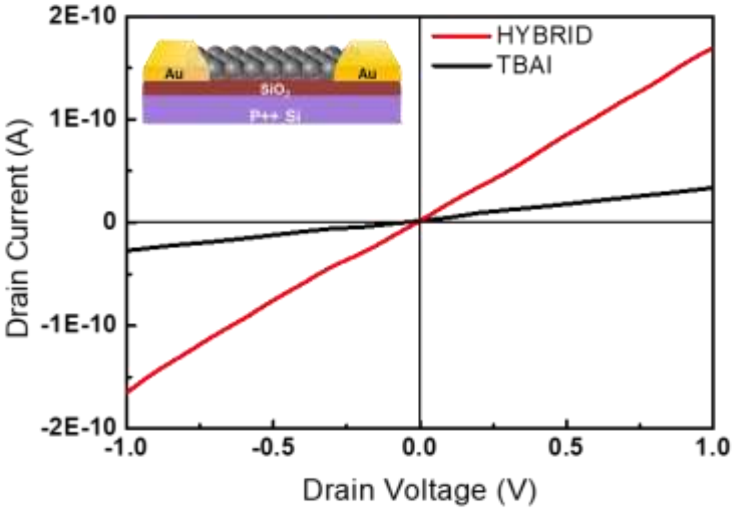

Figure 4.17: Conductance J-V curves of the HB and TBAI-treated films deposited onto an Au-patterned SiO_2 device. Inset: Illustration of the SiO_2 devices.

Figure 4.17 shows the J-V curves for an electrical conductance measurement on the TBAI and HB CQD films. The CQD devices were fabricated using a PbS solution and ligand exchange process by standard photolithography. Photoresist (MICROPOSIT S1813) was spin-coated on a silicon wafer with a 300 nm SiO_2 layer and baked at 110 °C for 60 sec. The substrate was exposed through a photomask that defines the electrode pattern and then developed in MICROPOSIT MF-319 developer for 30 sec and finally the silicon substrate was then rinsed with water for 2 min. A metal electrode of 100 nm Au was deposited by thermal evaporation. PbS solutions and the same ligand exchange process for TBAI and HB passivation were deposited onto the substrate using a layer-by-layer spin coating method. The J-V curve for the HB surface passivation film is steeper than that recorded for the TBAI-based film, which indicates that an electrically favorable environment is formed.

4.6 Concluding Remarks

In this chapter, we have explored the influence of a time-dependent inorganic ligand exchange process as well as an organic/inorganic hybrid passivation process on the resulting properties of PbS CQD films. It is shown that controlled surface passivation increases the better packing density through a minimization of the residual oleic acid ligands. Moreover, the additional use of the shortest amine base (pyridine) can result in a near-complete removal of the oleic acid and can reduce the number of surface trap sites in CQD films. Consequently, high performance CQD solar cell devices have been successfully fabricated by employing different surface passivation methods. These approaches can be used to help better understand the energy harvesting dynamics and the charge carrier transfer dynamics of CQD films.

4.7 References

[1] W. H. Evers, J. M. Schins, M. Aerts, A. Kulkarni, P. Capiod, M. Berthe, B. Grandidier, C. Delerue, H. S. van der Zant, C. van Overbeek, J. L. Peters, D. Vanmaekelbergh, and L. D. Siebbeles, “High charge mobility in two-dimensional percolative networks of PbSe quantum dots connected by atomic bonds.,” Nat. Comm., vol. 6, no. 1, p. 8195, 2015.

[2] L. Sun, J. Choi, D. Stachnik, A. Bartnik, B.-R. Hyun, G. Malliaras, T. Hanrath, and F. Wise, “Bright infrared quantum-dot light-emitting diodes through inter-dot spacing control,” Nat. Nanotech., vol. 7, no. 6, p. 369, 2012.

[3] D. Milliron, “Quantum dot solar cells: the surface plays a core role,” Nat. Mater., vol. 13, no. 8, p. 772, 2014.

[4] A. Fischer, L. Rollny, J. Pan, G. Carey, S. Thon, S. Hoogland, O. Voznyy, D. Zhitomirsky, J. Kim, O. Bakr, and E. Sargent, “Directly deposited quantum dot solids using a colloidally stable nanoparticle ink,” Adv. Mater., vol. 25, no. 40, p. 5742, 2013.

[5] F. Xu, L. Gerlein, X. Ma, C. Haughn, M. Doty, and S. Cloutier, “Impact of different surface ligands on the optical properties of PbS quantum dot solids,” Mater., vol. 8, no. 4, p. 1858, 2015.

[6] Y. Liu, M. Gibbs, C. Perkins, J. Tolentino, M. Zarghami, J. Bustamante, and M. Law, “Robust, functional nanocrystal solids by infilling with atomic layer deposition,” Nano Lett., vol. 11, no. 12, p. 5349, 2011.

[7] M. Zarghami, Y. Liu, M. Gibbs, E. Gebremichael, C. Webster, and M. Law, "P-type PbSe and PbS quantum dot solids prepared with short-chain acids and diacids.," ACS Nano, vol. 4, no. 4, p. 2475, 2010.

[8] W. Baumgardner, K. Whitham, and T. Hanrath, "Confined-but-connected quantum solids via controlled ligand displacement," Nano Lett., vol. 13, no. 7, p. 3225, 2013.

[9] G. Carey, L. Levina, R. Comin, O. Voznyy, and E. H. Sargent, "Record charge carrier diffusion length in colloidal quantum dot solids via mutual dot-to-dot surface passivation.," Adv. Mater., vol. 27, no. 21, p. 3325, 2015.

[10] E. Klem, H. Shukla, S. Hinds, D. MacNeil, L. Levina, and E. Sargent, "Impact of dithiol treatment and air annealing on the conductivity, mobility, and hole density in PbS colloidal quantum dot solids," Appl. Phys. Lett., vol. 92, no. 21, p. 212105, 2008.

[11] C. Giansante, and I. Infante, "Surface traps in colloidal quantum dots: a combined experimental and theoretical perspective.," J. Phys. Chem. Lett., vol. 8, no. 20, p. 5209, 2017.

[12] R. Wang, Y. Shang, P. Kanjanaboos, W. Zhou, Z. Ning, and E. Sargent, "Colloidal quantum dot ligand engineering for high performance solar cells," Energy Environ. Sci., vol. 9, no. 4, p. 1130, 2016.

[13] C. Reinhart and E. Johansson, "Colloidally prepared 3-mercaptopropionic acid capped lead sulfide quantum dots," Chem. Mater., vol. 27, no. 21, p. 7313, 2015.

[14] D. Neo, C. Cheng, S. Stranks, S. Fairclough, J. Kim, A. Kirkland, J. Smith, H. Snaith, H. Assender, and A. Watt, "Influence of shell thickness and surface passivation on

PbS/CdS core/shell colloidal quantum dot solar cells," Chem. Mater., vol. 26, no. 13, p. 4004, 2014.

[15] Z. Jin, A. Wang, Q. Zhou, Y. Wang, and J. Wang, "Detecting trap states in planar PbS colloidal quantum dot solar cells," Sci. Rep., vol. 6, no. 1, p. 37106, 2016.

[16] Y. Cho, B. Hou, J. Lim, S. Lee, S. Pak, J. Hong, P. Giraud, A.-R. Jang, Y.-W. Lee, J. Lee, J. Jang, H. Snaith, S. Morris, J. Sohn, S. Cha, and J. Kim, "Balancing charge carrier transport in a quantum dot P-N junction toward hysteresis-free high-performance solar cells.," ACS Energy Lett., vol. 3, no. 4, p. 1036, 2018.

[17] C.-H. Chuang, P. Brown, V. Bulović, and M. Bawendi, "Improved performance and stability in quantum dot solar cells through band alignment engineering," Nat. Mater., vol. 13, no. 8, p. 796, 2014.

[18] D. Balazs, D. Dirin, H.-H. Fang, L. Protesescu, G. ten Brink, B. Kooi, M. Kovalenko, and M. Loi, "Counterion-mediated ligand exchange for PbS colloidal quantum dot superlattices," ACS Nano, vol. 9, no. 12, p. 11951, 2015.

[19] G. Hwang, D. Kim, J. Cordero, M. Wilson, C. Chuang, J. Grossman, and M. Bawendi, "Identifying and eliminating emissive sub-bandgap states in thin films of PbS nanocrystals," Adv. Mater., vol. 27, no. 30, p. 4481, 2015.

[20] M. Law, J. Luther, Q. Song, B. Hughes, C. Perkins, and A. Nozik, "Structural, optical, and electrical properties of PbSe nanocrystal solids treated thermally or with simple amines," J. Am. Chem. Soc., vol. 130, no. 18, p. 5974, 2008.

[21] N. Noel, A. Abate, S. Stranks, E. Parrott, V. Burlakov, A. Goriely, and H. Snaith, "Enhanced photoluminescence and solar cell performance via Lewis base passivation

of organic–inorganic lead halide perovskites," ACS Nano, vol. 8, no. 10, p. 9815, 2014.

Chapter 5. Solar Cell with Plasmonic Nanoparticles

5.1 Introduction

The previous chapter showed how, through surface functionalization of QDs using short chain ligands, it was possible to overcome the conventional limits on the performance of QDSCs. To further improve the QDSC performance, the insertion of various interfacial layers with nanostructured materials has been considered.[1-6] Increasing the thickness of the CQD films may also be an important factor in harvesting a larger number of photons. However, the thickness of the CQD films cannot be easily adjusted and is limited to a certain value (usually 200-300 nm for the PbS QDSCs) due to their low hole transport properties.[7]

Plasmonic effects have been proposed as a solution to overcoming the limited light absorption in thin-film solar cell devices, and various types of plasmonic solar cells have been explored. Specifically, introducing plasmonic nanostructures (usually in the form of metallic nanoparticles (MNPs)) into photovoltaic solar cells is an alternative approach to improving the overall light absorption efficiency while keeping the thickness of the CQD film unaltered.[8-11] Surface plasmons are collective oscillations of free electrons in metallic and plasmonic materials between a metal and its surrounding medium. These surface plasmons can induce plasmonic effects, and plasmonic enhancement is achieved through various mechanisms such as far-field scattering and near-field enhancement.

As an example, small metallic nanoparticles can be used as scattering elements to trap freely propagating plane waves from the Sun by folding the light into the CQD films. This far-field scattering increases the absorption efficiency by increasing the optical path length of the incident photons in the absorbing medium. Moreover, metallic nanoparticles can be used as near-field antennas in which the near-field wave increases the number of absorption events compared to their bare counterparts (**Figure 5.1**). Introducing these two plasmonic effects in QDSCs can also increase the overall energy conversion efficiency.

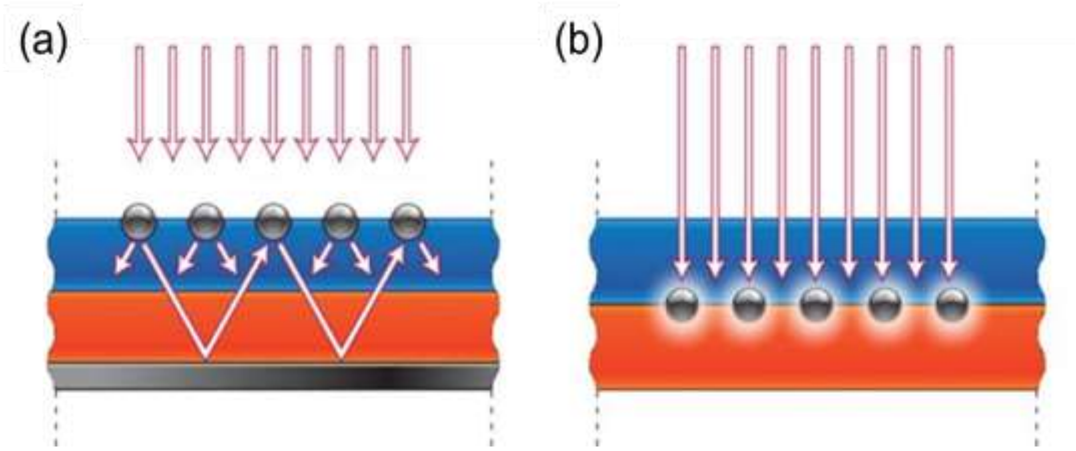

Figure 5.1: Illustrations of (a) the effects of scattering and (b) the near-field wave resonance via the introduction of small metallic nanoparticles (reproduced from Ref. 12).

5.2 Plasmonic Effect Layers

Small Au and Ag metal nanoparticles (MNPs) are typically the best candidates for plasmonic resonance effects in photovoltaic cells. Plasmonic phenomena can promote increased optical absorption by concentrating the near-field intensity of the electromagnetic waves and increasing the light travel time through scattering. In this work, large-sized silver (Ag) nanoparticles (> 50 nm) are used for the purposes of light scattering, whereas small-sized gold (Au) nanostructures (< 20 nm) can induce strong near-field oscillations. Combining these two plasmonic effects in QDSCs can synergistically improve the light absorption efficiency. Furthermore, the placement of these Au and Ag MNPs is also of critical importance for the maximized enhancement of the overall device performance because the direct combination between the nanostructures and the photovoltaic active films can, unintentionally, induce undesirable quenching of excitons and lead to fast carrier recombination.[13-14] Therefore, efficiently utilizing both plasmonic effects in the correct locations of the device is necessary to improve the QDSC performance. In this work, the aim is to not only incorporate two different plasmonic nanostructures (i.e. Au and Ag nanoparticles) within a QDSC, but also to position these at the appropriate locations within the device so that both effects can be exploited leading to enhanced energy conversion. Two different nanoparticles are applied (i.e. dual-plasmon layers) via a simple nanoparticle solution deposition process (**Figure 5.2**). The Ag MNPs are included to induce scattering whereas the Au MNPs are employed to act as antennas in the QDSC applications.

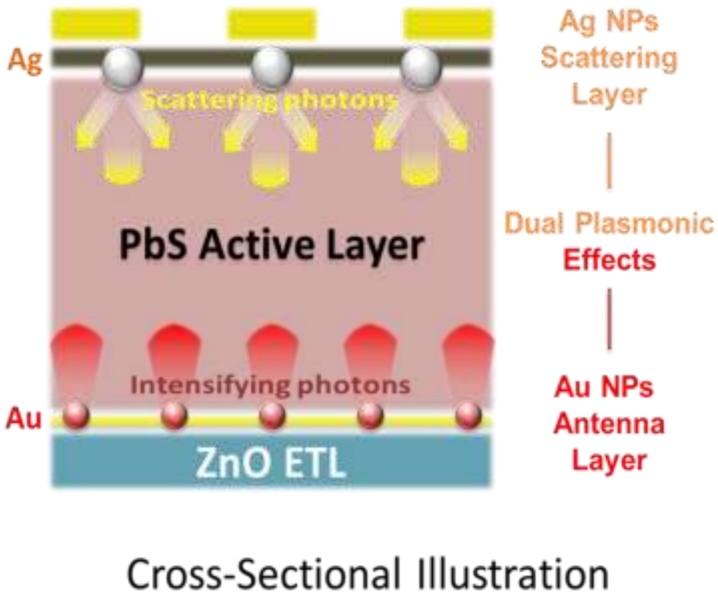

Figure 5.2: Schematic of the cross-sectional QDSC with the dual-plasmonic layers.

To verify the influence of plasmonic effects on the QDSC, the Au and Ag nanoparticles are inserted at the top and bottom of the interface layers in the QDSC junction structure, respectively. For the fabrication process, ZnO nanoparticles (which act as the electron transfer layer) were deposited on indium tin oxide (ITO)/glass substrates using a spin-coating method. On the as-prepared ZnO/ITO substrates, the Au nanoparticle (~ 10 nm) solution was then spin-coated to form the first plasmonic layer. Subsequently, the PbS CQD films were spin-coated onto the Au layers which serve as the photovoltaic active layers. In the PbS active layers, tetrabutylammonium iodide (TBAI) and 1,2-ethanedithiol (EDT) ligand-treated PbS QD films were used (hybrid passivation). After the 12 layers of PbS CQD films (10 TBAI-treated CQD layers and 2 EDT-treated CQD layers), the Ag nanoparticle solution was then spin-coated onto the device. **Figure 5.3** shows transmission electron microscopy images of the silica-coated Au and Ag nanoparticles.

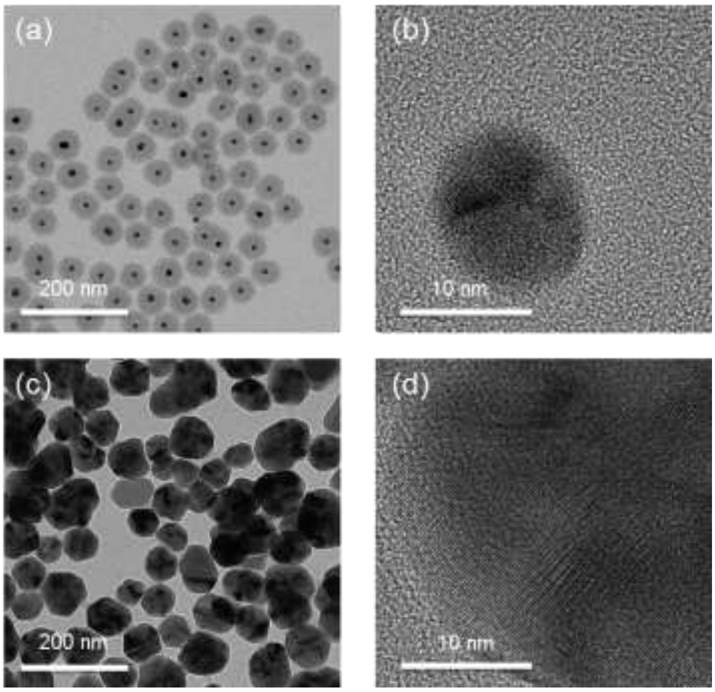

Figure 5.3: TEM images of the (a,b) silica-coated Au NPs and (c, d) Ag NPs. (TEM images were taken by Dr. Bo Hou)

The enhancement in the optical absorption as a result of the nanoparticles has been investigated using UV-Vis spectroscopy (**Figure 5.4**). The CQD films prepared for the UV-Vis absorption analysis have the same thickness (5 layers). As shown, there is no observable shift in the absorption peak after the deposition of the Au and Ag nanoparticles on the CQD films, indicating that the addition of the nanoparticles does not change the optical properties of the film. Interestingly, the Au nanoparticles applied on to the CQD film were found to selectively increase the absorption spectra over the wavelength range from 450 – 800 nm, but near the absorption edge (900 – 1200 nm) the absorption spectra of the CQD film exhibits no significant change for the different concentrations of Au nanoparticles, indicating that there is no spectral response of the nanoparticles. In contrast, applying Ag nanoparticles to the film was found to increase the absorption spectra of the

CQD films over the full spectral range (450 – 1200 nm), which is in accordance with a scattering-based phenomenon that is observed for the Ag nanoparticles.

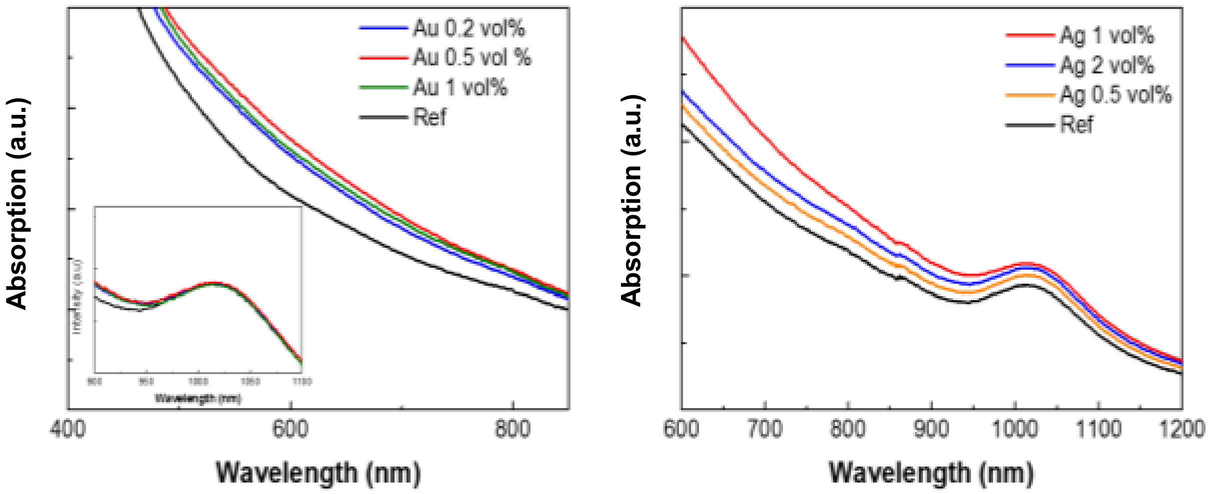

Figure 5.4: Ultraviolet–visible images of the PbS CQD films (the 100 nm films) with the (a) Au NPs in DI water and (b) Ag NPs in ethanol.

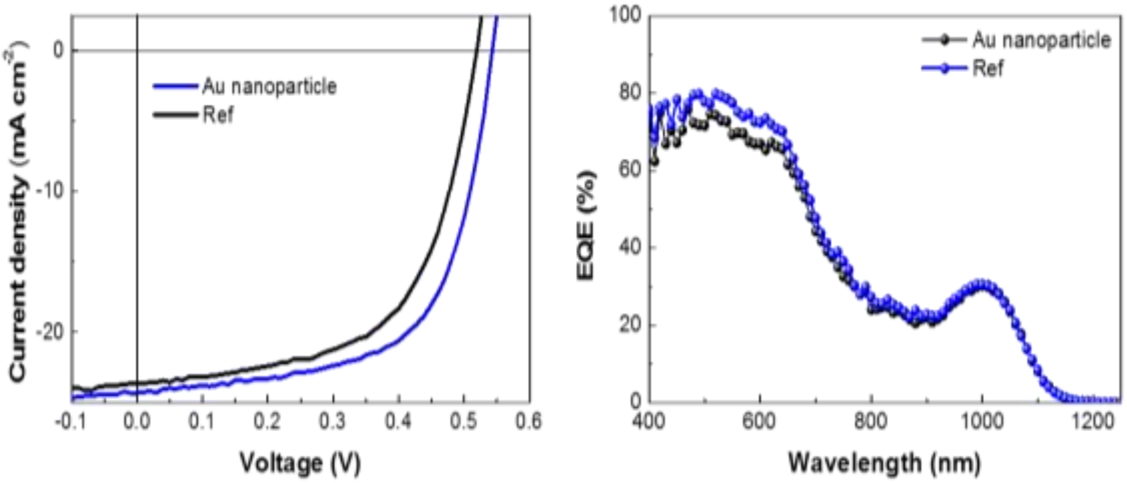

Figure 5.5: J-V and EQE curves of the QDSCs with the inserted Au layers only.

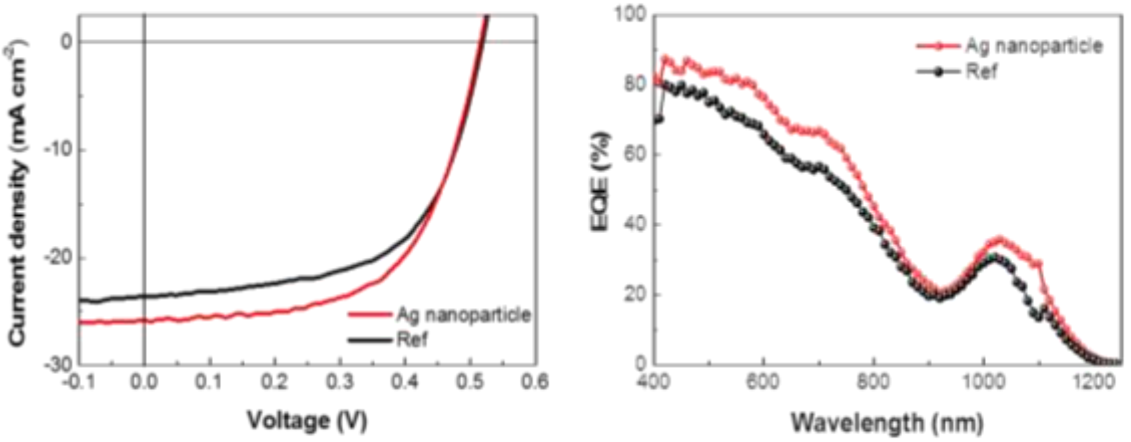

Figure 5.6: J-V and EQE curves of the QDSCs with the inserted Ag layers only.

Photocurrent density and voltage (J-V) curves were evaluated under standard AM 1.5G solar illumination (100 mW cm^{-2}). **Figure 5.5** shows the representative J-V curves for the reference (without Au and Ag nanoparticles) and Au plasmonic QDSCs (Au-QDSCs). The Au plasmonic nanoparticles in the QDSCs lead to a substantial improvement in the PCE from 7.22% to 8.32%. This significant enhancement in the PCE largely relates to the improvements in the short-circuit current (J_{sc}), fill factor (FF) and open-circuit voltage (V_{oc}). Similarly, the application of Ag nanoparticles also leads to a substantial improvement in the PCE, reaching 8.12% (**Figure 5.6**). In this case, the large PCE enhancement observed with the use of Ag nanoparticles results mainly from the improvement in the J_{sc}. The slight V_{oc} increase could also be associated with the inserted Au NPs and their plasmonic coupling effects with the CQD films, promoting electron transfer and increasing the built-in potential of the QDSC. Moreover, the Ag nanoparticles can trap the incident light and increase the effective photon path length.

External quantum efficiency (EQE) of the QDSCs was measured to determine the origin of the performance enhancement. After applying the Au nanoparticles, regions of the EQE spectra are selectively increased. The major increase in the EQE spectra occurs over the wavelength region of 400 nm – 700 nm. However, for the region near 900 – 1200 nm, there is no significant spectral difference between the reference cell and the Au-QDSC, which is in good agreement with the results obtained from UV-Vis spectroscopy. The EQE spectra for the Ag-based plasmonic QDSCs (Ag-QDSCs) exhibits an increase in the area compared with that of the reference QDSC, indicating a larger J_{sc} value for the Ag-QDSC. The enhancement in the EQE occurs over the full wavelength range of the incident photons on the CQD film through a scattering effect.

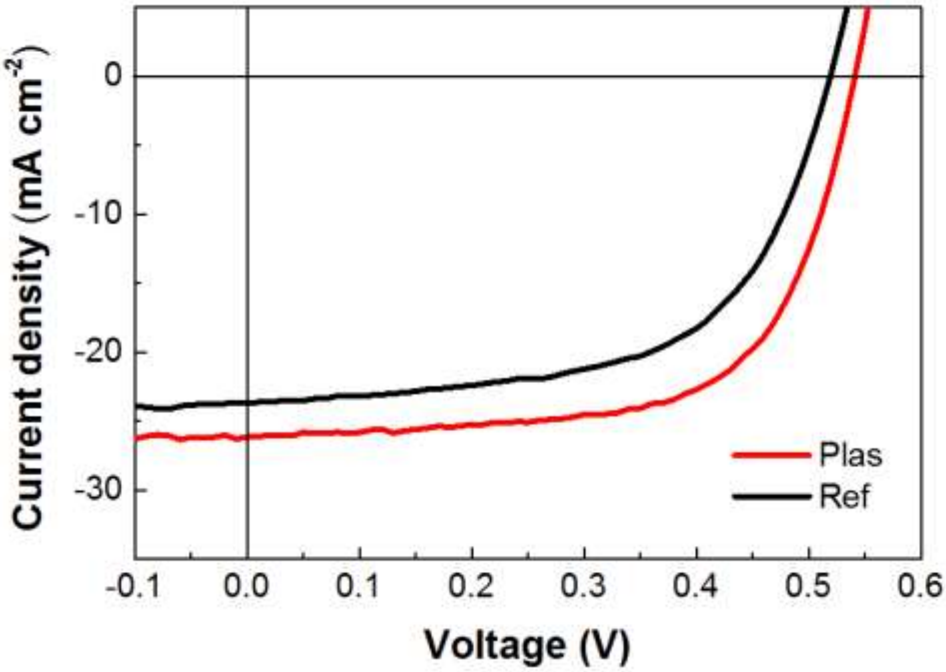

Figure 5.7: J-V curves of the QDSCs with the dual-plasmonic (Ag and Au nanoparticles) layers.

In the final experiment in this study, both types of nanoparticles (Au and Ag) were applied to the solar cell to form dual-plasmonic layers so as to maximize both the antenna and scattering effects. From these results, it is found that champion QDSCs consisting of dual Au and Ag nanoparticle layers exhibits a V_{oc} = 0.54 V, J_{sc} = 26.16 mA cm^{-2}, FF = 0.65 and PCE = 9.18 % (**Figure 5.7**). The increase in the V_{oc} and FF are strongly related to the antenna effects of the Au nanoparticles while the relatively large increase in the J_{sc} correlates with both plasmonic effects through an increase in the number of charge carriers due to the high photon absorption efficiency. QDSCs with dual-plasmonic layers show a 13% increase in the J_{sc}, a 4% increase in the V_{oc}, a 7% increase in FF, and finally a 25% enhancement in the PCE compared to the reference cell.

5.3 Concluding Remarks

In this chapter, the introduction of Au and Ag nanoparticles on a CQD film can effectively increase the overall photon absorption efficiency of the film, leading to an improvement in the device performance. The synergistic application of nanostructured materials in CQD films is a promising technique for producing highly efficient CQD photovoltaic devices for a range of optoelectronic applications such as solar cells.

5.4 References

[1] L. Etgar, T. Moehl, S. Gabriel, S. Hickey, A. Eychmüller, and M. Grätzel, “Light energy conversion by mesoscopic PbS quantum dots/TiO_2 heterojunction solar cells,” ACS Nano, vol. 6, no. 4, p. 3092, 2012.

[2] C. Ding, Y. Zhang, F. Liu, Y. Kitabatake, S. Hayase, T. Toyoda, R. Wang, K. Yoshino, T. Minemoto, and Q. Shen, “Understanding charge transfer and recombination by interface engineering for improving the efficiency of PbS quantum dot solar cells,” Nanoscale Horiz., vol. 3, no. 1, p. 417, 2018.

[3] J. Jean, S. Chang, P. Brown, J. Cheng, P. Rekemeyer, M. Bawendi, S. Gradečak, and V. Bulović, “ZnO nanowire arrays for enhanced photocurrent in PbS quantum dot solar cells,” Adv. Mater., vol. 25, no. 20, p. 2790, 2013.

[4] J. Heo, M. Jang, M. Lee, D. Shin, D. Kim, S. Moon, S.-W. Kim, B. Park, and S. Im, “High performance solid-state PbS quantum dot-sensitized solar cells prepared by introduction of hybrid perovskite inter-layer,” ACS Appl. Mater. Interfaces, vol. 9, no. 47, p. 41104, 2017.

[5] C. Chen, L. Wang, L. Gao, D. Nam, D. Li, K. Li, Y. Zhao, C. Ge, H. Cheong, H. Liu, H. Song, and J. Tang, “6.5% certified Sb_2Se_3 solar cells using PbS colloidal quantum dot film as hole transporting layer,” ACS Energy Lett., vol. 2, no. 9, p. 2125, 2017.

[6] G.-H. Kim, P. de Arquer, Y. Yoon, X. Lan, M. Liu, O. Voznyy, L. Jagadamma, A. Abbas, Z. Yang, F. Fan, A. Ip, P. Kanjanaboos, S. Hoogland, J. Kim, and E. Sargent,

"High-efficiency colloidal quantum dot photovoltaics via robust self-assembled monolayers," Nano Lett., vol. 15, no. 11, p. 7691, 2015.

[7] P. Rekemeyer, C.-H. Chuang, M. Bawendi, and S. Gradecak, "Minority carrier transport in lead sulfide quantum dot photovoltaics," Nano Lett., vol. 17, no. 10, p. 6221, 2017.

[8] T. Kawawaki, H. Wang, T. Kubo, K. Saito, J. Nakazaki, H. Segawa, and T. Tatsuma, "Efficiency enhancement of PbS quantum dot/ZnO nanowire bulk-heterojunction solar cells by plasmonic silver nanocubes," ACS Nano, vol. 9, no. 4, p. 4165, 2015.

[9] S. Chen, Y. Wang, Q. Liu, G. Shi, Z. Liu, K. Lu, L. Han, X. Ling, H. Zhang, S. Cheng, and W. Ma, "Broadband enhancement of PbS quantum dot solar cells by the synergistic effect of plasmonic gold nanobipyramids and nanospheres," Adv. Energy Mater., vol. 8, no. 8, p. 1701194, 2018.

[10] T. Kawawaki and T. Tatsuma, "Enhancement of PbS quantum dot-sensitized photocurrents using plasmonic gold nanoparticles," Phys. Chem. Chem. Phys., vol. 15, no. 46, p. 20247, 2013.

[11] S. Baek, J. Song, W. Choi, H. Song, S. Jeong, and J. Lee, "A resonance-shifting hybrid n-type layer for boosting near-infrared response in highly efficient colloidal quantum dots solar cells," Adv. Mater., vol. 27, no. 48, p. 8102, 2015.

[12] H. Atwater and A. Polman, "Plasmonics for improved photovoltaic devices," Nat. Mater., vol. 9, no. 3, p. 205, 2010.

[13] B. Gonfa, M. Kim, P. Zheng, S. Cushing, Q. Qiao, N. Wu, M. Khakani, and D. Ma, “Investigation of the plasmonic effect in air-processed PbS/CdS core–shell quantum dot based solar cells,” J. Mater. Chem. A, vol. 4, no. 34, p. 13071, 2016.

[14] F. Beck, A. Stavrinadis, S. Diedenhofen, T. Lasanta, and G. Konstantatos, “Surface plasmon polariton couplers for light trapping in thin-film absorbers and their application to colloidal quantum dot optoelectronics,” ACS Photonics, vol. 1, no. 11, p. 1197, 2014.

Chapter 6. Nanostructured Electrodes for Energy Storage

6.1 Introduction

In the previous chapters, the various sizes of 0-dimension nanostructures (CQDs) and engineering techniques for QDSCs have been proposed. Simultaneously, to efficiently store the intermittent generation of electricity from QDSCs, the development of high-performance supercapacitor electrodes is also strongly required. To obtain a good energy storing performance, there are two different parameters that need to be considered: one is the electrode material selection, and the other relates to the engineering of nanostructures.

For the material selection of pseudocapacitors, currently, transition metal oxides/hydroxides such as RuO_2, $Ni(OH)_2$, Co_3O_4 and MnO_2, are the most commonly used electrode materials with high theoretical capacitances.[1-6] However, their low conductivity and structural instability continuously hinders their successful exploitation as electrode materials. To overcome these limitations, numerous studies have focused on the development of new electrode materials that are based on binary transition metal oxides (BTMOs, $ZnCo_2O_4$, $NiCo_2O_4$, $NiMoO_4$ and etc.) or metal chalcogenides (Ni_3S_2, Cu_2S and etc.).[7-14] These materials typically exhibit a higher electrical conductivity and richer chemical valence states than the single-component transition metal oxides/hydroxides. These materials have been selected as potential electrode candidates in this chapter.

For the engineering of nanostructures, various nanostructuring approaches have been developed to address issues related to limited electrochemical kinetics on the surface of electrodes, which are strongly associated with the low degree of surface contact area and low ion diffusion rates through the miniaturization of the size as well as the construction of a porous-structure. Despite these notable technological advances, it remains a challenge to tailor complex BTMOs and metal sulphides into desirable nanostructured architectures with a large surface area, facile and short ion diffusion paths, and a high structural integrity during the charge/discharge process. Therefore, the development of new methods with solution-based synthesis processes are strongly required to successfully tailor the nanostructures and to understand the new charge storage mechanism in pseudocapacitors. This is because solution-based synthesis approaches such as hydrothermal synthesis have been proposed and generally accepted as an efficient fabrication procedure for preparing electrodes with a unique morphology and hierarchical architecture.

In this chapter, the aim is to develop novel and facile synthetic routes for the preparation of unique nanostructured binary metal oxides and metal chalcogenides that can enhance the charge storage kinetics so as to improve the overall storage capacitance and storage performance.

6.2 Nanostructured Electrode Control

6.2.1 Aspect ratio control

1-D nanostructures are one of the most widely used architectures for electrochemical storage devices mainly because 1) the unique geometry results in a large contact surface area; 2) the structures exhibit short diffusion distances; 3) they exhibit good structural stability and 4) they possess a favorable charge carrier path during the charge/discharge processes. Controlling the supersaturated environments enables the synthesis of 1-D nanostructures with different, but predictable, morphologies (**Figure 6.1**). In this regard, a simple and facile way for controlling the supersaturation levels has been proposed so as to control the crystal nucleation rates and the crystal growth geometries thereby leading to different 1-D $NiMoO_4$ aspect ratios. The primary interest in $NiMoO_4$ lies in the fact that the high specific capacitance from the Ni atom and the high electrical conductivity from the Mo atom can contribute collectively to the superior electrochemical behavior.

In this work, one-dimensional $NiMoO_4$ nanostructures with different aspect ratios on nickel foams were synthesized using a hydrothermal method. First, a conductive Ni foam (1 cm x 1 cm) was cleaned using 1 M HCl, ethanol, and deionized water. For a typical synthesis, 1.0 mmol of $Ni(NO_3)_2 \cdot 6H_2O$ and 1.0 mmol of Na_2MoO_4 were dissolved in deionized water at room temperature to form a clear green solution. After being stirred for an hour, the solution was then transferred to a 45 ml Teflon-lined cup, and then the Ni foam was transferred into a Teflon-lined cup and a stainless-steel autoclave. Different nanostructures of the $NiMoO_4$ material were synthesized using various solvents with different mixtures of solvents such as water, ethanol and hydrochloric acids.

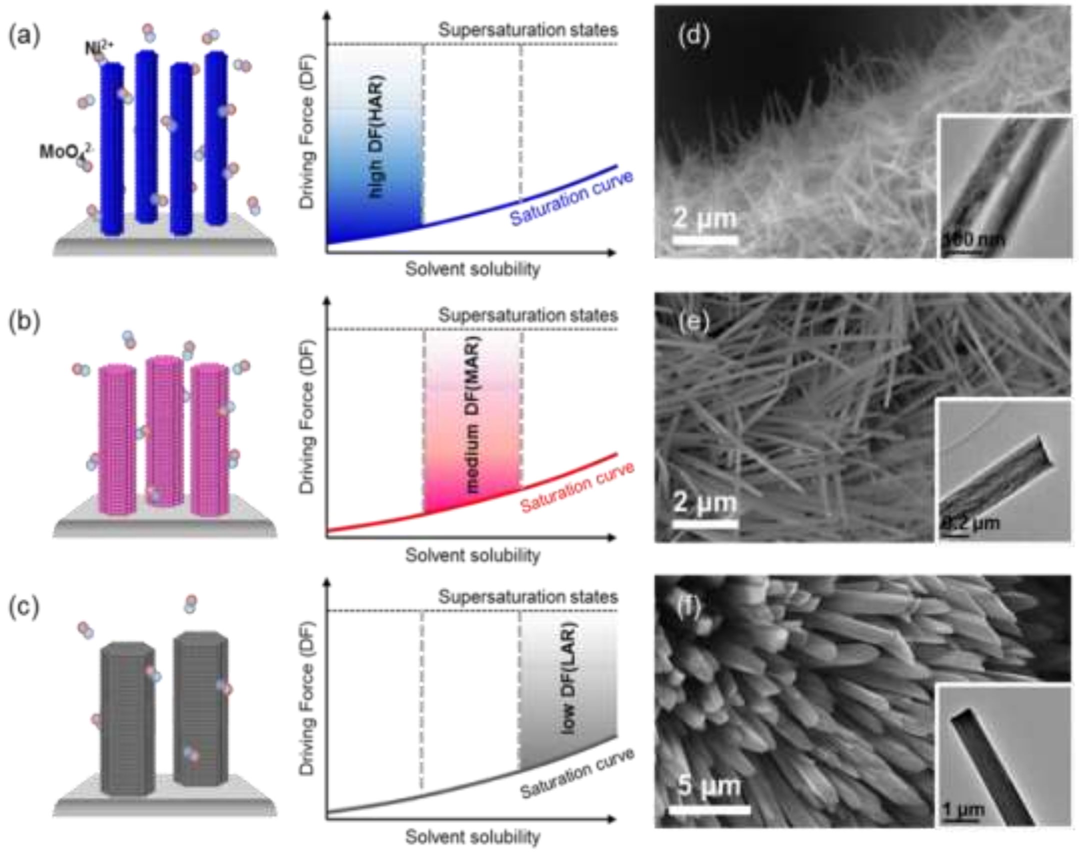

Figure 6.1: Illustration of (a) high aspect ratio (HAR-), (b) medium aspect ratio (MAR-) and (c) low aspect ratio (LAR-) $NiMoO_4$ 1-D nanostructures. 1-D nanostructures are systematically controlled by using different supersaturation states during the growth phase. (d-f) SEM images of the HAR-, MAR- and LAR-$NiMoO_4$ 1-D nanostructures. Inset images show the corresponding TEM images of the three different 1-D nanostructures. (TEM images were taken by Dr. Bo Hou).

The morphology and structural characteristics of the as-prepared $NiMoO_4$ materials were investigated by scanning electron microscopy (SEM). The controlled growth of the 1-D $NiMoO_4$ nanostructures with different aspect ratios was successfully achieved by adjusting the solubility level in the reaction solution thereby introducing different supersaturation states for the precursor solvents (Water, Ethanol and HCl-water). It can be seen that by varying the supersaturation state, the morphology of the 1-D nanostructures can be transformed from a low length-to-breadth aspect ratio (LAR) to a high aspect ratio (HAR) (medium aspect ratio (MAR) structures can also be formed using this process).

The results in **Figure 6.1**e show that the MAR-$NiMoO_4$ sample obtained from the DI water-only solution has a diameter size of ~250 nm. In contrast, the HAR-$NiMoO_4$ sample (**Figure 6.1**d) with a diameter of about 80 nm is grown under low solubility conditions induced by adding an alkaline solvent. The LAR-$NiMoO_4$ sample (**Figure 6.1**f) has a diameter of 800 nm and was constructed by introducing an additional acidic solvent. These findings indicate that introducing a low (high) solubility environment to the hydrothermal precursor solution induces a relatively high (low) degree of supersaturation, leading to a higher (lower) driving force for the crystal nucleation and growth process. As a result, a higher driving force leads to a faster growth rate along the length of the nanostructure than the radial direction and hence results in the formation of 1-D $NiMoO_4$ structures with a high aspect ratio. Therefore, the synthesis mechanism responsible for the different 1-D $NiMoO_4$ structures can be understood in terms of a control of the solvent solubility.

The nanostructures for the HAR-, MAR- and LAR-$NiMoO_4$ samples were further characterized by transmission electron microscopy (TEM). The TEM images (shown in the insets in **Figure 6.1**) clearly demonstrate that the diameter of the 1-D nanostructures for the as-prepared $NiMoO_4$ samples is in good agreement with the SEM results.

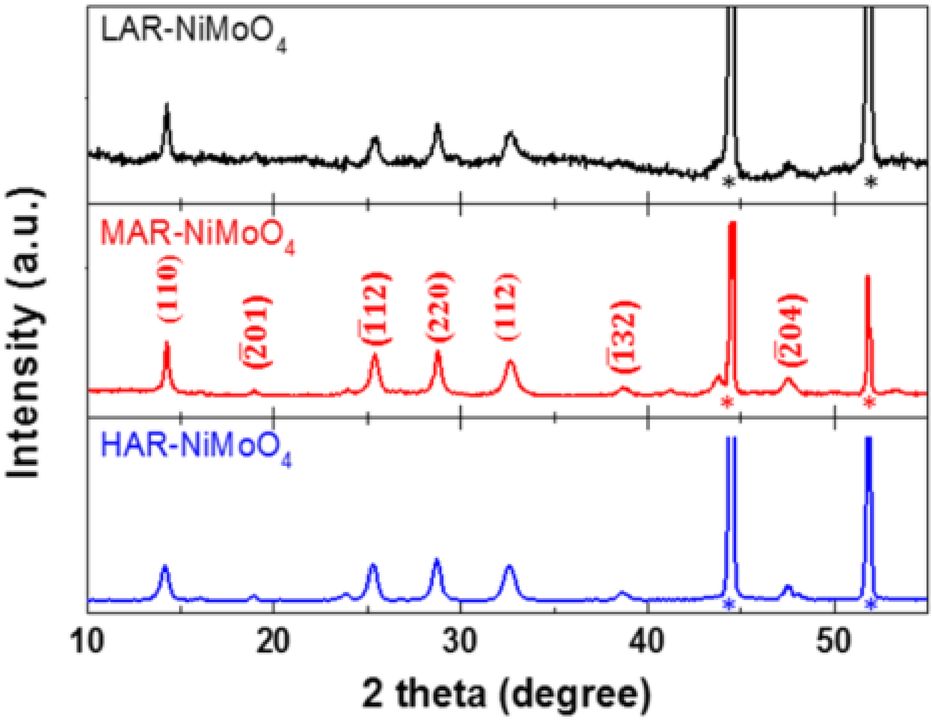

Figure 6.2: XRD patterns of the as-prepared NiMoO$_4$ nanostructures for the three different growth processes.

To evaluate the crystallographic phase of the NiMoO$_4$ electrode samples, X-ray diffraction (XRD) spectra were analyzed, which are shown in **Figure 6.2**. The diffraction patterns obtained from the 1-D NiMoO$_4$ nanostructures with different aspect ratios are unambiguously assigned to the NiMoO$_4$ phase (JCPDS Card No. 86-0361) without any noticeable differences (**Figure 6.2**).[15]

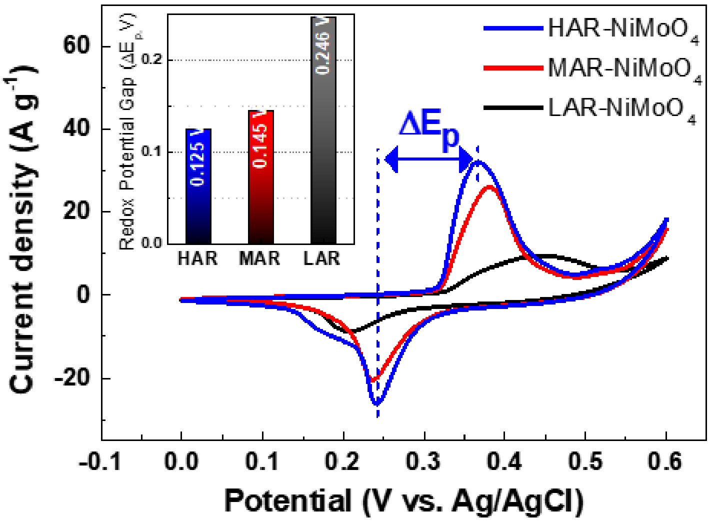

Figure 6.3: CV curves for the HAR-, MAR-, and LAR-$NiMoO_4$ electrodes at a scan rate of 5 mV s^{-1} in 1.0 M KOH. The inset shows the redox potential gap (ΔE_p).

The HAR-, MAR- and LAR-$NiMoO_4$ materials were applied directly as working electrodes in a three-electrode system. **Figure 6.3** presents the cyclic voltammetry (CV) curves of the three different types of $NiMoO_4$ electrodes at a scan rate of 5 mV s^{-1}. It can be clearly observed that all of the $NiMoO_4$ electrodes exhibit several Faradaic reaction peaks that can be ascribed to reversible redox reactions between Ni(II) and Ni(III).[16] The area bounded by the CV curve for the HAR-$NiMoO_4$ sample occupies the largest area, indicating the highest value for the electrochemical capacitance. The inset of **Figure 6.3** indicates the potential difference (ΔE_p) for each electrode between the anodic and cathodic peak, representing the degree of reversible intercalation and de-intercalation dynamics during the CV charge-discharge process. The results indicate that the HAR-$NiMoO_4$ electrode provides much more appreciable OH^- ion access and a faster charge transfer rate.

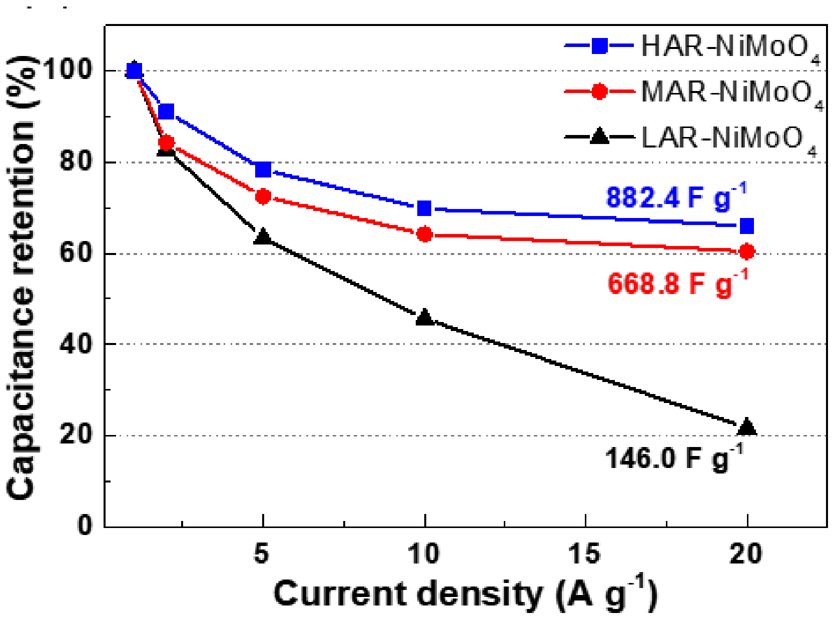

Figure 6.4: Comparison of the capacitance retention of the HAR-, MAR-, and LAR-NiMoO4 samples.

The calculated specific capacitance for the HAR-, MAR-, and LAR-NiMoO4 samples at a current density of 1 A g^{-1} are found to be 1335 F g^{-1}, 1106 F g^{-1} and 672 F g^{-1}, respectively (**Figure 6.4**). From a low current density of 1 A g^{-1} to a high current density of 20 A g^{-1}, the capacitance of the HAR-NiMoO4 electrode shows good capacitance retention, which is found to be 882.4 F g^{-1} at 20 A g^{-1} with ~ 66.1% of the capacitance retained when compared to that measured for 1 A g^{-1}. On the other hand, for the MAR and LAR-NiMoO4 electrodes the capacitance is recorded to be 668.8 F g^{-1} and 146.0 F g^{-1} with 60.5% and 21.8% rate retention, respectively. The HAR-NiMoO4 shows the highest specific capacitance and rate retention values.

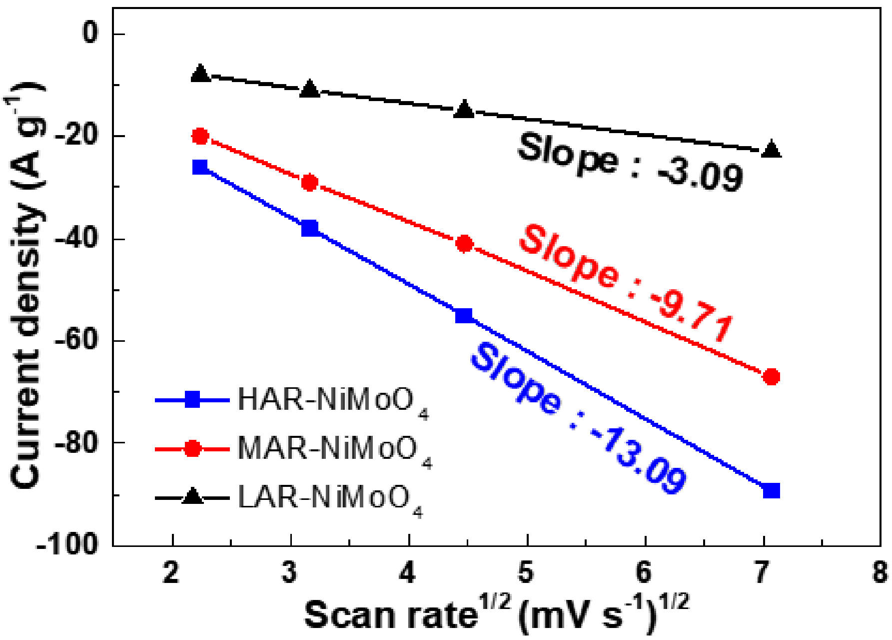

Figure 6.5: Cathodic peak current density as a function of the square root of the scan rate for the 1-D $NiMoO_4$ samples.

The cathodic peak current densities of the $NiMoO_4$ electrodes are plotted as a function of the square root of the scan rates in **Figure 6.5**. The cathodic peak current increases linearly, showing that redox reactions at the surface are followed by a diffusion-controlled process with the OH^- ions. Also, it is evident that the cathodic peak current of the HAR-$NiMoO_4$ sample shows a steeper dependence compared to the other electrodes, indicating a larger diffusion coefficient. The diffusion coefficient for the $NiMoO_4$ electrodes were calculated according to the following Randles–Sevcik equation:[17]

$$i_p = (2.69 * 10^5) * n^{\frac{3}{2}} * A * D_0^{\left(\frac{1}{2}\right)} * C_0 * v^{\frac{1}{2}} \qquad [6.1]$$

where i_p is the cathodic peak current density, n is the number of electrons, A is the electrode backbone area, D_0 is the diffusion coefficient, C_0 is the electrolyte concentration, and v is the scan rate. Therefore, the diffusion coefficient for the 1-D $NiMoO_4$ samples can be directly compared from the slope of the curve $(D_0^{\frac{1}{2}} \propto i_p/\upsilon^{\frac{1}{2}})$. As a result, the diffusion coefficient of the HAR-$NiMoO_4$ sample is found to be 1.82 and 17.9 times larger than that of the MAR- and LAR-$NiMoO_4$ samples, respectively.

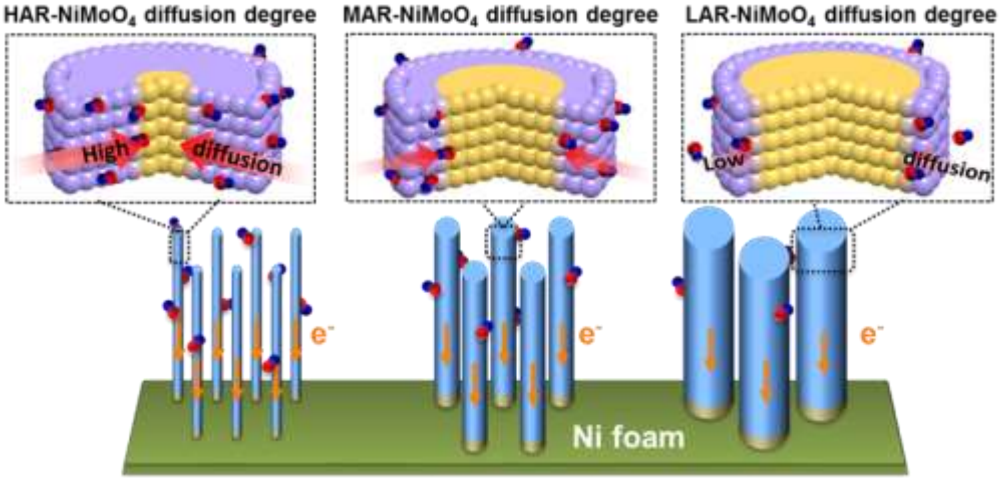

Figure 6.6: Illustration of the relationship between the tailored 1-D $NiMoO_4$ nanostructures and the pseudo-capacitive behavior including electrolyte ion diffusion and electron transfer dynamics (blue dots : hydroxide ions and red dots: oxide ions).

Overall, the electrochemical relationships for the $NiMoO_4$ electrodes with different 1-D morphologies are illustrated in **Figure 6.6**. The HAR-$NiMoO_4$ electrode nanostructure not only provides the largest contact sites, which lead to a large density of electrolyte ions near the surface, but also facilitates more efficient electrochemical reactions through the large degree of ion diffusion towards the inside of the electrode. Such behavior is strongly correlated with high capacitance, fast retention rate and charge transfer mechanism of the HAR-$NiMoO_4$ electrode.

6.2.2 Core-shell structure control

Usually core–shell nanostructures offer a new active interface and a potential synergistic effect between the core and shell structures, making these structures highly attractive in many applications. In this regard, hierarchically-assembled 3D porous heterostructures consisting of binary transition metal oxides (BTMO) were also studied. The heterostructures comprise a rigidly interconnected nanoporous core-shell network and a secondary protruding nanostructure as illustrated in **Figure 6.7**. Hierarchically assembled 3D $ZnCo_2O_4/NiMoO_4$ heterostructures on a Ni foam were synthesized using a two-step hydrothermal synthetic process. For the synthesis of the $ZnCo_2O_4$ core backbone material, 1.0 mmol of $Zn(NO_3)_2 \cdot 6H_2O$, 2.0 mmol of $Co(NO_3)_2 \cdot 6H_2O$ and 5.0 mmol of urea were dissolved in deionized water to form a clear red solution. The red solution and the cleaned Ni foam were then transferred to a Teflon-lined stainless-steel autoclave and kept at 130 °C for 5 h. Then, to obtain the hierarchically-assembled 3D porous $ZnCo_2O_4/NiMoO_4$ heterostructures, precursors for $NiMoO_4$ were prepared. For this, 1.0 mmol of $Ni(NO_3)_2 \cdot 6H_2O$ and 1.0 mmol of Na_2MoO_4 were dissolved in a solution (deionized water and ethanol) to form a clear green solution. The green solution and the annealed Ni foam sample with a nanoporous $ZnCo_2O_4$ core were then transferred to the Teflon-lined stainless-steel autoclave and kept at 140 °C for 4 h.

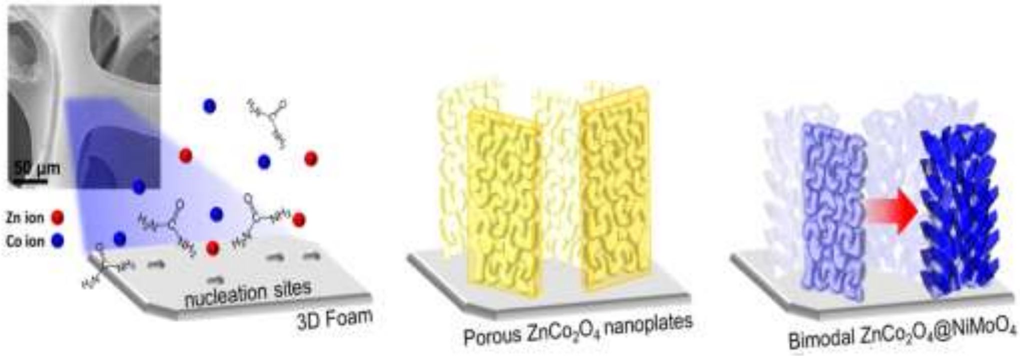

Figure 6.7: Illustrations of the hierarchically-assembled 3D porous $ZnCo_2O_4/NiMoO_4$ heterostructures and the corresponding fabrication steps.

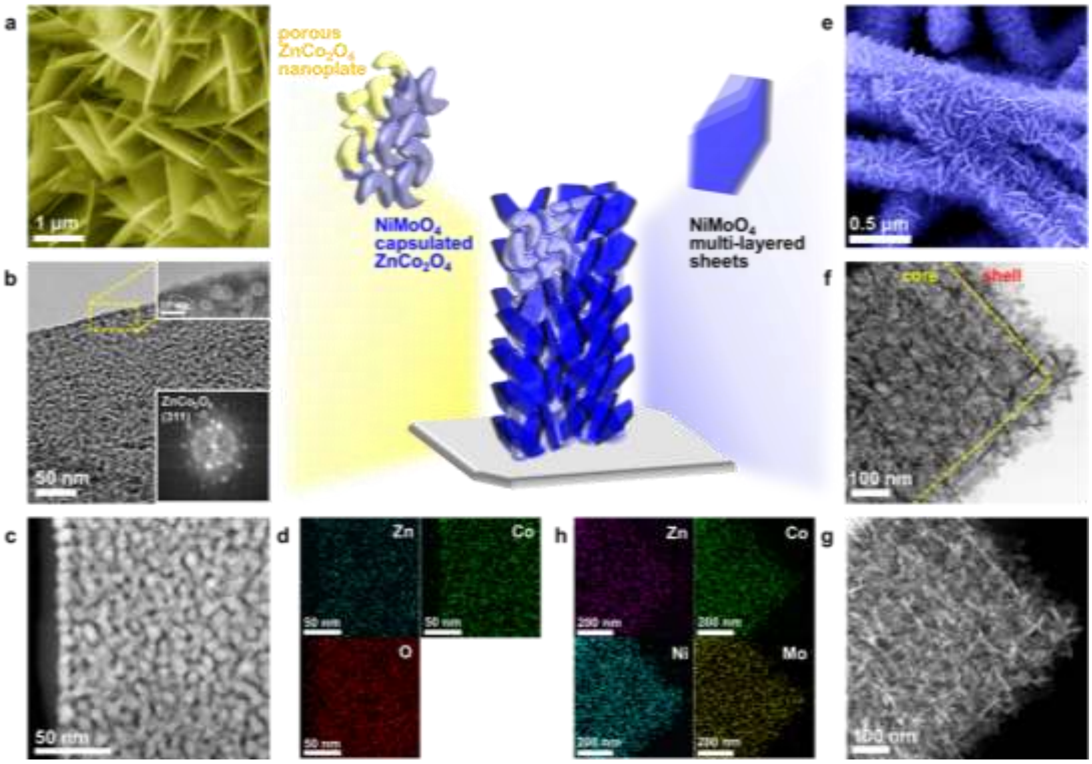

Figure 6.8: (a) SEM, (b) TEM, (c) HADDF-STEM, and (d) EDX mapping images of 3D nanoporous $ZnCo_2O_4$. (e) SEM, (f) STEM, (g) HADDF-STEM, and (h) EDX mapping images of hierarchically-assembled 3D porous $ZnCo_2O_4/NiMoO_4$ heterostructures. (TEM images were taken by Dr. Y.-W. Lee at UNIST).

The hierarchically-assembled 3D $ZnCo_2O_4$/$NiMoO_4$ heterostructures were assessed using scanning electron microscopy (SEM), transmission electron microscopy (TEM), and high-angle annular dark-field scanning TEM (HAADF-STEM) measurements (**Figure 6.8**). The thin nanostructured $ZnCo_2O_4$-only plates were synthesized (**Figure 6.8**a-d). TEM studies reveal that the plates are composed of rigidly interconnected nanoscale grains and pores with sizes in the range 10 – 20 nm. Moreover, the HAADF-STEM image of $ZnCo_2O_4$ demonstrates the existence of highly-entangled grains (white space) and pore channels (black space). The elemental distribution of the $ZnCo_2O_4$ plates is also clearly identified from an energy dispersive X-ray spectroscopy (EDX) mapping analysis. After the assembly of the 3D $ZnCo_2O_4$/$NiMoO_4$ heterostructures, there is an obvious change in the surface morphology of the electrodes with the addition of the secondary nanosheet arrays (**Figure 6.8**e-h). Notably, TEM and HAADF-STEM images show morphologically-distinct regions, including a primary plate region with an interconnected porous network and a secondary nanosheet region. Furthermore, the EDX mapping images show that all the elements (Zn, Co, Ni, and Mo) are uniformly distributed along the hierarchical nanostructures. Therefore, these results indicate the formation of $ZnCo_2O_4$/$NiMoO_4$ heterostructures with additional secondary nanostructures. In addition, the cross-sectional STEM images of the $ZnCo_2O_4$/$NiMoO_4$ heterostructure sample prepared using a focused ion beam also clearly verify the hierarchical formation of the secondary protruding layered nanosheets on the primary nanoporous plates (**Figure 6.9**).

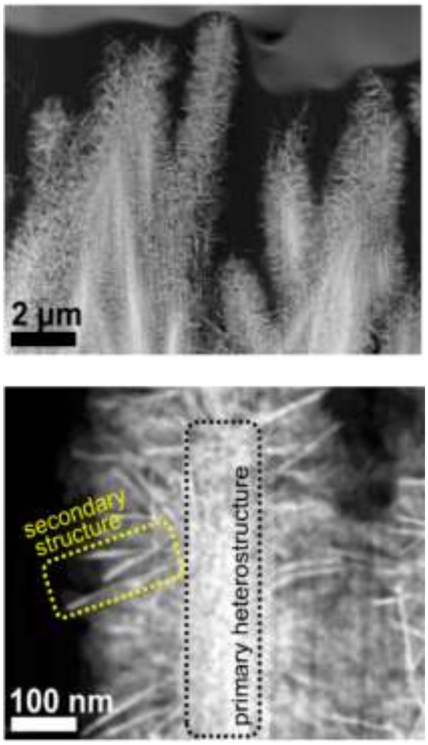

Figure 6.9: Low-resolution and high-resolution cross-sectional HAADF-STEM images of the $ZnCo_2O_4/NiMoO_4$ heterostructures (TEM images were taken by Dr. Y.-W. Lee at UNIST).

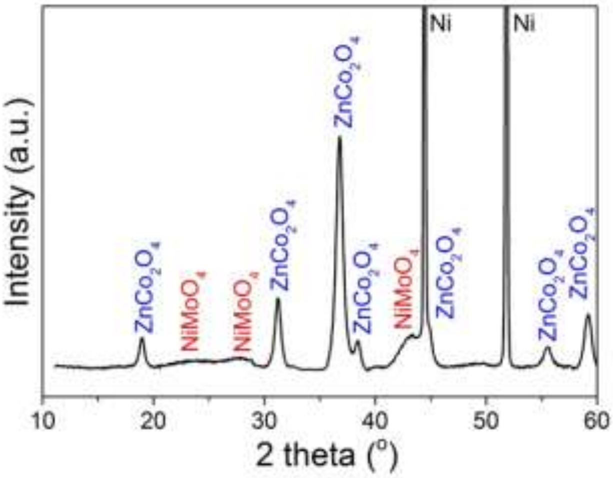

Figure 6.10: XRD pattern of the as-prepared $ZnCo_2O_4/NiMoO_4$ sample.

As shown in **Figure 6.10**, to evaluate the crystallographic phase of the $ZnCo_2O_4/NiMoO_4$ electrode samples, XRD spectra were analyzed. The locations of the diffraction peaks of the heterostructures can be indexed using the standard diffraction patterns of $ZnCo_2O_4$ (JCPDS 23-1390) and $NiMoO_4$ (JCPDS 86-0361).[18-19]

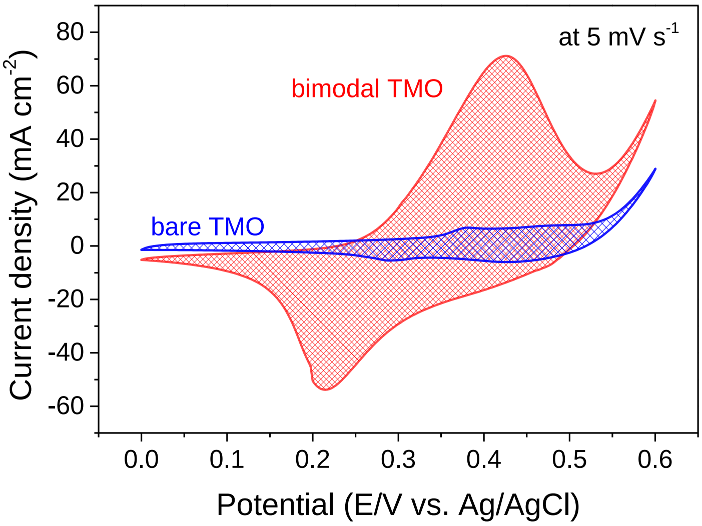

Figure 6.11: CV curves of the bimodal- and bare-BTMO at a scan rate of 5 mV s^{-1}.

The overall electrochemical performance of the bare $ZnCo_2O_4$ electrode without any additional $NiMoO_4$ layer (denoted as single-BTMO) and the $ZnCo_2O_4/NiMoO_4$ heterostructured electrode with hierarchically bimodal geometrical structures (denoted as bimodal-BTMO) was investigated. As shown in **Figure 6.11**, a cyclic voltammetry (CV) curve of the bimodal-BTMO exhibits a typical Faradaic redox behavior with a potential window ranging from 0.0 to 0.6 V at a scan rate of 5 mVs^{-1}. The integrated CV area for the bimodal-BTMO sample is found to be much larger than that of the single-BTMO. This indicates that the bimodal-BTMO possesses a superior electrochemical capacitance.

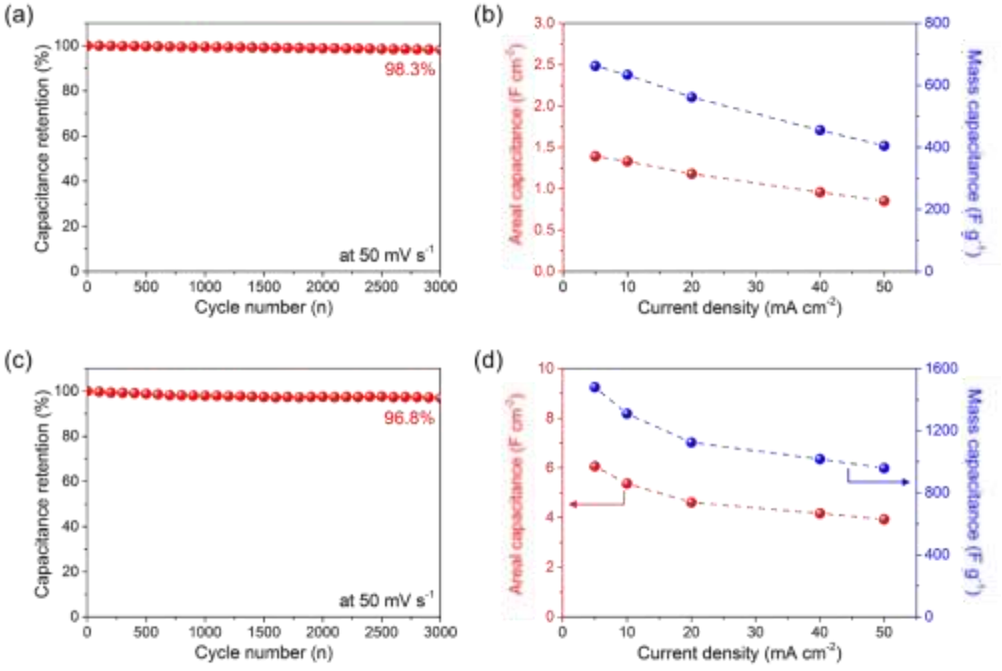

Figure 6.12: (a) Cycling stability and (b) areal and mass capacitance of the bare-BTMO electrodes. (c) Cycling stability and (d) areal and mass capacitance of the bimodal-BTMO electrodes.

As shown in **Figure 6.12**, the area and mass capacitance of the bare-BTMO is found to reach 1.39 F cm^{-2} and 661.90 F g^{-1}, respectively. The cycling capacitance of the bare-BTMO retains more than 98.3% of its initial capacitance after 3000 cycles at 50 mVs^{-1}. The high cyclability of the bare-BTMO electrode can be strongly attributed to morphological advantages such as a stable nanoporous structure and favorable spinel crystal properties of $ZnCo_2O_4$. The areal and mass capacitance of the bi-hierarchical-BTMO are significantly enhanced such that they reach values of 6.07 F cm^{-2} and 1480.48 F g^{-1}, respectively, at a current density of 2 mA cm^{-2}, which is a factor of four more than that of the specific capacitance of the bare-BTMO. Moreover, the electrode retains more than 96.8% of its initial capacitance after 3000 cycles at 50 mVs^{-1}.

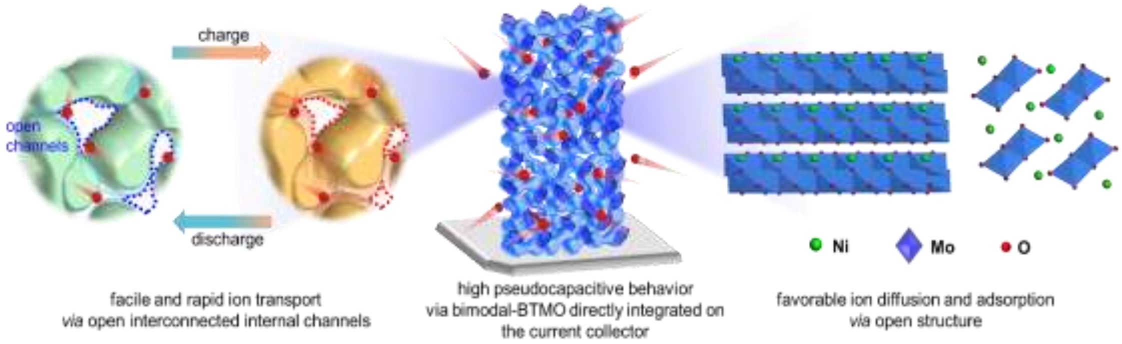

Figure 6.13: Illustration showing pseudo-capacitive behaviour in hierarchically-assembled 3D porous $ZnCo_2O_4/NiMoO_4$ heterostructures.

As illustrated in **Figure 6.13**, the hierarchically-assembled 3D heterostructures consist of open interconnected porous channels, providing an enhanced surface area and multi-access diffusion pathways for facile and rapid ion transport. The second advantage is the formation of the secondary protruding $NiMoO_4$ nanosheets on the surface of the primary nanoplates, which provide an additional contribution to the improvement of the specific capacitance and electrochemical kinetics because of the high pseudo-capacitive activity combined with the unique layered, open structure that facilitates favorable ion diffusion and adsorption. An additional advantage of this electrode design is the direct integration of the $ZnCo_2O_4$ backbone structure, which has high electric conductivity and good structural stability, onto the 3D microporous current collector framework and ensures fast electron transport and good structural integrity.

6.3 Direct Solution Growth Method for Nanostructured Electrode

Based on thermal synthesis, there are several issues that still need to be addressed, such as the long processing time (about 12-24 hr) and the need for additional post-heat-treatment (about 200-400 ºC) steps, which are severely limiting in terms of the production and scalability of the electrode fabrication. Instead of using solution thermal synthesis, an ultrafast synthesis (~10 min) strategy at room temperature for producing nanostructured transition metal sulphides is proposed.

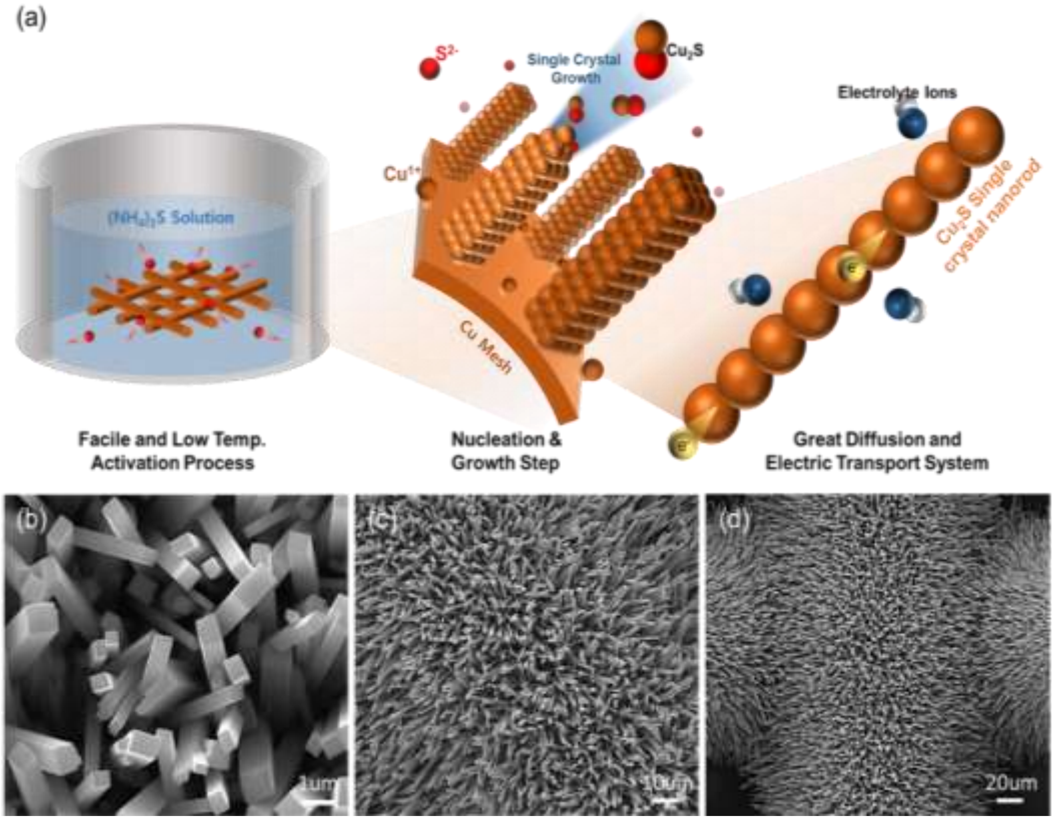

Figure 6.14: (a) Schematic illustration of direct solution growth of copper sulphide and (b-d) SEM images of the Cu_2S electrode for different magnifications.

As shown in **Figure 6.14**, a facile, one-step surface activation method was used to fabricate single crystalline Cu_2S nanorod (SC-Cu_2S NR) arrays via a solution-based process. A Cu mesh substrate was directly immersed into an aqueous ammonium sulphide solution ($(NH_4)_2S$ solution) in ambient conditions at room temperature. The ammonium sulphide solution then rapidly reacts with the Cu substrate, and the Cu ions emanating from the substrate are eluted quickly. After the rapid (10 to 15 min) nucleation and growth steps, the uniform-arrayed SC-Cu_2S NRs are then successfully fabricated on the substrate. Scanning electron microscopy (SEM) observations revealed that the as-prepared SC-Cu_2S NRs were uniformly dispersed across the entire Cu substrate. The morphology of the Cu_2S NRs shows a well-defined rectangular shape with dimensions of about 200–600 nm in width, and a few tens of micrometers in length. The cubic-shaped nanorods enclosed by well-faceted side planes indicate the formation of a single crystalline phase of Cu_2S.

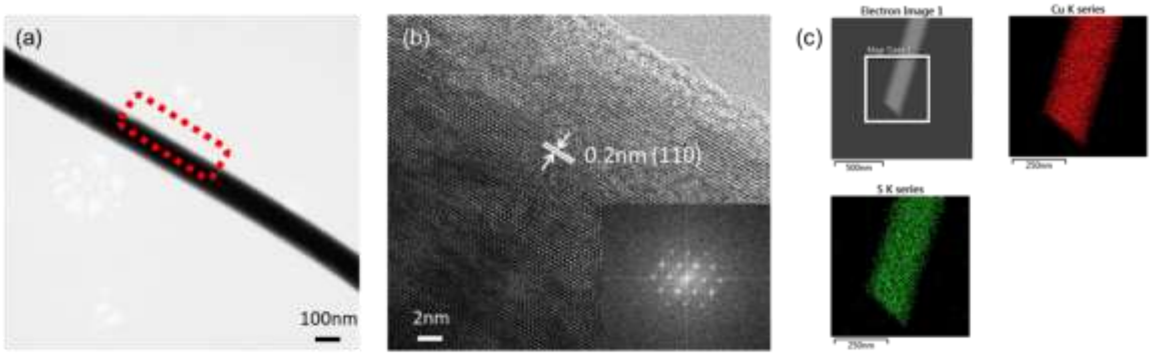

Figure 6.15: (a) Low-resolution, (b) high-resolution, and (c) EDX mapping images of the SC-Cu_2S electrodes. (TEM images were taken by Dr. Y.-W. Lee).

The SC-Cu_2S NRs were examined using transmission electron microscopy (TEM) and corresponding fast Fourier transform diffraction (FFT) pattern measurements (**Figure 6.15**). The TEM images reveal that the Cu_2S NRs form a single-crystalline phase. The interplanar d-spacing is about ~0.2 nm corresponding to the (110) plane in the cubic crystal structure of Cu_2S.[20] Moreover, the FFT image further confirms the formation of a single crystalline phase of Cu_2S. Finally, the elemental distribution of the SC-Cu_2S NRs is also clearly identified by energy dispersive X-ray spectroscopy (EDX) mapping analysis, confirming the existence of the Cu and S elements. To evaluate the crystallographic phase of the as-prepared SC-Cu_2S NR samples, we carried out X-ray diffraction (XRD) spectroscopy analysis on the samples (**Figure 6.16**). The diffraction patterns obtained from the SC-Cu_2S NR samples are indexed using the standard diffraction patterns of Cu_2S (JCPDS Card No. 26-1116) without any obvious differences in the peak values.[21]

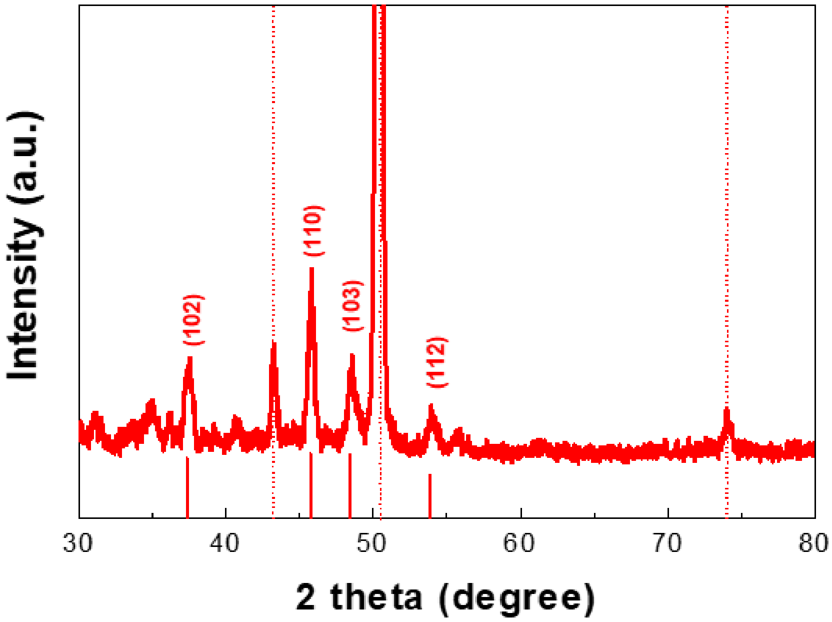

Figure 6.16: XRD of the SC-Cu_2S nanoarrays.

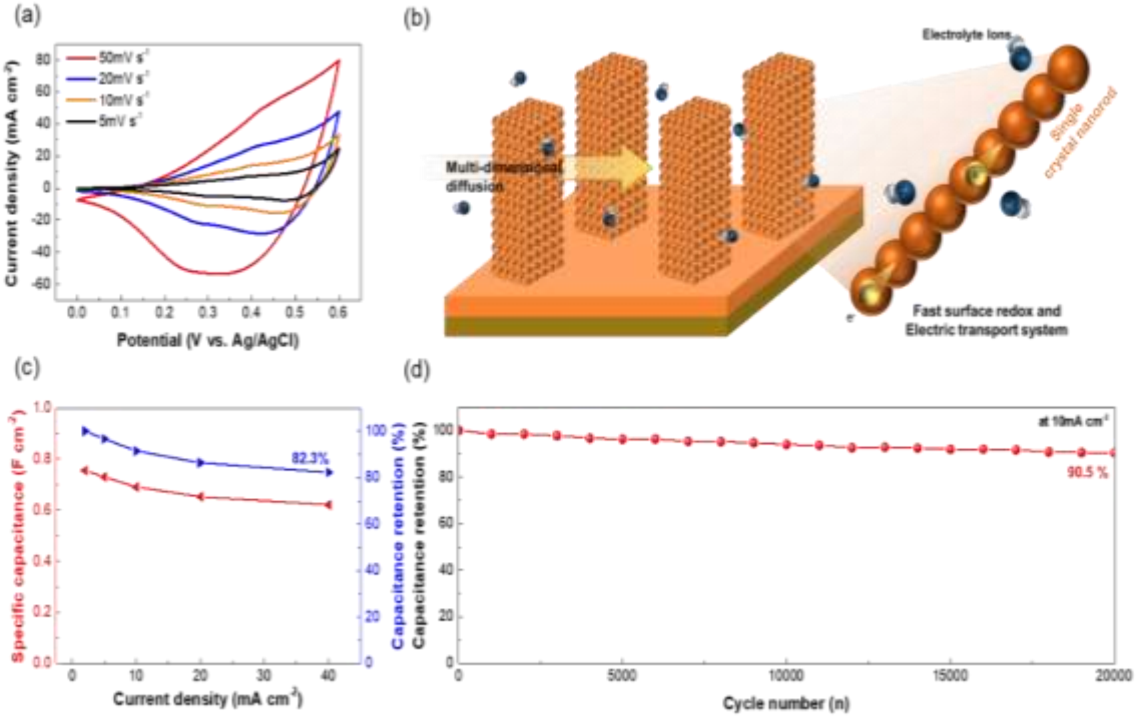

Figure 6.17: (a) CV curves of the SC-Cu_2S electrode. (b) Illustration of the SC-Cu_2S electrode. (c) Calculated specific capacitance of the SC-Cu_2S electrode (primary axis) and the capacitance retention (secondary axis). (d) Capacitance retention of the SC-Cu_2S electrode at a current density of 10 mA cm^{-2} when subjected to 20,000 charge/discharge cycles.

Figure 6.17a shows cyclic voltammetry (CV) curves of the SC-Cu_2S NR electrode in the presence of a potential in the range from 0.0 V to 0.6 V. All of the CV curves are of a similar shape within the different scan rates, indicating reversible Faradaic behaviour of the electrode. The areal capacitance of the SC-Cu_2S NR electrode reaches 0.75 F cm^{-2}. Furthermore, even at a high charge/discharge rate of 40 mA cm^{-2}, the SC-Cu_2S NR electrode exhibits a capacitive retention of 0.62 F cm^{-2}. About 82.3% of the capacitance is retained after the charging rate is increased from 2.0 to 40 mA cm^{-2}, demonstrating that the high conductivity and diffusion kinetics of the SC-Cu_2S NR electrode result in a high rate retention performance (**Figure 6.17**c). Moreover, the specific capacitance is maintained at 90.5% of the initial value even after 20,000 cycles, representing an excellent electrochemical stability of the device at a current density of 10 mA cm^{-2} (**Figure 6.17**d). The SC-Cu_2S NR electrode has a number of benefits that enable good electrochemical performance even though it has been fabricated using a facile and room-temperature process (**Figure 6.17**b). The unique 1-D nanostructures and single crystalline compositional features of the electrodes can provide multiple-access diffusion channels for the electrolyte ions, a fast surface redox reaction on the Cu_2S surface and good conductive electric transport behavior.

6.4 Concluding Remarks

Adjusting the solubility in a hydrothermal approach has been shown to be a promising technique for producing highly efficient pseudo-capacitive electrodes with 1-D nanostructures. Such electrodes can easily promote dynamic electrochemical kinetics, including high Faradaic capacitance, high retention and fast charge transfer rate for practical pseudocapacitor applications. Moreover, this chapter has demonstrated hierarchically-assembled 3D porous heterostructures consisting of two different binary metal oxides so as to emphasize the importance of designing nanoarchitectures that optimize the intrinsic electrochemical properties and that provide a morphology that exhibits a high structural integrity. In the last part of this chapter, a single crystalline Cu_2S nanorod electrode has been successfully prepared via an ultrafast and low-temperature solution-based direct synthesis process. The resulting Cu_2S NR electrodes can be predictively and precisely synthesized by applying an ammonium sulphide solution.

6.5 References

[1] J.-C. Chou, Y.-L. Chen, M.-H. Yang, Y.-Z. Chen, C.-C. Lai, H.-T. Chiu, C.-Y. Lee, Y.-L. Chueh, and J.-Y. Gan, "RuO_2/MnO_2 core–shell nanorods for supercapacitors," J. Mater. Chem. A, vol. 1, no. 31, p. 8753, 2013.

[2] A. Ponrouch, S. Garbarino, E. Bertin, and D. Guay, "Ultra high capacitance values of Pt@RuO_2 core–shell nanotubular electrodes for microsupercapacitor applications," J. Power Sources, vol. 221, no. 1 p. 228, 2013.

[3] C. Zhang, Q. Chen, and H. Zhan, "Supercapacitors based on reduced graphene oxide nanofibers supported $Ni(OH)_2$ nanoplates with enhanced electrochemical performance," ACS Appl. Mater. interfaces, vol. 8, no. 35, p. 22977, 2016.

[4] Y. Wang, T. Zhou, K. Jiang, P. Da, Z. Peng, J. Tang, B. Kong, W. Cai, Z. Yang, and G. Zheng, "Reduced mesoporous Co_3O_4 nanowires as efficient water oxidation electrocatalysts and supercapacitor electrodes," Adv. Energy Mater., vol. 4, no. 16, p. 1400696, 2014.

[5] P. Gao, P. Metz, T. Hey, Y. Gong, D. Liu, D. Edwards, J. Howe, R. Huang, and S. Misture, "The critical role of point defects in improving the specific capacitance of δ-MnO_2 nanosheets," Nat. Comm., vol. 8, no. 1, p. 14559, 2017.

[6] J. Yang, M. Ma, C. Sun, Y. Zhang, W. Huang, and X. Dong, "Hybrid $NiCo_2S_4$@MnO_2 heterostructures for high-performance supercapacitor electrodes," J. Mater. Chem. A, vol. 3, no. 3, p. 1258, 2014.

[7] G. Zhang and X. Lou, “Controlled growth of $NiCo_2O_4$ nanorods and ultrathin nanosheets on carbon nanofibers for high-performance supercapacitors,” Sci. Rep., vol. 3, no. 1, p. 1470, 2013.

[8] A. Pendashteh, M. Rahmanifar, R. Kaner, and M. Mousavi, “Facile synthesis of nanostructured $CuCo_2O_4$ as a novel electrode material for high-rate supercapacitors,” Chem. Commun., vol. 50, no. 16, p. 1972, 2013.

[9] Z. Gu, H. Nan, B. Geng, and X. Zhang, “Three-dimensional $NiCo_2O_4$@$NiMoO_4$ core/shell nanowires for electrochemical energy storage,” J. Mater. Chem. A, vol. 3, no. 22, p. 12069, 2015.

[10] W. Zhou, X. Cao, Z. Zeng, W. Shi, Y. Zhu, Q. Yan, H. Liu, J. Wang, and H. Zhang, “One-step synthesis of Ni_3S_2 nanorod@$Ni(OH)_2$ nanosheet core–shell nanostructures on a three-dimensional graphene network for high-performance supercapacitors,” Energy Environ. Sci., vol. 6, no. 7, p. 2216, 2013.

[11] Y.-W. Lee, B.-S. Kim, J. Hong, J. Lee, S. Pak, H.-S. Jang, D. Whang, S. Cha, J. Sohn, and J. Kim, “A pseudo-capacitive chalcogenide-based electrode with dense 1-dimensional nanoarrays for enhanced energy density in asymmetric supercapacitors,” J. Mater. Chem. A, vol. 4, no. 26, p. 10084, 2016.

[12] L. Shen, J. Wang, G. Xu, H. Li, H. Dou, and X. Zhang, “$NiCo_2S_4$ nanosheets grown on nitrogen-doped carbon foams as an advanced electrode for supercapacitors,” Adv. Energy Mater., vol. 5, no. 3, p. 1400977, 2015.

[13] C. Ji, F. Liu, L. Xu, and S. Yang, “Urchin-like $NiCo_2O_4$ hollow microspheres and $FeSe_2$ micro-snowflakes for flexible solid-state asymmetric supercapacitors,” J. Mater. Chem. A, vol. 5, no. 11, p. 5568, 2017.

[14] M. Liang, M. Zhao, H. Wang, J. Shen, and X. Song, "Enhanced cycling stability of hierarchical $NiCo_2S_4$@$Ni(OH)_2$@PPy core–shell nanotube arrays for aqueous asymmetric supercapacitors," J. Mater. Chem. A, vol. 6, no. 6, p. 2482, 2018.

[15] Z. Huang, Z. Zhang, X. Qi, X. Ren, G. Xu, P. Wan, X. Sun, and H. Zhang, "Wall-like hierarchical metal oxide nanosheet arrays grown on carbon cloth for excellent supercapacitor electrodes," Nanoscale, vol. 8, no. 27, p. 13273, 2016.

[16] B. Senthilkumar, K. Sankar, R. Selvan, M. Danielle, and M. Manickam, "Nano α-$NiMoO_4$ as a new electrode for electrochemical supercapacitors," RSC Adv., vol. 3, no. 2, p. 352, 2012.

[17] S. Liu, O. Hui, and K. N. Hui, "Flower-like copper cobaltite nanosheets on graphite paper as high-performance supercapacitor electrodes and enzymeless glucose sensors," ACS Appl. Mater. Interfaces, vol. 8, no. 5, p. 3258, 2016.

[18] G. Gao, H. Wu, B. Dong, S. Ding, and X. Lou, "Growth of ultrathin $ZnCo_2O_4$ nanosheets on reduced graphene oxide with enhanced lithium storage properties," Adv. Sci., vol. 2, no. 1, p. 1400014, 2015.

[19] L. Huang, W. Zhang, J. Xiang, H. Xu, G. Li, and Y. Huang, "Hierarchical core-shell $NiCo_2O_4$@$NiMoO_4$ nanowires grown on carbon cloth as integrated electrode for high-performance supercapacitors," Sci. Rep., vol. 6, no. 1, p. 31465, 2016.

[20] W.-Y. Wu, S. Chakrabortty, A. Guchhait, G. Wong, G. Dalapati, M. Lin, and Y. Chan, "Solution-processed 2D PbS nanoplates with residual Cu_2S exhibiting low resistivity and high infrared responsivity," Chem. Mater., vol. 28, no. 24, p. 9132, 2016.

[21] Y. Zhou, Y. Lei, D. Wang, C. Chen, Q. Peng, and Y. Li, “Ultra-thin Cu_2S nanosheets: effective cocatalysts for photocatalytic hydrogen production,” Chem. Comm., vol. 51, no. 68, p. 13305, 2015

Chapter 7. Conclusion

7.1 Summary

This study strongly focuses on nanostructure-based energy storage and generation system (solar cells and supercapacitor). The physical and chemical properties that govern the operation of these energy generation and storage devices were systematically investigated. Moreover, this study showed the complexity of harnessing the potential advantages of nanostructured materials in energy generation and storage systems. Via novel approaches in the synthesis, fabrication and functionalization, this collective work has revealed new methods, and exploited novel physical and chemical properties to understand the underlying energy mechanism so as to significantly enhance the performance of those devices.

To begin with, PbS CQDs with a range of band gaps have been synthesized and characterized for energy generation applications. For the first time, large band gap PbS CQDs have been synthesized using a liquid and solid non-hot-injection method, which controls the precursor reactivity. Moreover. special consideration was given to the role of the organic capping layer that covers the 0-dimensional CQDs. It was found that by means of ligand exchange methods (either changing the degree level of halide ions on the CQDs or attaching the additional pyridine ligands on the CQDs) it is possible to tailor the electro-optical properties of the resulting films, leading to high-performance energy generation devices. This work also presents a controlled device structure with dual plasmonic layers. Applying two different plasmonic nanoparticles (Au and Ag) at the interface of the electrodes can effectively increase the overall photon absorption efficiency of the CQD film, leading to an improvement in the device performance.

Following the developments made in energy conversion this thesis then considers energy storage mechanisms. In this work, we consider pseudo and super-capacitors and show that various nanostructures can be made from metal oxides and sulphides using a simple solution synthesis method. Controlling the aspect ratio of the 1-D nanostructure is shown to be important for supercapacitor devices that can deliver more electricity. In addition, unique nanoporous core-shell nanostructures are shown to synergistically exhibit superior stability and excellent specific capacitance for supercapacitor. Finally, a simple dipping method for single crystalline sulphides with 1-D nanostructures can be predictively and precisely synthesized by applying an ammonium sulphide solution, and also can be further used in practical applications such as roll-to-roll processes.

7.2 Future Work

Recent research demonstrates that ink-type QD solutions with proper synthetic methods and liquid-state surface functionalization can exhibit a large PCE improvement. By optimizing the methods demonstrated in this thesis, we can produce ink-type QDs with hybrid ligand materials (such as halides and pyridine) to provide better surface passivation of CQDs. Moreover, to advance towards genuinely practical methods for commercialization, electrode materials need to be rapidly fabricated at low temperature without any additional heat treatment processes, supporting the scalable, mass-efficient, and cost-effective production of pseudocapacitive electrodes. The sulphide solution method presented herein is compatible with a general roll-to-roll fabrication process, guaranteeing both mass and large area production of the electrodes. We are planning to test electrochemical performance of nanostructured sulphide electrodes following the roll-to-roll process.

List of Publications

[First author papers]

(01) Lee, Y.-W.* **Hong, J.*** An, G.-H. Pak, S. Lee, J. Cho, Y. Lee, S. Cha, S. Sohn, J. Kim, J. “Synergistic Effects of Engineered Spinel Hetero-Metallic Cobaltites on Electrochemical Pseudo-Capacitive Behaviors.” **J. Mater. Chem. A** (2018) DOI: 10.1039/c8ta04616f.

(02) **Hong, J.*** Lee, Y.-W.* Ahn, D. Pak, S. Lee, J. Jang, A.-R. Lee, S. Hou, B. Cho, Y. Morris, S. Shin, H. Cha, S. Sohn, J. Kim, J. “Highly Stable 3D Porous Heterostructures with Hierarchically-Coordinated Octahedral Transition Metals for Enhanced Performance Supercapacitors.” **Nano Energy** 39, 337 (2017).

(03) **Hong, J.** Lee, Y.-W. Hou, B. Ko, W. Lee, J. Pak, S. Hong, J.-P. Morris, S. Cha, S. Sohn, J. Kim, J. “Solubility-Dependent $NiMoO_4$ Nanoarchitectures: Direct Correlation between Rationally Designed Structure and Electrochemical Pseudo-Kinetics.” **ACS. Appl. Mater. Interfaces** 8, 35227 (2016).

(04) **Hong, J.*** Hou, B.* Lim, J. Pak, S. Kim, B.-S. Cho, Y. Lee, J. Lee, Y.-W. Giraud, P. Lee, S. Park J. Morris, S. Snaith, H. Sohn, J. Cha, S. Kim, J. “Enhanced Charge Carrier Transport Properties in Colloidal Quantum Dot Solar Cells via Organic and Inorganic Hybrid Surface Passivation.” **J. Mater. Chem. A** 4, 18769 (2016).

(05) Kim, B.-S.* **Hong, J.*** Hou, B. Cho, Y. Sohn, J. Cha, S. Kim, J. “Inorganic-Ligand Exchanging Time Effect in PbS Quantum Dot Solar Cell.” **Appl. Phys. Lett.** 109, 063901 (2016).

[Submission & Preparation First Author Papers]

(01) **Hong, J.** et.al. “Strategic Chalcogenide Solution-Mediated Activation Protocol for Scalable, Room-Temperature, and Ultrafast Synthesis of Single-Crystalline 1-D Copper Sulfide.” **Adv. Sci.** (2018) [submitted].

(02) Lee, Y.-W.* **Hong, J.*** Lee, J.* et.al. “Multiple Faradaic Charge Storing Reactions Enabled by an Ni-S-O Compound System with Active Binary Anions.” **Nano Energy** (2018) [submitted].

(03) **Hong, J.** et. al. “Harnessing Dual-Plasmonic Effects for High-Performance Quantum Dot Solar Cells.” **ACS. Appl. Mater. Interfaces** (2018) [submitted].

(04) **Hong, J.*** et. al. “Scalable fabrication of h-BN as lithium dendrite preventing separator with outstanding thermal stability.” [under preparation]

(05) **Hong, J.*** et. al. “Strategic synthesis process of metallic two-dimensional copper sulfide film for transparent and conductive film.” [under preparation]

[Co-author papers]

(01) Cho, Y.* Lee, S.* **Hong, J.** Pak, S. Hou, B. Lee, Y.-W. Jang, J. Im, H. Sohn, J. Cha, S. Kim, J. "Sustainable Hybrid Harvester Based on Air Stable Quantum Dot Solar Cells and Triboelectric Nanogenerator." **J. Mater. Chem. A,** advanced article (2018).

(02) Cho, Y.* Hou, B.* Lim, J. Lee, S. Pak, S. **Hong, J.** Giraud, P. Jang, A.-R. Lee, Y.-W. Lee, J. Jang, J. Snaith, H. Morris, S. Sohn, J. Cha, S. Kim, J. "Balancing Charge Carrier Transport in a Quantum Dot P–N Junction toward Hysteresis-Free High-Performance Solar Cells." **ACS Energy Lett.** 3, 1036 (2018).

(03) Jang, A.-R.* Lee, Y.-W.* Lee, S.-S. **Hong, J.** Baek, S.-H. Pak, S. Lee, J. Shin, H. Ahn, D. Hong, W.-K. Cha, S. Sohn, J. Park, I.-K. "Electrochemical and electrocatalytic reaction characteristics of boron-incorporated graphene via a simple spin-on dopant process." **J. Mater. Chem. A**, advanced article (2018).

(04) Cho, Y. Giraud, P. Hou, B. Lee, Y. **Hong, J.** Lee, S. Pak, S. Lee, J. Jang, J. Morris, S. Sohn, J. Cha, S. Kim, J. "Charge Transport Modulation of a Flexible Quantum Dot Solar Cell Using a Piezoelectric Effect." **Adv. Energy Mater.** 8, 1700809 (2018).

(05) J, Lee. Pak, S. Giraud, P. Lee, Y.-W. Cho, Y. **Hong, J.** Jang, A.-R. Chung, H.-S. Hong, W.-K. Jeong, H.Y. Shin, H.S. Occhipinti, L. Morris, S. Cha, S. Sohn, J. Kim, J. "Thermodynamically Stable Synthesis of Large-Scale and Highly Crystalline Transition

Metal Dichalcogenide Monolayers and their Unipolar n-n Heterojunction Devices.” **Adv. Mater.** 29, 1702206 (2017).

(06) Pak, S. Lee, J. Lee, Y.-W. Jang, A.-R. Ahn, S. Ma, K.Y. Cho, Y. **Hong, J.** Lee, S. Jeong, H.Y. Im, H. Shin, H.S. Morris, S. Cha, S. Sohn, J. Kim, J. “Strain-Mediated Interlayer Coupling Effects on the Excitonic Behaviors in an Epitaxially Grown MoS_2/WS_2 van der Waals Heterobilayer.” **Nano Lett.** 17, 5634 (2017).

(07) Lee, Y.-W.* Kim, B.-S.* **Hong, J.** Choi, H. Jang, H.-S. Hou, B. Pak, S. Lee, J. Lee, S.-H. Morris, S. Whang, D. Hong, J.-P. Shin, H. Cha, S. Sohn, J. Kim, J. “Hierarchically Assembled Tubular Shell-Core-Shell Heterostructure of Hybrid Transition Metal Chalcogenides for High-Performance Supercapacitors with Ultrahigh Cyclability.” **Nano Energy** 37, 15 (2017).

(08) Lee, J. Pak, S. Lee, Y.-W. Cho, Y. **Hong, J.** Giraud, P. Shin, H. Morris, S. Sohn, J. Cha, S. Kim, J. “Monolayer Optical Memory Cells Based on Artificial Trap-Mediated Charge Storage and Release.” **Nat. Commun.** 8, 14734 (2017).

(09) Hou, B. Cho, Y. Kim, B.-S. Ahn, D. Lee, S. Park, J. Lee, Y.-W. **Hong, J.** Im, H. Morris, S. Sohn, J. Cha, S. Kim, J. “Red Green Blue Emissive Lead Sulfide Quantum Dots: Heterogeneous Synthesis and Applications.” **J. Mater. Chem. C** 5, 3692 (2017).

(10) Cho, Y. Ahn, D. Park, J. Pak, S. Lee, S. Jun, B. **Hong, J.** Lee, S. Jang, J. Hong, J.-P. Morris, S. Sohn, J. Cha, S. and Kim, J. "Ferroelectrics: Enhanced Ferroelectric Property of P(VDF-TrFE-CTFE) Film Using Room-Temperature Crystallization for High-Performance Ferroelectric Device Applications." **Adv. Electron. Mater.** 10, 1600225 (2016).

(11) Hou, B. Cho, Y. Kim, B. **Hong, J.** Park, J. Ahn, S. Sohn, J. Cha, S. Kim, J. "Highly Monodispersed PbS Quantum Dots for Outstanding Cascaded-Junction Solar Cells." **ACS Energy Lett.** 1, 834 (2016).

(12) Lee, Y.-W.* An, G.-H.* Kim, B.-S. **Hong, J.** Pak, S. Lee, E.-H. Cho, Y. Lee, J. Giraud, P. Cha, S. Ahn, H.-J. Sohn, J. Kim, J. "Synergistic Effects of a Multifunctional Graphene Based Interlayer on Electrochemical Behavior and Structural Stability." **ACS Appl. Mater. Interfaces** 8, 17651 (2016).

(13) Kim, B.-S. Neo, D. Hou, B. Park, J. Cho, Y. Zhang, N. **Hong, J.** Pak, S. Lee, S. Sohn, J. Assender, H. Watt, Andrew. Cha, S. Kim, J. "High Performance PbS Quantum Dot/Graphene Hybrid Solar Cell with Efficient Charge Extraction." **ACS Appl. Mater. Interfaces** 8, 13902 (2016).

(14) Lee, Y.-W. An, G.-H. Lee, S. **Hong, J.** Kim, B.-S. Lee, J. Kwak, D.-H. Ahn, H.-J. Huh, W. Cha, S. Park, K.-W. Sohn, J. Kim, J. "Synergistic Incorporation of Hybrid

Heterobimetal–nitrogen Atoms into Carbon Structures for Superior Oxygen Electroreduction Performance.” **Catal. Sci. Technology** 6, 2085 (2016).

(15) Lee, Y.-W.* Kim, B.-S.* **Hong, J.** Lee, J. Pak, S. Jang, H.-S. Whang, D. Cha, S. Sohn, J. Kim, J. “A Pseudo-Capacitive Chalcogenide-Based Electrode with Dense 1-Dimensional Nanoarrays for Enhanced Energy Density in Asymmetric Supercapacitors.” **J. Mater. Chem. A** 4, 10084 (2016).